Methodical
and Applied Research

PROTON RADIOSURGERY AT THE PNPI SYNCHROCYCLOTRON

PNPI participants: Yu.A. Gavrikov, E.M. Ivanov, V.I. Lazarev, V.V. Lysenko, Yu.A. Malov, G.A. Ryabov, D.M. Seliverstov

RSCRST participants: D.L. Karlin, T.V. Pushkareva, R.A. Shalek, A.A. Shtyrkova, N.A. Skugareva, V.M. Vinogradov, M.V. Zhydkov, O.M. Zhydkova

1. Introduction

Radiosurgery is a one-time exposure of small pathological formations to high doses of radiation. Since April 1975, it has been systematically carried out at the PNPI synchrocyclotron medical proton complex SC-1000. The exposure technique is described in detail in Refs. [1, 2]. In total, 1386 patients have received a stereotactic radiosurgery by January 1, 2013.

Several upgrades of the installation, as well as of its system to control the exposure parameters, have been performed during 40 years of operation of the Pilot Medical Proton Complex (PMPC). In 1990, a lock-head device of the third generation was built, and the process to control the exposure parameters was computerised. In 2002–2004, with the support of the Government of Leningrad region, the PMPC was upgraded. In particular, new systems for monitoring the supplied doses and scanning, as well as for controlling the proton beam parameters, were built, some worn-out elements were replaced, and the automation of the beam output was performed.

2. Modernisation of the medical proton complex

In the period after 2005, the worn-out measuring systems were replaced, the software was changed, and some work to ensure the reliability of the system operations was carried out. In particular, to ensure the stability against noise, a photocoupler isolation of the local manual control of the installation for the exposure of patients was added.

A new temperature control unit was fabricated in the installation for the thermoluminescence dosimetry, which also increased the reliability of its operation.

The performance of the TLD-100 detectors of the "Harshaw" company was studied with respect to the parameters presented below, with the aim to use these detectors in clinical dosimetry instead of LiF detectors.

2.1. Dependence of the light yield on the radiation dose

One can see in Fig. 1 that the obtained data are in good agreement with those in the literature.
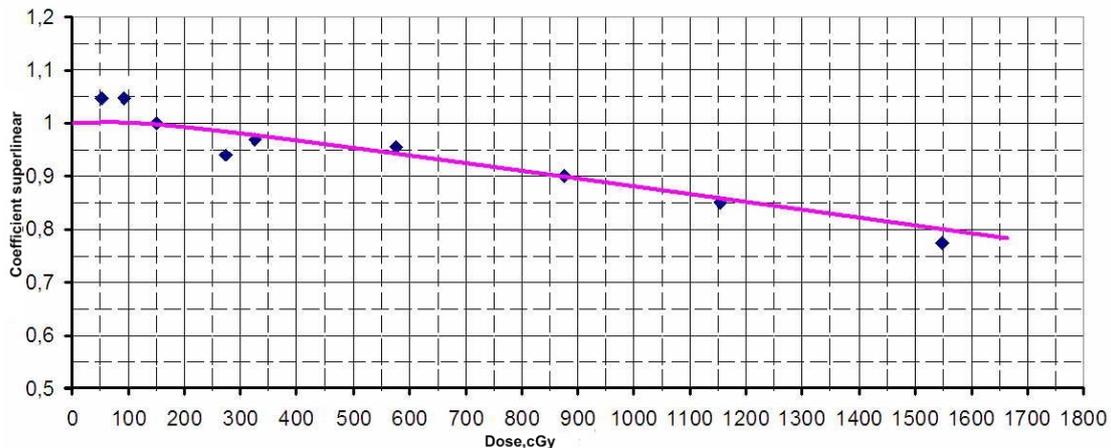

Fig. 1. Superlinearity curve for the TLD-100 detectors

2.2. Spontaneous loss of the information on the accumulated dose over time

Such a characteristic as the loss of the detector information (fading) is very important. While fading occurs even in normal conditions, its influence can be reduced by using special modes of the TLD preparation to reading, *e.g.*, by their pre-exposure to certain temperatures for a certain time. Providing that the reading regimes are standard and preparing them to be read, one can apply the corrections for fading, which is a function of the time passed after the previous reading or the moment of exposure. The results of the fading effect are given in Fig. 2.
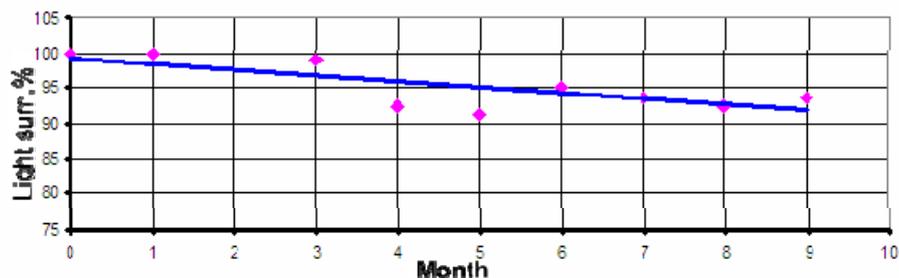

Fig. 2. Information loss of the irradiated TLD-100 versus the storage time

For the TLD-100, the fading for the first three months (the typical control period) was about 3 %. After the period of four months, the fading did not exceed more than 7.5 %. The obtained results are in good agreement with the published data on the dependence on the storage time of the information loss of the irradiated TLD.

2.3. Reproducibility of dosimeter readings

In clinical dosimetry, including the construction of dose distributions and fields, the reproducibility of the detectors – the ability of the dosimeters to show the same value of a dose in the same experimental conditions – is very important. For clinical dosimetry, the detectors are considered to be acceptable when the difference in readings of two measurements does not exceed 5 % (2 divisions on the device frame). The number of suitable TLD-100 detectors with the difference in readings between the first and the second measurement equal to 0, 1, 2 divisions was 155, or 78.7 % of the total number (197) of the detectors (Table 1).

Table 1

Reproducibility of dosimeter indications

Difference in the dosimeter readings between the 1-st and 2-nd measurements	Number of TLD	% of the total number
0	41	20.8
1	61	31
2	53	26.9
3	23	11.7
4	12	6.1
5	3	1.5
6	1	0.5
7	2	1
9	1	0.5
0–2	**155**	**78.7**

2.4. Dose measurements and construction of the dose fields and distributions

Two cassettes *XY* and *ZY* with the thermoluminescence detectors (by the "Harshaw" company) were prepared to measure the doses and to construct the dose fields. The measurements were performed using a homogeneous phantom of the human head made from plexiglass in the shape of a sphere of 160 mm in diameter. Before the irradiation, the phantom was centred on the rotation pole. During the period of the irradiation, the loch-device made 14 passes over ± 36º, the treatment table – 14 passes in one direction, the radiation dose being 6.56 Gy.

The calculations were made using Microsoft Office Excel, and the dose distributions and the dose fields were built in the PUSK application hosted inside MATLAB 5.5.0. The flowchart of the application used to build the dose distributions and fields is given in Fig. 3.
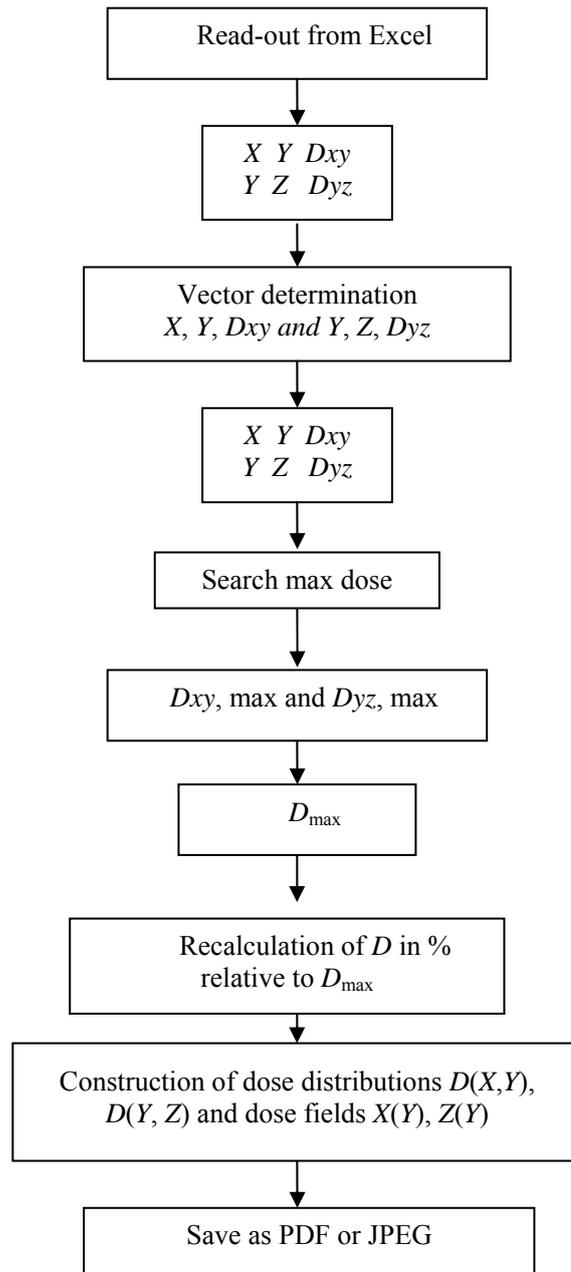

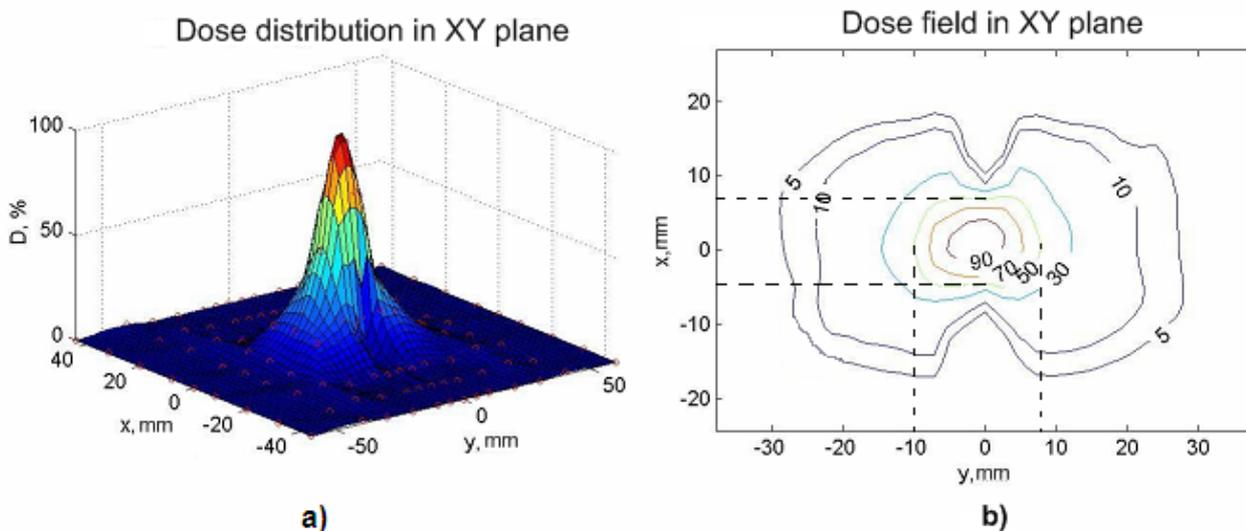**Fig. 3.** The flowchart of the used application

Fig. 4. Result of the PUSK application. a – the dose distribution and b – the field in the *XY* plane with mobile proton beam irradiation. The beam dimensions are $\Delta x = 12$ mm and $\Delta y = 18$ mm

The result of the PUSK application is presented in Fig. 4a, b, which shows the result of the connection to 50%-isodoses of two fields with the dimensions $\Delta x = 6$ mm, $\Delta y = 8$ mm, $\Delta z = 6$ mm. The docking of the fields is necessary for the irradiation of complex configuration targets, *e.g.*, cerebral ArterioVenous Malformation (AVM). The distance between the centres of the fields is selected according to the form and the size of the irradiation field, which was measured in a tissue-equivalent on the phantom and obtained at mobile proton beam irradiation with the dimensions $\Delta x = 12$ mm and $\Delta y = 18$ mm (50 % isodose). Note that the rotation pole and the phantom centre coincide. The measurements were performed with the thermoluminescent dosimeters that were 3 mm in diameter and 1 mm thick. Such a representation of the depth dose field clearly shows a high degree of localization of the absorbed energy in the centre of rotation.

3. Proton radiosurgery

The experience of proton radiosurgery performed at the SC-1000 is summarized in Table 2.

Table 2

Proton radiosurgery of FSBI RSCRST at the PNPI synchrocyclotron from 2007 to 2012

Irradiation of pituitary – hypophysectomy	50
Pituitary adenomas	12
Mammary cancer	18
Prostate cancer	20
Irradiation of brain	10
Arteriovenous malformation	10
Total	60
Of these repeated	2

In detail, in the cases of prolactin-secreting adenoma, clinical remission was observed in 80 % of the patients and stabilization – in 15 % of the cases. 21 female patients could become pregnant and gave birth to healthy children (4 patients – twice). The complete clinical remission was observed in 92 % of the Icenko – Cushing's disease cases and, in the long-term period, this figure was equal to 96 %. This was manifested in

disappearance of the diabetes, normalization of the blood pressure and regression of the pathological obesity. In the long-term period, the sustained recovery and full normalization of the growth hormone was observed in 86 % of the patients with acromegaly. In this case, the overwhelming majority of the patients were not marked by development of the secondary hormone deficiency. The clinical cure with hormonally inactive adenomas was 95 %. The treatment with the proton irradiation did not cause any serious threatening complications.

Figure 5 shows photographs of a patient before and after the irradiation. The patient had the Icenko – Cushing's disease causing obesity, diabetes, high blood pressure, calcium loss from bones, fractures, and impotence. The results of the proton therapy speak for themselves: 2 years after the therapy – the blood pressure became normal, there was no diabetes, the patient had daily 2 km runs; 3 years after the therapy – the patient got married; 4 years later – he became father.

Fig. 5. Patient before (left) and after (right) the irradiation

Figure 6a shows the arteriovenous malformation of patient L., who previously had a stroke, before the Proton Therapy (PT) and 3 years after the PT. Figure 6b shows patient L. after the PT.

A year after the proton therapy, L. had a child and moved to a village to work as a postman. She drives a car and gives an interview to a TV reporter.

Our work is still in progess…

Fig. 6. a – the AVM of patient L. before the PT (left) and the AVM of this patient 3 years after the PT (right); b – patient L. several years after the proton therapy

References

1. N.K. Abrossimov *et al.*, Abstracts of XI Meeting on Applied Accelerators (ICAA 05), SPb. (2005).
2. N.K. Abrossimov *et al.*, Synchrocyclotron Journal of Physics: Conference Series **1**, 424 (2006).

DESIGN FEATURES OF THE 80 MeV H⁻ ISOCHRONOUS CYCLOTRON IN GATCHINA

PNPI participants: S.A. Artamonov, E.M. Ivanov, G.F. Mikheev, Yu.T. Mironov, G.A. Riabov.
D.V. Efremov NIIEFA participant: V.G. Mudrolubov

1. Introduction

The synchrocyclotron for acceleration of proton beams up to the energy of 1000 MeV is in operation in Gatchina since 1970. During this time, several reconstruction projects were proposed, but none of them was financially supported. As a result, it was decided to concentrate on a cheaper project and to construct an isochronous cyclotron for acceleration of protons up to 80 MeV. The cyclotron complex is designed for fundamental and applied researches – production of medical isotopes, beam therapy of eye melanoma and surface types of cancer.

To minimize the expenditures while designing the cyclotron, an attempt was made to use at most the existing synchrocyclotron infrastructure, *i.e.* the building, the bridge crane for 30 ton, the electric power system, the water cooling system, the ventilation system, *etc*. The iron yoke of the magnet model of the existing synchrocyclotron was taken for the cyclotron magnet system.

Acceleration of H⁻ ions has obvious advantages: a possibility for 100 % extraction of the beam with high intensity and variable energy. On the other hand, it requires a special source of H⁻ ions, high vacuum, and what is most important, the magnetic field strength in the magnet sector should not exceed in our case 17 kGs to prevent H⁻ electromagnetic dissociation.

The designing and construction of the H⁻ isochronous cyclotron were in progress several years, and the drawings for the main accelerator subsystems were completed in 2010 [1–3]. The cyclotron magnet was designed, produced, commissioned and put into operation, and full scale magnetic measurements were started. The main problem by that time became a purchase of industrially and commercially produced equipment that was realized in the frame of the nuclear medicine program of the National Research Centre "Kurchatov Institute". Starting from September 2010, the cyclotron and the beam transport line equipment have been mounted in the experimental hall.

2. General description

Main parameters of the cyclotron are presented in Table 1.

Table 1

Main parameters of the cyclotron

MAGNET	
Pole diameter	2.05 m
Valley gap	386 mm
Hill gap (min)	164 mm
Number of sectors	4
Spiral angle (max)	65 degrees
Field in the centre	1.352 T
Flutter (max)	0.025
Ampere-turns	3.4×10^5
Power	120 kW
Weight	250 t
HF SYSTEM	
Frequency	41.2 MHz
Potential	60 kV
Harmonics	2
HF power	2×40 kW

VACUUM	
Pressure	10^{-7} Torr
2 cryogenic pumps	2×3500 l/s
1 turbo-molecular	(H_2)
H⁻ source	
Multipole	1.5 mA
Injection energy	26 keV
AXIAL INJECTION	
Transport system: solenoid lens, solenoid, inflector	
EXTRACTION SYSTEM	
Stripping method	
Energy range	40–80 MeV

3. Features of the magnetic system

The magnet and the magnetic system are the most important and expensive parts of the cyclotron, and a considerable attention was paid to their design. The cyclotron magnetic field should meet several requirements. The magnetic field rigidity at the final orbit must reach $Br = 13.2$ kGs · m, which corresponds to 80 MeV energy of the proton beam. For insuring the isochronism, the magnetic field averaged over the azimuth when going from the centre of the magnet to the final orbit should increase by 8.5 %. The azimuthal variation of the magnetic field should provide the vertical and horizontal transversal focusing. Some room should be left for a high frequency system: the gap between the shims should be wider than 140–150 mm. In distinction from a standard cyclotron, there is an additional and essential requirement for an H⁻ machine – to keep H⁻ losses due to dissociation less than 5 %. There are two main problems related to the design of the magnetic field of an isochronous cyclotron. The first one is a selection of the magnetic field structure that would provide both the highest possible energy of the accelerated H⁻ ions for the given magnet and the beam losses below 5 %. The second problem is the determination of the pole tips geometry that would provide the desired field structure.

3.1. H⁻ losses and the magnetic structure

Two alternative versions of the magnetic structure have been examined. The first one has the flutter (the mean square relative variation of the magnetic field along the path of the particle under acceleration) $F = 0.04$, the spiral angle (the angle between the radius vector at the radius r and the tangent to the median line of a sector at the same radius) $\gamma = 55°$, the harmonic amplitude $A_4 = 4.15$ kGs, and the second one has $F = 0.025$, $\gamma = 65°$, and $A_4 = 3.28$ kGs at the final radius. Both versions provide about the same net axial focusing and differ by the field in the hill regions. Figure 1 presents the beam losses due to electromagnetic dissociation for these two versions of the magnetic structure. The second version, with a low flutter and a high spiral angle, was selected for the Gatchina cyclotron since it provides beam losses less than 5 %.
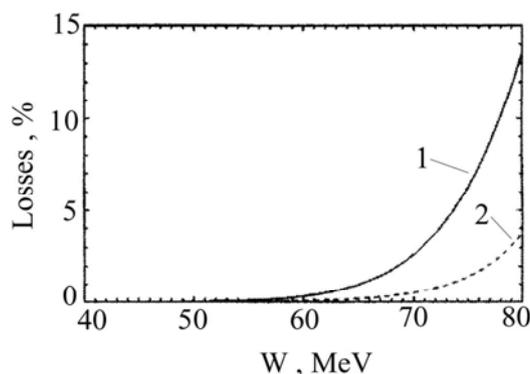

Fig. 1. H⁻ losses due to electromagnetic dissociation for two versions of the magnetic structure

3.2. The magnetic structure with a high spiral angle

Figure 2 presents a top view of the pole tips of the magnetic system. With the use of the Novosibirsk MERMAID code, which accounts for the iron saturation and permits to use up to 20×10^6 nodes, the profile of the iron shims was determined. More detailed information on the formation of the magnetic field is in a special report in this book. The distribution of the magnetic field in the full scale magnet was measured using a measuring system based on twenty NMR calibrated Hall probes and an automated coordinate system, which could position probes in the cylindrical coordinate system with an accuracy of 0.1 mm along the radius and azimuth at the radius of 100 cm. The achieved precision was equal to 2×10^{-2} % with the total time of measurements of 6–8 hours. Disagreement between the measurements and calculations did not exceed 20 Gs. The final distribution of the magnetic field was measured with 2–5 Gs precision.
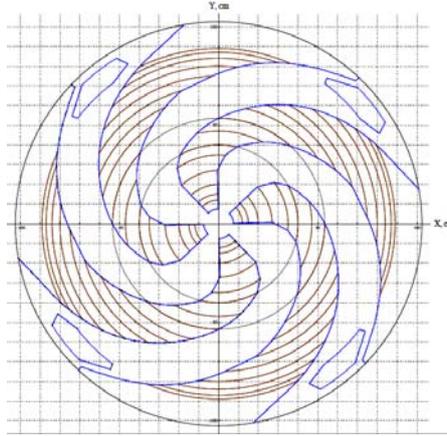
Fig. 2. Top view of the pole tip

3.3. The flutter versus the radius for straight sectors

The needed sizes of the valley and hill gaps were estimated by calculations of the flutter in a straight sector structure. An estimation of the flutter value, which defines the azimuthal variation of the magnetic field at different radii, requires three dimensional calculations even for straight sectors. Such calculations presented a real problem quite recently. For this reason, approximate methods were developed to analyze the problem. Approximate calculations cannot give quantitative results, but allow us to analyze qualitatively the relations between different parameters of the magnetic structure. In [4], under an assumption of a uniform magnetization of the magnet sectors, the value of the main harmonics of the magnetic field variation in an isochronous cyclotron is determined as:

$$B_N = 8\,M \sin(2\pi a / d) \exp(-2\pi g_h / d),$$

where $2a$ is the sector width along the azimuth for a given radius, $2g_h$ is the hill gap, d is the structure period equal to the sum of widths of the valley and the hill, and $4\pi M = 21$ kGs. From this expression one can see that for an isochronous cyclotron with $d = 2\pi r/N$, where $N = 4$ is the number of sectors, the azimuthal widths of the valley and hill being equal, the flutter increases with the radius as:

$$F \sim B_N^2 \sim \exp(-2/x),$$

where $x = r / N g_h$. The flutter increases when the hill gap is decreased and decreases with the growth of the number of sectors. The maximum value of the flutter corresponds to the case when the sector and valley widths are the same. In this case, $a = 0.25d$, and $\sin(2\pi a / d) = 1$. For the case of $x < 0.5$, which corresponds to the range of radii $r < 0.5 \cdot N g_h$, the value of the flutter rapidly decreases, and the edge focusing becomes ineffective. For C-80, this effect takes place at radii $r < 15$ cm. These qualitative results are supported with more exact calculations. The precisely calculated flutter versus the radius is presented in Fig. 3 for two variants of the magnetic structure.
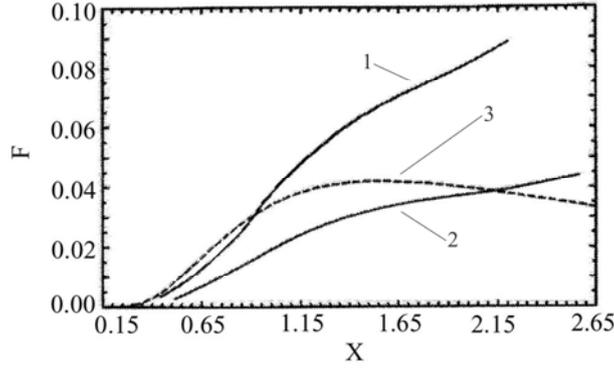
Fig. 3. Flutter as a function of the non-dimensional parameter $x = r/Ng_h$: $1 - 2g_v = 386$ mm, $2g_h = 170$ mm; $2 - 2g_v = 284$ mm, $2g_h = 145$ mm; 3 – approximation of the sector uniform magnetization for the case 1. Here, g_v is a half of the valley gap

3.4. The effect from the spiral pole tips

For acceleration of H⁻ ions, it is advantageous to use a highly spiraled magnetic structure and small variation of the magnetic field from hill to valley. The presence of high spiral angles leads to an increase of the vertical focusing and provides an extra focusing due to angular focusing. It is a standard practice to estimate an increase of the flutter by using the following factor:

$$S(r, \gamma) = 1 + 2 \tan^2 \gamma(r),$$

where $\gamma(r)$ is the spiral angle at the given radius. However, in the real life for a spiral structure with high values of γ and especially for the central region, the benefit in focusing is smaller than it could be expected from this expression. This is explained by a drop of the flutter at small radii and a difference between the spiral angle for the pole tips and that for the magnetic field. The drop of the flutter due to introduction of the spirality can be understood on the basis of simple geometrical considerations [5]. At large values of the spiral angle, the difference between the sector width along the azimuth (AB in Fig. 4) and the sector width A_1B_1 determined along the perpendicular to the middle line, becomes substantial. In the case of straight sectors, the flutter is defined by the edge effect along the azimuth. With introduction of the spirality, the distance between sectors along the line perpendicular to the middle line of a sector becomes smaller than the distance along the azimuth. It leads to a decrease of effective sector and valley widths, and as a consequence to a decrease of the flutter. At middle and large radii, the total effect from the spirality of the magnetic structure connected with an increase of the edge focusing and a decrease of the flutter leads to an increase of focusing. However, the spirality of the magnetic structure decreases the effective width of the sectors and may result at small radii in a drop of the flutter and to a decrease of focusing. The influence of the spiral angle on the flutter value can be estimated with calculations of the flutter for a straight sector (see Fig. 4) if one makes the following replacement: $x_{eff} = x \cos \gamma$. The total effect from the spiral angle can be characterized with the parameter which is a product of the flutter F and the value of $S(r, \gamma)$. Since the flutter rapidly decreases at $x_{eff} < 0.5$, the spirality can result in a decrease of focusing. For each value of the radius and the parameter x, there is a critical spiral angle that results in an increase of focusing from introduction of the spirality. For the spiral angles more than the critical value the vertical focusing decreases. The value of the critical angle for each value of x can be found as a root of the following equation:

$$U(x, \gamma) = (F(x \cos \gamma) / F(x)) \cdot (1 + 2 \tan^2 \gamma) - 1 = 0,$$

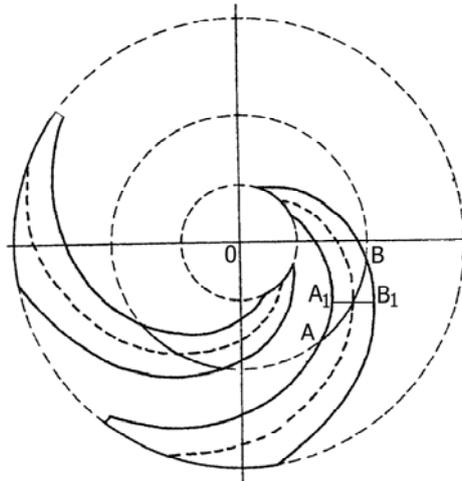where $F(x)$ is a function similar to that shown in Fig. 3.

335

Fig. 4. The difference between the sector width along the azimuth and an "effective" width at large spiral angles. AB – width of a sector along the azimuth; $A_1B_1 \approx AB\cos\gamma$ – an effective width of a sector along a perpendicular to the middle sector line

Figure 5 shows the critical spiral angle versus the radius for the considered accelerator C-80. According to the plot, the spiral structure with high spiral angles has an advantage at $r > 35$ cm, whereas at radii $r < 15$ cm it becomes ineffective. Therefore, it is necessary to use a straight sector structure in the central region, a highly spiraled structure like the spiral of Archimedes being ineffective in this region.
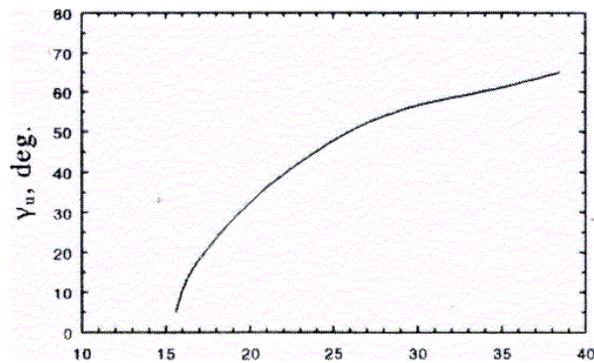
Fig. 5. The critical spiral angle in dependence on radius for $2g_v = 386$ mm, $2g_h = 170$ mm, $r = N \cdot g_h x_{\text{eff},}$, $N = 4$

Another effect, which has been already mentioned, is related to a mismatch of the geometrical and magnetic field spiral angles. For C-80, the maximum mismatch between the magnetic field and geometrical spiral angles is about 7°, which results in a reduction of the edge focusing by up to 30 % at the angles of 65–70°. This effect was noted in [4], and it needs to be taken into account in a design of the magnetic structure of the cyclotron.

4. Features of the chamber and vacuum system

The chamber for the C-80 cyclotron has an unusual design. As has been noted before, successful acceleration of H⁻-ions requires high vacuum of 10^{-7} Torr in the chamber. To achieve such high vacuum, the pumping system involves two cryogenic and one turbo molecular pumps, an external ion source being used. Moreover, in the adopted design the magnetic system with correction shims is placed outside of the vacuum volume. The upper and lower lids of the chamber are attached to the poles of the magnet. Thus, two walls of the chamber (2×16 mm) occupy about 10 % of the magnet gap, which has required to increase the ampere-turns of the magnet winding and the power of the magnet.

5. Beam extraction

The beam extraction is realized with a stripping method. Due to acceleration of H⁻ ions, it is possible to extract 100 % of the beam with intensity of 100 μA and implement a variation of the extracted beam energy from 40 to 80 MeV. The scheme of the extraction system is shown in Fig. 6.
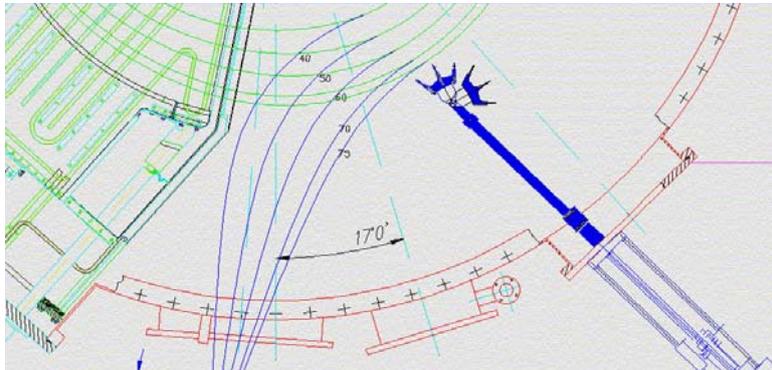

Fig. 6. Schematic view of the extraction system

As is shown in Fig. 6, rays of the extracted beams of different energies come together to a focus point outside of the vacuum chamber in the centre of the correction magnet. This magnet provides matching of the extracted beam with the transport beam line. Figure 7 shows the calculated parameters of the extracted beam. This information can be used as input data to design the beam transport lines.
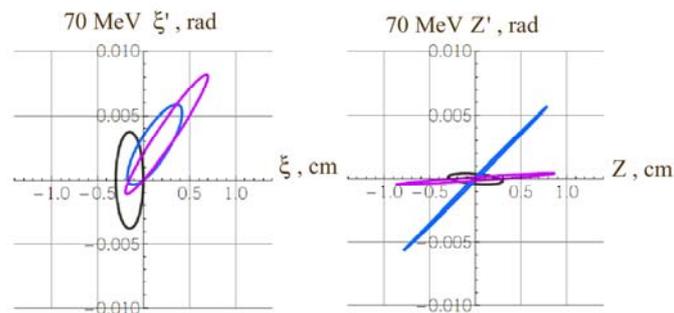
Fig. 7. Phase space ellipses of the extracted beam: black is at the stripping foil, blue is at the input of the correction magnet, and lilac is at the exit of the correction magnet. Here, ζ (ζ') is the horizontal coordinate (angle), Z (Z') is the vertical coordinate (angle)

6. The experimental area

The multy-purpose experimental complex consists of targets of different specialization and beam transport lines. A beam of high intensity is transported to the basement, where three stationary targets are installed for production of medical radioisotopes and pharmaceutical medications: two targets are intended for radiochemical separation methods, and the third target is to be used for separation with the electromagnetic separator as is shown in Fig. 8.
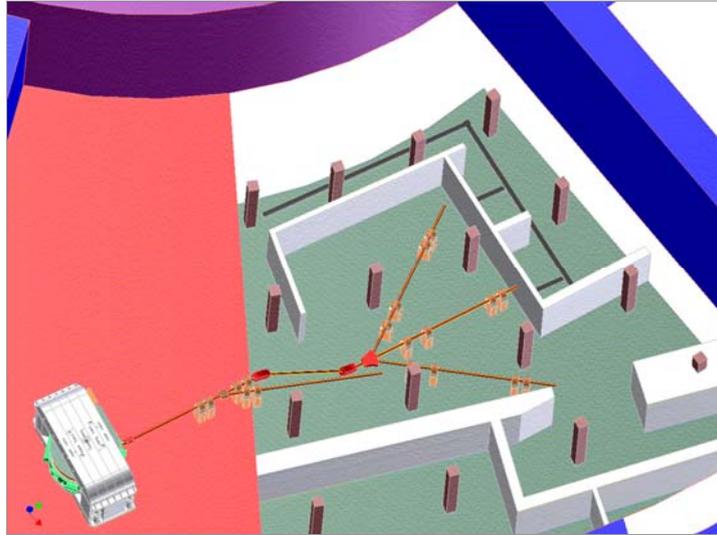
Fig. 8. Transport lines to the targets for production of medical radioisotopes

On the ground floor are disposed an ophthalmology facility with a low intensity beam line and a facility for radiation tests of electronics components with the beam of energies from 20 to 80 MeV.

7. Conclusion

By present, the repair and modernization work of the experimental hall for installation of the cyclotron complex has been completed. The installation and commissioning of the main equipment of the cyclotron is in progress: a power system, a high-frequency generator, a vacuum chamber, an axial injection system and a source, beam probes with a beam diagnostic system, an extraction system with a stripping probe and a correction magnet, and a control system of the cyclotron. Designing and manufacturing of the elements of the beam transport system are in progress. According to the plans, the first beam is expected to be in the end of 2012 or in the beginning of 2013.

References

1. N.K. Abrossimov *et al.*, *Proc. XIII Intern. Conf. on Cycl. and Their Applic.*, Vancouver, Canada, 54 (1992).
2. N.K. Abrossimov *et al.*, RUPAC-XIII, Russia, Dubna **2**, 205 (1993).
3. N.K. Abrossimov *et al.*, RUPAC-XIV, Russia, Protvino **4**, 5 (1994).
4. V.I. Danilov, Preprint JINR-R-**409**, Dubna (1959).
5. N.K. Abrossimov *et al.*, *Proc. XV Intern. Conf. on Cycl. and Their Applic.*, Caen, France, 58 (1997).
6. H.G. Blosser and D.A. Jonson, NIM **121**, 301 (1974).

3D MODELING AND FORMATION OF THE MAGNETIC FIELD
IN THE C-80 ISOCHRONOUS CYCLOTRON

S.A. Artamonov, E.M. Ivanov, G.A. Riabov

1. Introduction

The isochronous cyclotron C-80 which is under construction at PNPI is planned to be used for fundamental researches in nuclear physics, solid state physics and biology, as well as for an applied program – production of medicine isotopes for therapy of eye melanoma and surface forms of cancer. As a first approximation, the magnetic system of the cyclotron C-80 was designed a few years ago on the basis of 2D calculations by using the POISSON program and measurements on two small models [1, 2].

A rather complicated magnetic structure with high spiral angles and a set of 17 correction shims in each of 8 sectors is used in the H⁻ ion isochronous cyclotron C-80. The 3D Novosibirsk code MERMAID was applied to optimize the geometry of the sectors and shims in the hill and valley regions. A precision finite-element model allows taking into account the iron non-linear effects and the detailed magnet geometry. The MERMAID code makes use of about 20.5 million nodes and provides magnetic field calculations with an accuracy of 10–20 Gs. The integral magnetic field parameters (isochronism, transversal motion frequency, H⁻ ion electromagnetic dissociation) have been optimized by using a trajectory analysis. The MERMAID program provides a significant reduction of time and efforts for determination of necessary shims, as compared with a trial-and-error method.

The final version of the C-80 magnetic structure optimized with 3D calculations using the MERMAID program is presented in this report.

2. Main calculation problems

One of the central problems for every isochronous cyclotron is to form the radial and azimuthal magnetic field distribution with required properties. A well designed cyclotron magnet should ensure isochronism for particle acceleration, the magnetic field that provides axial (vertical) and radial (horizontal) focusing of the beam during acceleration, the magnetic field that guarantees an operation point (for cyclotrons it looks like an operation curve) away from dangerous resonances or a fast passage of the beam through the resonance zones, and last, but not least, a possibility to install all cyclotron subsystems.

It is always worth to reduce the number of nodes in the 3D model magnet, which consequently reduces also the time of calculations. This can be done by application of all possible symmetries of the cyclotron magnet. Some magnet details can also be neglected since their influence on the magnetic field in the median plane is very small (*e.g.*, holes for screws on the outer side of the return yoke necessary to handle and fix other cyclotron subsystem elements). Unfortunately, the full model is always required when one wants to study the influence on the magnetic field of different imperfections, such as, for example, a shift and/or rotation of the upper part with respect to the lower part of the cyclotron, a shift and/or rotation of one of the coils with respect to the median plane of the cyclotron, some mechanical defects of one or more poles, *etc*.

Another problem is related with acceleration of H⁻ ions. To reduce H⁻ dissociation losses, a magnetic structure of C-80 with high spiral angles was proposed [3]. Note that the spiral structure provides vertical beam focusing.

It is also necessary to mention an essential mathematical nonlinearity of the problem. In the isochronous C-80 cyclotron, three types of steel are used for the magnetic structure. The main magnet yoke is constructed from a set of two types of steel: steel 3 with the permeability $\mu_3(B)$ (see Fig. 1) and steel 10 with $\mu_1(B)$. The poles are constructed from steel 10 with $\mu_1(B)$. The spiral sectors, 17 correction shims in each of 8 sectors, and the valley shims are constructed from steel 10 with $\mu_2(B)$. In Fig. 1, it is seen that the values of $\mu(B)$ very strongly differ in the working range of magnetic fields of the cyclotron (11000–18000 Gs). It is obvious that this gives rise to additional calculation difficulties and problems for making a 3D model.
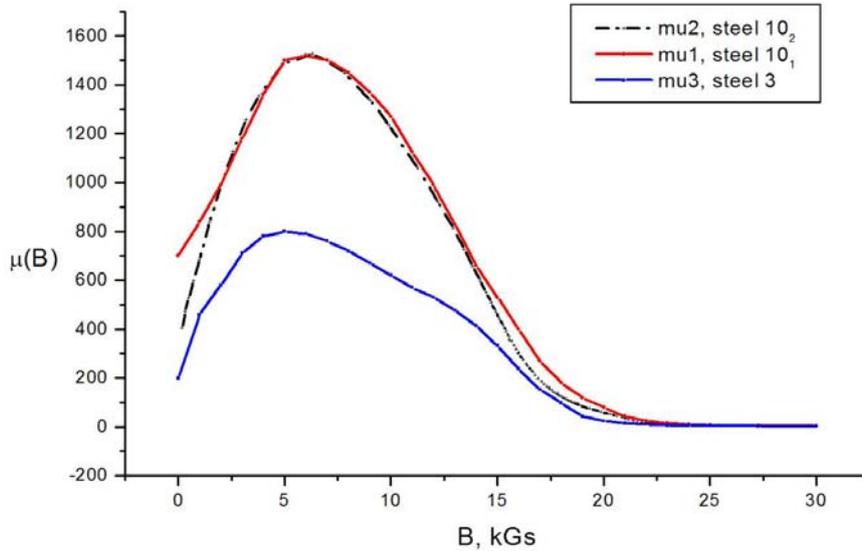
Fig. 1. Permeability curves $\mu(B)$ for the steel used in C-80

3. Magnetic field formation

The selection of magnetic structure parameters and the necessary magnetic field formation for C-80 was accomplished step by step using the program MERMAID [4].

At the first stage, the geometry and the key parameters of the magnetic system for C-80 [5] were fixed. It was supposed that the height of each of the sectors is equal to 90 mm, and during further optimization was not changed. For obtaining the required isochronism, the height of the correction sector shims was varied. The initial height of these shims was selected equal to 20 mm. Besides, in the course of the optimization, a special constrained condition was imposed. It was required that the amplitude of the 4-th field harmonic should not exceed ~ 3000 Gs, and the field near the extraction radius $r = 90$ cm should be $B \leq 17000$ Gs. Under these conditions, the H$^-$ dissociation is below 5 % [3]. For these purposes, additional valley shims were introduced into the magnetic system, and their geometrical parameters were also varied. Thus, the formation of the demanded isochronous field was carried out only by changing the iron shim geometry without using correction coils.

At the second stage, a 3D model of the magnetic system of C-80 was developed and constructed (see Fig. 2). It reproduces accurately the geometry of the magnet yoke, of the sectors (4 pairs), sector shims (17 correction shims in each sector), of the valley shims, the coils current, and the external boundaries. It also takes into account nonlinear magnetic properties of the used electrotechnical steels.

As a rule, 1/8 or 1/4 part of the magnet with the periodic symmetric boundary conditions is used in 3D calculations. Such a model essentially reduces the number of nodes and increases the accuracy of the calculations. In our case, it is impossible to use this approach. Because of a big angular extension of the spiral sectors in C-80, it was necessary to use a half of the magnet with the corresponding symmetry boundary conditions in our calculations. The external boundary of the area where the calculations were performed was chosen rather far to get rid of its influence on the magnetic field in the working region and to determine correctly the fringe field. The fringe field should be taken into account for correct calculations of the extraction beam optics.

Thus, for the description of the magnetic structure of C-80 using the MERMAID program, about 20.5 million direct prisms were required, which allowed us to reach the necessary precision of 10^{-3}–10^{-4} in the calculation of the magnetic field.
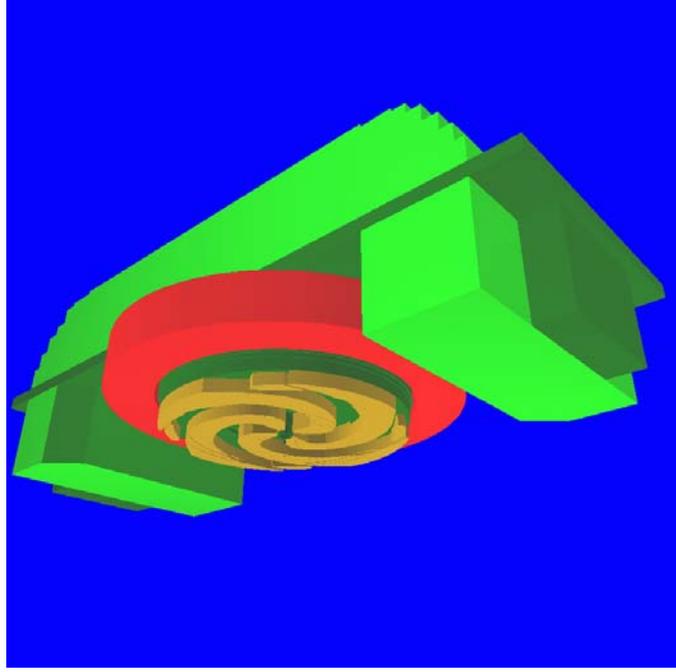
Fig. 2. MERMAID model of C-80

Our three-dimensional model is close to the reality. Therefore, the results of magnetic field measurements are expected to be close to the results of calculations. Our experience is that using the MERMAID software one can expect a difference of 10–20 Gs between the calculated and measured magnetic field values. These field differences can be explained by not sufficient precision of the software, by uncertainties in the permeability curves $\mu(B)$, and by some small geometrical differences between the model and the real cyclotron magnet.

4. Algorithm of optimization

The developed computing model was used for simulations of the necessary spatial distribution of the C-80 magnetic field $B_z(z,r,\theta)$ and for its subsequent analysis. As is well known, the cyclotron magnetic field at the given radius r, having the N-fold rotational symmetry, can be presented as a Fourier series

$$B_z(z=0, r, \theta) = \overline{B}(r)\left\{1+\sum_{n=1}^{\infty}\left[a_n(r)\cos(nN\theta)+b_n(r)\sin(nN\theta)\right]\right\}=$$

$$= \overline{B}(r)\left\{1+\sum_{n=1}^{\infty}A_n(r)\cos nN\left[\theta-\psi_n(r)\right]\right\},$$

where N is the number of symmetry periods of the cyclotron ($N = 4$ in our case),

$$a_n, b_n, A_n = \sqrt{a_n^2+b_n^2}\ \text{ are the coefficients of the Fourier series,}$$

$$\psi_n(r) = \frac{1}{n}\text{arctg}\frac{b_n(r)}{a_n(r)}\ \text{ is the phase of the } n\text{-th harmonic,}$$

$$\overline{B}(r) = \frac{1}{2\pi}\int_0^{2\pi}B_z(r,\theta)d\theta\ \text{ is the magnetic field averaged over the azimuth.}$$

The magnetic field flutter F at the radius r can be defined as

$$F = \frac{\overline{B^2}-\overline{B}^2}{\overline{B}^2} = \frac{1}{2}\sum_{n=1}^{\infty}A_n^2, \quad \overline{B^2} = \frac{1}{2\pi}\int_0^{2\pi}B_z^2(r,\theta)d\theta.$$

341

The procedure of the magnetic field optimization was divided into two stages. At the first stage, the isochronous field (the averaged over the azimuth magnetic field necessary for isochronous particles acceleration) and the betathron frequencies were estimated using analytical formulas from [6]. Namely, the betathrone frequencies were approximated by the following equations:

$$\nu_z^2 = -k + F + \frac{1}{2(N^2-1)}\left[A_N^2(1+(2N^2-1)\mathrm{tg}^2\gamma) - A_N A_N' - A_N'' A_N \right] + \frac{(A_N')^2}{2N^2},$$

$$\nu_r^2 = 1 + k + \frac{1}{2(N^2-1)(N^2-4)}\left[6N^2 F(1+\mathrm{tg}^2\gamma) + (5N^2-8)A_N A_N' \right] + \frac{A_N'' A_N}{2(N^2-1)} + \frac{(A_N')^2}{2(N^2-4)},$$

where ν_z is the axial (vertical) betathron frequency, ν_r is the radial (horizontal) betathron frequency, $k = \dfrac{r}{\overline{B}(r)}\dfrac{d\overline{B}(r)}{dr}$ is the radial field index, $A_N' = r\dfrac{dA_N}{dr}$ and $A_N'' = r^2\dfrac{d^2 A_N}{dr^2}$ are the first and second derivatives of the A_N harmonic amplitude, $\mathrm{tg}\gamma = r\dfrac{d\psi_N(r)}{dr}$, γ is the sector spiral angle (the angle between the radius vector at radius r and the tangent to the pole tip edge at this radius).

Ions motion should be synchronized with a given phase of the cyclotron RF system during acceleration. Therefore, the magnetic field in the cyclotron should ensure a constant rotation period of ions $T = 2\pi/\omega_0$. As was mentioned above, the magnetic field with this feature is called isochronous. This field can be approximated by the following equation:

$$\overline{B}_{\mathrm{isochr}}(r) = \frac{B_0\tau(r)}{\sqrt{1-\dfrac{r^2\tau^2(r)}{R_c^2}}},$$

where

$$\tau(r) = 1 - \sum_{n=1}^{\infty} \frac{A_{Nn}^2 + A_{Nn}\,A_{Nn}'}{\left[(Nn)^2-1\right]},$$

$R_c = c/\omega_0 = $ const, c is the light velocity, $\omega_0 = \dfrac{qB_0}{m_0 c}$, q is the particle charge (in units of the electron charge), B_0 is the magnetic field in the centre of the cyclotron, m_0 is the rest mass of the particle under acceleration.

The aim of the magnetic field optimization is to make the value $\Delta B = \overline{B}(r) - \overline{B}_{\mathrm{isochr}}(r)$ as small as possible at each radius r. For the purpose of receiving the minimum difference between the calculated average field $\overline{B}(r)$ and the estimated isochronous field $\overline{B}_{\mathrm{isochr}}(r)$, some geometrical changes were made in the 3D model (with a control of other required characteristics of the cyclotron). Such an approach is rather simple and fast, but it doesn't possess the sufficient accuracy for an isochronous cyclotron.

At the second stage, a full particle trajectory analysis was carried out. Namely, we solved numerically the relevant nonlinear equations describing the particles movement:

$$r'' = r + 2\frac{r'^2}{r} + \frac{q\sqrt{r'^2+r^2+z'^2}}{\sqrt{E^2-E_0^2}}\left[B_z(r+\frac{r'^2}{r}) - B_r\frac{r'z'}{r} - B_\theta z' \right],$$

$$z'' = 2\frac{r'z'}{r} + \frac{q\sqrt{r'^2+r^2+z'^2}}{\sqrt{E^2-E_0^2}}\left[B_z\frac{r'z'}{r} - B_r(\frac{z'^2}{r}+r) + B_\theta r' \right],$$

$$B_r = \int_0^z \frac{\partial B_z}{\partial r}dz = \frac{\partial B_z}{\partial r}z,$$

$$B_\theta = \frac{1}{r}\int_0^z \frac{\partial B_z}{\partial \theta}dz = \frac{\partial B_z}{\partial \theta}\frac{z}{r}.$$

342

Here E and E_0 are the total energy and the rest mass of the particle (in MeV); r', r'', z' and z'' are derivatives of r and z over θ. The orbit will be an equilibrium one if the periodic initial conditions are as follows:

$$r_{\text{eq}}(2\pi) = r_{\text{eq}}(0), \quad r'_{\text{eq}}(2\pi) = r'_{\text{eq}}(0).$$

In the first approximation, an analytical formula from [6] was used for $r_{\text{eq}}(\theta)$ near $r = r_k$:

$$r_1(\theta) = r_k \left\{ 1 + \sum_{n=1}^{\infty} \frac{A_{Nn}}{(Nn)^2 - (1+k)^2} \cos Nn[\theta - \psi_{Nn}] - \right.$$
$$\left. - \sum_{n=1}^{\infty} \left[A_{Nn}^2 \frac{3(Nn)^2 - 2}{4[(Nn)^2 - 1]^2} + \frac{A_{Nn} A'_{Nn}}{2[(Nn)^2 - 1]} \right] \right\}.$$

The expression for $r'_1(\theta)$ can be received from $r_1(\theta)$ if one differentiates it over θ.

A special procedure allowed us to determine the so-called static equilibrium orbits, more precise values of the time of particle revolutions at different radii, the betathron frequencies, the H^- ions losses due to electromagnetic dissociation, and the value of the isochronous field (details see in [7]). This new more precise value of the isochronous field was compared with the magnetic field averaged over the azimuth. If it was necessary, geometrical corrections of the magnetic structure were repeated in order to minimize the difference between the calculated average and the isochronous fields. Such iteration procedures were repeated until the difference between the average 3D field and the isochronous one (calculated at the second stage) became less than 20 Gs.

The C-80 magnet structure optimization was realized for a number of minimum magnet gaps: 146, 156, 170, 176 and 164 mm.

5. Main results of the calculations

The final version of the magnetic structure for the isochronous cyclotron C-80 was chosen for a minimum gap equal to 164 mm. The optimum 3D magnetic field is presented on Fig. 3.
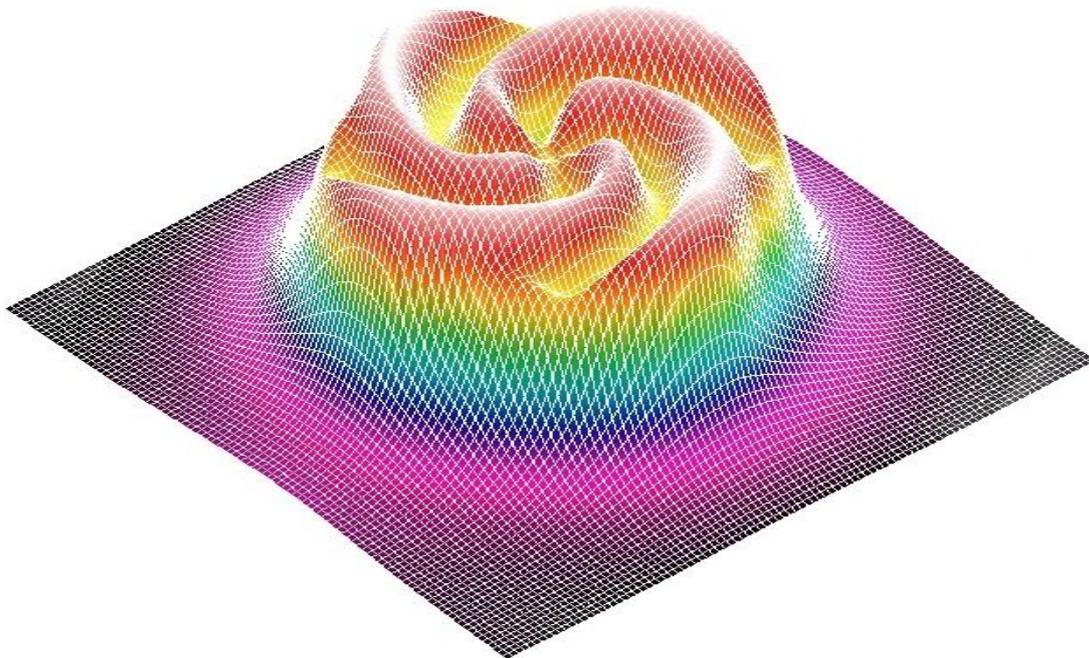

Fig. 3. 3D MERMAID magnetic field for C-80

The results of 3D magnetic field calculations provide information about the magnetic field in any point of the model and around it. Very often they are used to make magnetic field maps in the cyclotron magnet median plane or in three dimensions around this plane. Such a magnetic field map becomes a part of the input data for programs calculating the trajectories of particles and for programs calculating properties of the magnetic field, for example, the equilibrium orbit codes [7].

Briefly, we will enumerate main modifications of the initial magnetic system [1, 2] executed on the basis of 3D simulations. The direct sectors were prolonged from the radius of 27 cm to the radius of 40 cm, but with two turns at fixed angles, keeping the previous sector widths along the azimuth the same (see Fig. 4). It led to blocking of an uncontrollable penetration of the magnetic spiral angle to the area near the central region. Thereby, a growth of the amplitude of the main harmonic was provided which led to stable motion of particles in this area. For reduction of the number of valley shims, the azimuthal expansion of the sectors was made by ~ 20 mm from the radius of 70 cm to the final radius of 102.5 cm (see Fig. 4). It allowed to reduce the number of the valley shims in each valley from four in the initial magnetic system to one in the final version.

The dashed and solid blue lines in Fig. 4 show the old and new geometry of a C-80 sector, respectively. The red line is the central line of the sector. The central region was changed in the 3D C-80 model so that to consider the real geometry of the system with an axial injection. Besides, by means of a magnetic plug, a necessary fall of the magnetic field in the central region was ensured.

It is necessary to emphasize that the proposed modification of the magnetic system allowed to receive stable axial and radial motion of the accelerated ions in all working area of the C-80 cyclotron. A preliminary numerical study of resonances in the cyclotron acceleration system has also been performed. For this purpose, the data presented in Fig. 5 were used. The operation point (v_r, v_z) moves as the particle kinetic energy increases and can cross the resonance curves shown in Fig. 5. Resonances are dangerous when the crossing of these resonances is slow (when the kinetic energy gain per turn is small). On the other hand, if the passage through the resonance zones is fast, then the quality of the beam becomes only slightly worse.
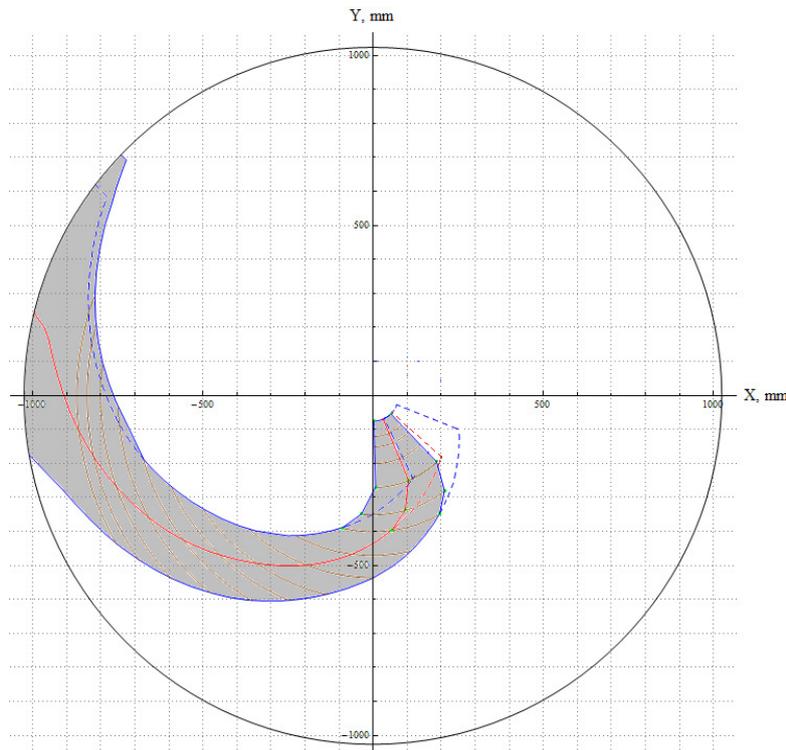

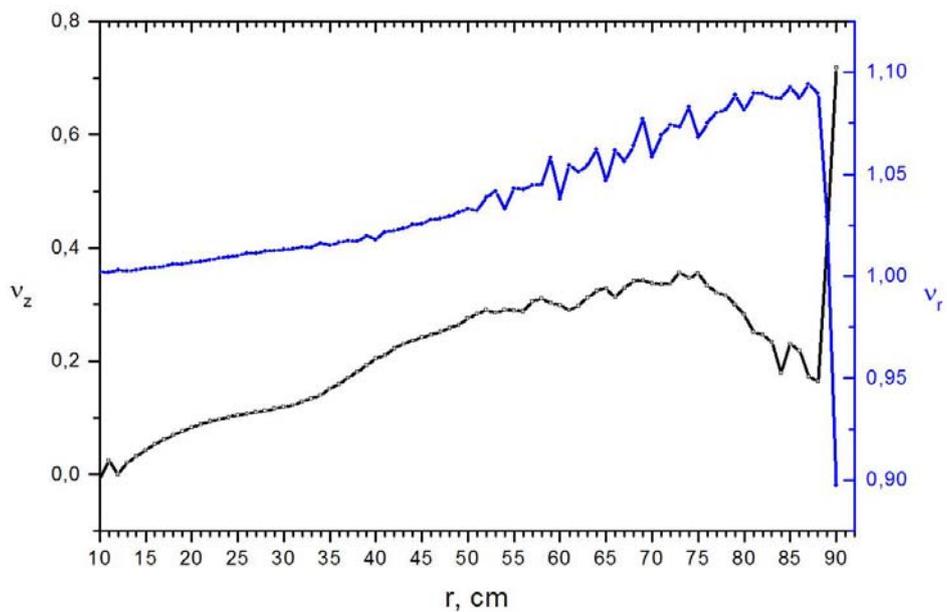**Fig. 4.** Modification of C-80 sectors

Fig. 5. Horizontal v_r (the upper curve) and vertical v_z betathron frequencies (the numbers of oscillations per turn) in C-80

The performed changes of the magnetic structure led also to a decrease to 2.2–2.5 % of losses of the H⁻ ions dissociation in the course of acceleration. The final proposed magnetic structure for the C-80 cyclotron is shown in Fig. 6.

Fig. 6. View of the pole tip for the cyclotron C-80

345

6. Conclusion

A careful analysis of the 3D data on the magnetic field, performed with the method described in detail in [7], has shown that practically all problems of the isochronous cyclotron C-80 under construction have been overcome. The betathrone frequencies are acceptable in all working area of the cyclotron. However, most likely, small corrections of the isochronous field will be required, depending on the measurements to be done. The final distribution of the magnetic field is planned to be measured with a 2–6 Gs precision when the sectors will be mounted.

According to the results of simulations of the 3D magnetic field and particles trajectory calculations, it is possible to state that the last version of the magnetic structure of the isochronous C-80 cyclotron meets all design requirements.

References

1. N.K. Abrossimov, S.A. Artamonov, V.A. Eliseev, G.A. Riabov, "Design and Optimization of the Magnet and Magnetic Structure for the 80 MeV H¯ Isochronous Cyclotron", Proceeding of the Second International Workshop: Beam Dynamics & Optimization – BDO, 1995, St.-Petersburg, Russia, 7 (1995).
2. N.K. Abrossimov, S.A. Artamonov, V.A. Eliseev, G.A. Riabov, "Design and Modelling of the Spiral Magnetic Structure for 80 MeV H¯ Isochronous Cyclotron", Proceeding of the XV International Conference on Cyclotron and Their Application, Caen, France, 518 (1998).
3. N.K. Abrossimov, S.A. Artamonov, V.A. Eliseev, G.A. Riabov, "Losses of H¯ Ions Due to Electromagnetic Dissociation and Their Effect on Selection of Isochronous Cyclotron Magnetic Structure", PNPI Research Report 1994–1995, Gatchina, 275 (1996).
4. S.N. Andrianov, S.A. Artamonov, A.N. Dubrovin, V.A. Eliseev, "Computer Simulation of the 3D Magnetic Field of the PNPI Isochronous Cyclotron" (in Russian), Vestnik SPbSU, ser. 10, iss. **3**, 12 (2008).
5. G.A. Riabov *et al.*, "Design Features of the 80 MeV H¯ Isochronous Cyclotron in Gatchina", these proceedings.
6. Yu.G. Basargin, V.P. Belov, "Some Problems of Particle Motion Dynamic in Cyclotrons with Spatially Variable Fields", Electrofisicheskaya Apparatura (in Russian), **3**, Moscow, Atomizdat, 3 (1965).
7. S.N. Andrianov, S.A. Artamonov, "Optimal Algorithm for Forming an Isochronous Magnetic Field in Accelerators with Azimuthal Variation" (in Russian), Vestnik SPbSU, ser. 10, iss. **2**, 3 (2009).

DEVELOPMENT OF TARGETS FOR THE RIC-80 PROJECT

**V.N. Panteleev, A.E. Barzakh, D.V. Fedorov, A.M. Filatova, V.S. Ivanov,
K.A. Mezilev, F.V. Moroz, P.L. Molkanov, S.Yu. Orlov**

1. Introduction

The rapidly growing studies in nuclear physics, developments of experimental methods and implementation of very sensitive and effective detectors have provided a very good possibility for development of a completely new direction in medical diagnostics and therapy of diseases, which is presently known as nuclear medicine. The exceptional ability of nuclear medicine methods is based on the possibility to detect and treat a large set of diseases at a very early stage, saving human lives and reducing expenses for treatment. The technology of nuclear medicine used for diagnostics and therapy is based on employing radioactive isotopes with selected properties. The common methods in nuclear diagnostics use the technology of marking medications by specific radionuclides. By measuring the distribution of radioisotopes in the human body, it is possible to observe the functions of the investigated organs or their parts. Similar methods are used for treatment of malignant tumors. In this case, the compounds containing radioactive isotopes are absorbed by malignant formations, which leads to their local irradiation and subsequent destruction. The main advantage of nuclear radiomedicine methods is that the diagnostics and treatment can be carried out at very early stages of the disease.

This work is the first part of the program of the target development for the new project of RIC-80 (Radioactive Isotopes at the cyclotron C-80) [1], which is presently being carried out at PNPI. The main task of this work is the development of methods of production and separation of the isotope-generator ^{82}Sr, which is used for PET diagnostics of heart diseases, and also of some other isotopes used for diagnostics and therapy. The methods are worked out using a 1 GeV proton beam of the synchrocyclotron with the aim to use the developed target prototypes at the new radioisotope facility RIC-80 with the proton energy of 80 MeV and the beam intensity of up to 200 µA.

2. Description of the experiment and experimental results on production of ^{82}Sr

In the first experiments, niobium foils were used as target material for production and yield measurements of ^{82}Sr. This nuclide with the half-live $T_{1/2} = 25.55$ days is the generator for its daughter isotope ^{82}Rb ($T_{1/2} = 1.25$ min), which is widely used in PET diagnostics.

A stack of niobium foils of 16 g/cm^2 thickness was placed into a Ta-W container which was designed as a prototype of the target device for production of ^{82}Sr at RIC-80. Results of FLUKA [2, 3] calculations of the ^{82}Sr activity produced in the irradiated Nb and Zr targets are presented in Fig. 1.
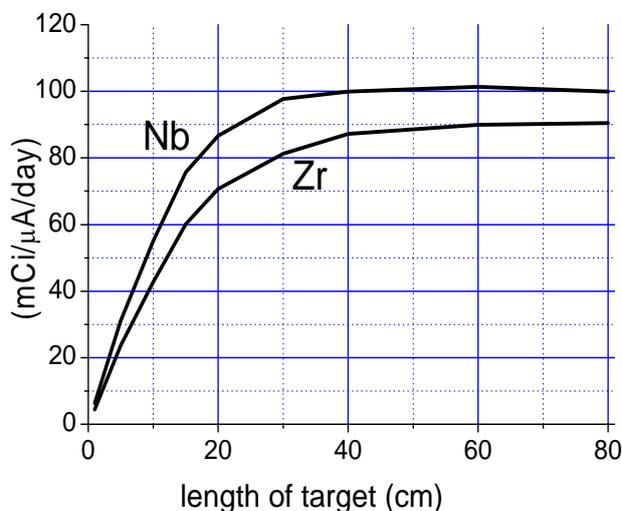

Fig. 1. ^{82}Sr radioactivity produced in the Nb or Zr foil target *vs* target length. The activity value is in mCi; the proton energy is 1 GeV; the proton beam intensity is 1 µA; the irradiation time is 24 hours

One can see in Fig. 1 that even with a rather low current of the PNPI synchrocyclotron (up to 1 µA), it is possible to obtain about 0.5 Ci of ^{82}Sr after 5 day irradiation of a target of the appropriate length of 30 cm.

For irradiation and target heating tests, the target prototype was manufactured with the parameters close to those specified for the target of the RIC-80 facility, which were the following: the target material – Nb foils of 25 mm in diameter; the target thickness – 16 g/cm^2; the length of the target container – 200 mm; the cylindrical container of Ta-W alloy – 30 mm in diameter. A target prototype (shown in Fig. 2) was fabricated for irradiation by the proton beam to accumulate ^{82}Sr in the target material.
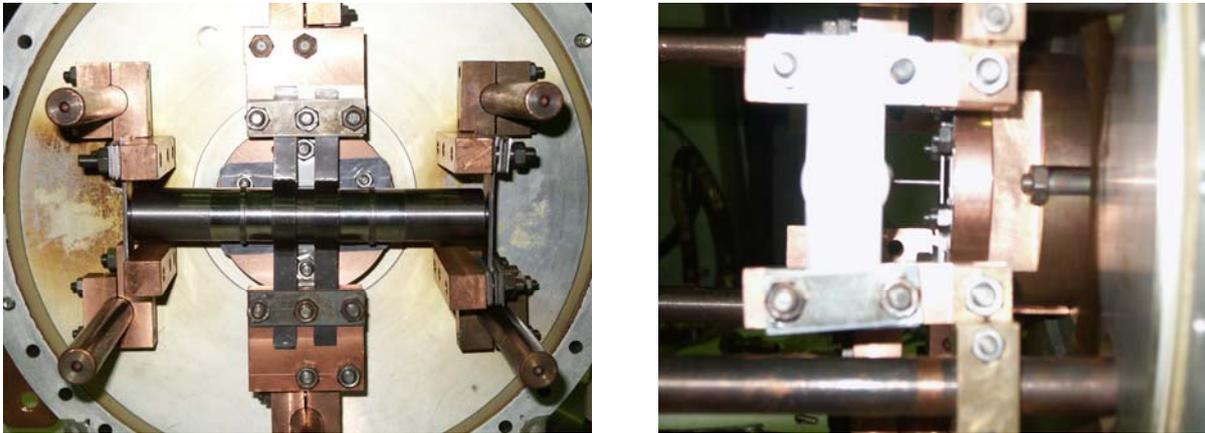
Fig. 2. Target prototype constructed for tests of production and thermal extraction of the generator isotope ^{82}Sr from the irradiated niobium foil target

The proton beam was directed along the target container with a stack of niobium foils. In the central part, the target container was connected to a tungsten tube with a hole of 2 mm in diameter. The radioactive nuclides accumulated in the target material were evaporated through this tube in the course of the target heating up to 2100 °C and were absorbed by the tantalum foil collector, which was placed in contact with the copper flange cooled by water. For the tungsten tube, along which the evaporated nuclides passed through, the same method of heating was used as that for the target container. Before irradiation by the proton beam, the container was installed and tested at a test bench. The target was heated up to its working temperature of 2000–2100 °C and subsequently cooled down, and this procedure was repeated many times under vacuum of 10^{-5} Torr.
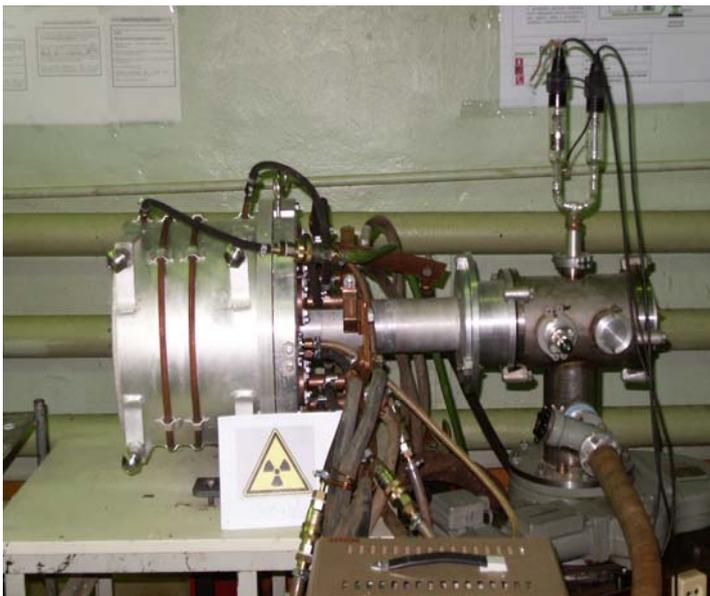

Fig. 3. Vacuum test bench with the investigated target installed. The target itself is inside of the water cooled aluminum vacuum container

The target heating tests demonstrated that the repeated process of target heating and cooling had not caused any noticeable changes of such target parameters as the shape of the target container, its position and electric resistance. The thermal investigations of the target confirmed the results of our earlier tests with high-temperature and high-density uranium carbide target units investigated in the same temperature conditions [4]. Figure 3 shows the vacuum test bench constructed for testing high-temperature targets with the heating power of up to ~ 9 kW. The parameters of the test bench heating system are the following: the current through the target is up to 1100 A; the voltage drop on the target container is up to 8 V; the target heating power is up to 8.8 kW. This target construction provides production and extraction of radionuclides from diverse target materials such as refractory metal foils, refractory metal carbides and liquid metals.

The constructed target device was installed in the PNPI synchrocyclotron proton beam for irradiation with the beam intensity of 0.1 μA during 24 hours. After two weeks of radiation cooling (the time interval for decay of short-lived isotopes), the target unit was transported to the experimental hall of the IRIS facility and placed on the test bench for ^{82}Sr extraction by target heating. Figure 4 presents the gamma-spectrum measured by an ultrapure germanium detector placed at a three-meter distance from the irradiated target before its heating started.
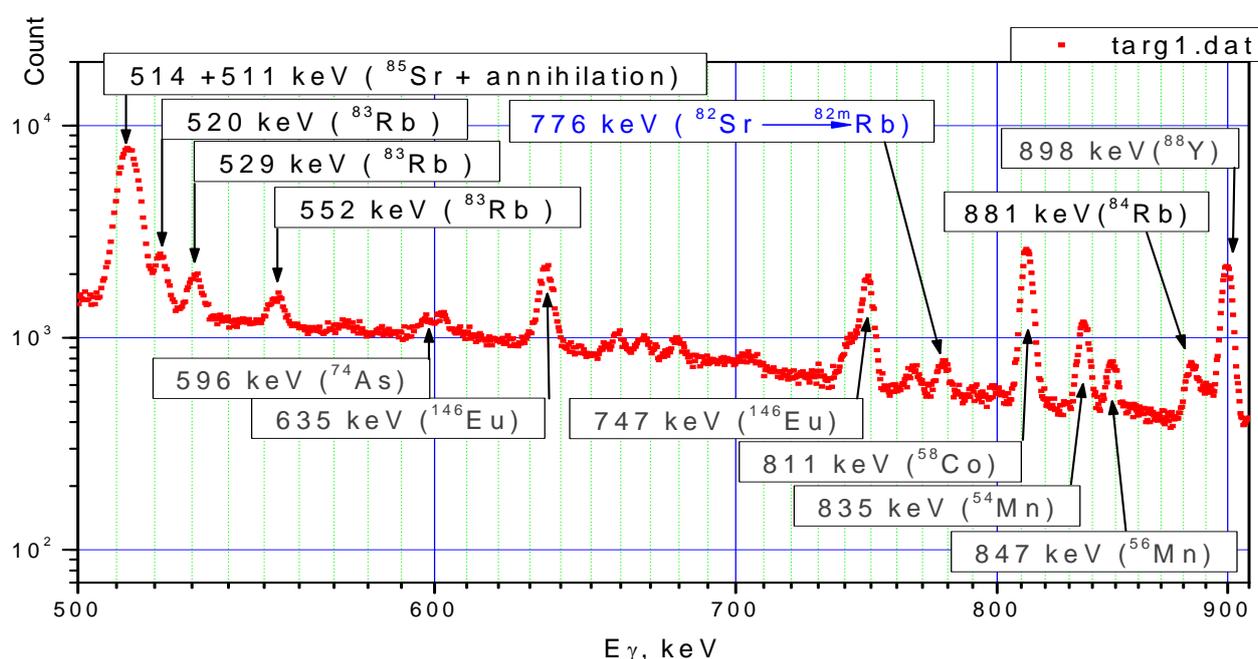
Fig. 4. Gamma-spectrum of the irradiated niobium foil target. The gamma-line of 776 keV belongs to the decay of ^{82}Sr daughter isotope ^{82}Rb used for PET diagnostics

To extract the radioactive species produced in the target material, there were several stages in the process of target heating in high vacuum. Since strontium is released from the target by relatively slow diffusion and effusion processes, the target heating was started at low temperatures of 1500–1800 °C to evaporate Rb, Mn and other radionuclides with low values of diffusion-effusion parameters. The gamma-spectrum of the radioactive species extracted from the target during two hours of heating at 1500 °C and deposited on a tantalum collector is shown in Fig. 5.

One can see in Fig. 5 that only the isotopes of easily diffusing and volatile elements (Rb, Mn) escape the target at the temperature of 1500 °C. The gamma-spectrum of radioactive species collected at the tantalum foil is shown in black; the red points show the gamma-spectrum of these radioactive species washed out of the foil-collector by alcohol. The efficiency of washing out Rb and Mn from the surface of the tantalum foil collector by alcohol was about 30 %. In the collected radioactive matter, no traces of ^{82}Sr are seen. It means that at this temperature all volatile species can be removed from the target in a rather short time (6–8 hours) without losses of strontium. After that, strontium can be selectively extracted by heating the target to higher temperatures.
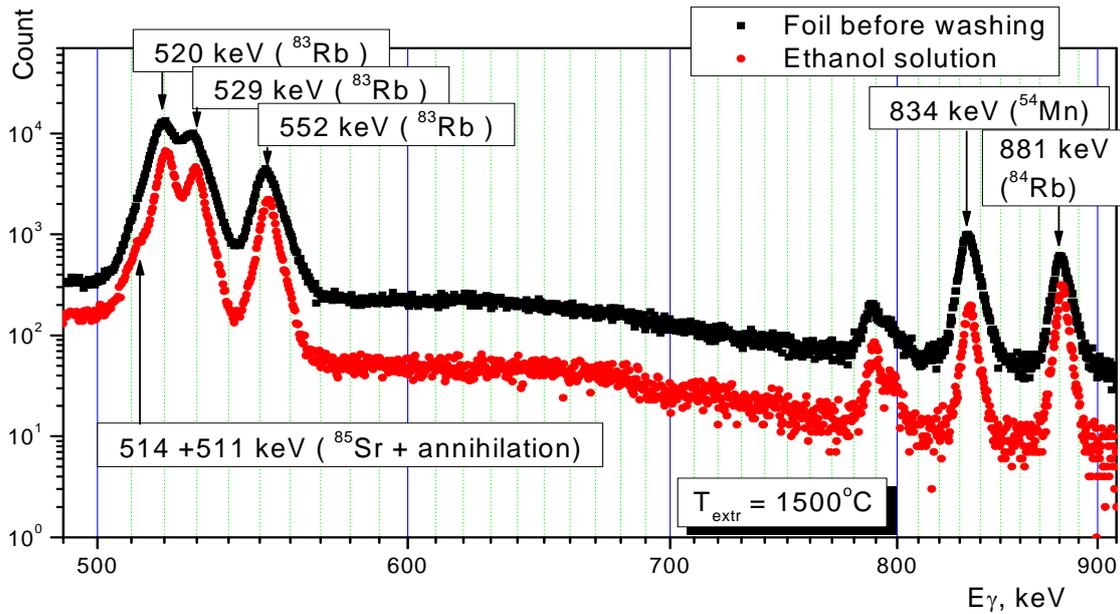
Fig. 5. Gamma-spectra of the radioactive species extracted from the target during two hours of heating at 1500 °C and deposited on a tantalum collector

The gamma-spectrum of the species collected at the temperature of 2000 °C after the target heating during 8 hours at the temperature of 1500–1600 °C is shown in Fig. 6. As one can see, all the radioactive species were finally evaporated from the irradiated target, except for strontium. The efficiency of washing out strontium from the tantalum foil collector by a solution of HNO_3 acid was 70 %. During the target heating at the temperature of 2000 °C, 93 % of ^{82}Sr was removed from the target in ten hours, with 65 % collected on the tantalum foil and 70 % transferred to the acid solution. Thus, we can estimate that the integral efficiency of our first experiment on ^{82}Sr production was 42%.
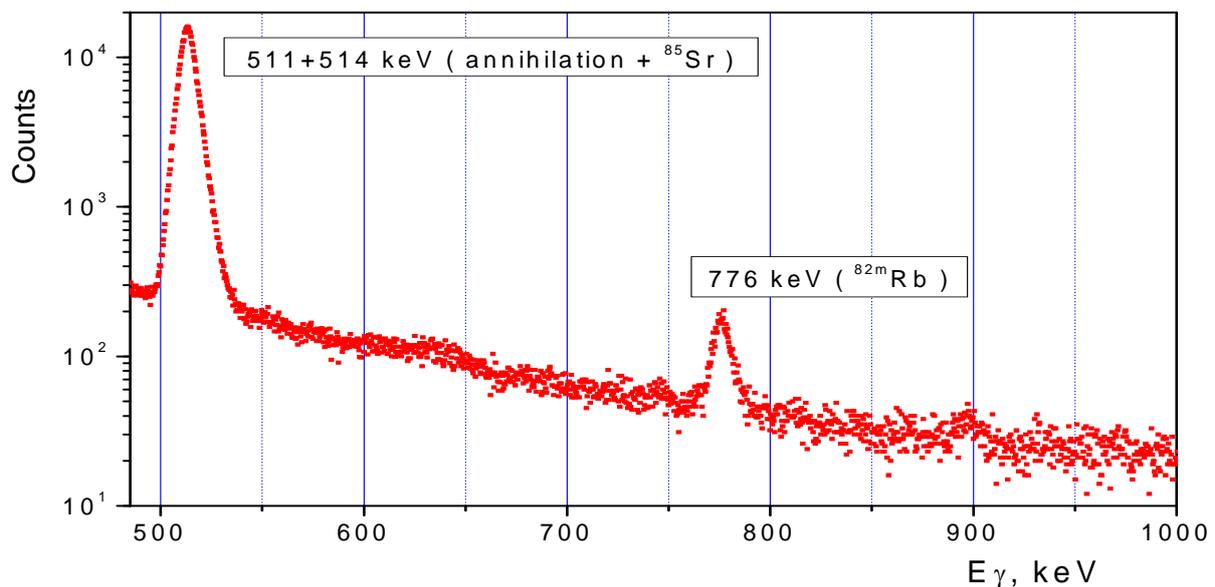
Fig. 6. Gamma-spectrum of the species collected at 2000 °C after target heating for 8 hours at 1500–1600 °C to evaporate the volatile species. During this heating process, the gamma spectrum of the collected active matter was measured every 2 hours to control that strontium did not escape

350

3. Production of thallium isotopes from a Pb target

The radionuclide ^{201}Tl ($T_{1/2}$ = 3.04 d) is used for diagnostics of myocardial diseases. It can be effectively produced from lead targets of natural or enriched abundance. The cross section for production of ^{201}Tl from a lead target is presented in Fig. 7.
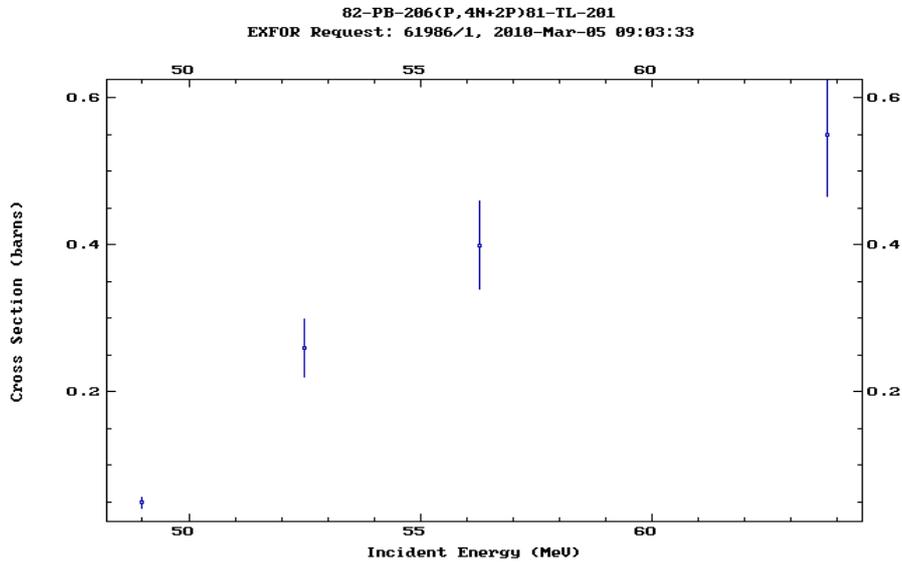

82-PB-206(P,4N+2P)81-TL-201
EXFOR Request: 61986/1, 2010-Mar-05 09:03:33

Fig. 7. Dependence of the cross section for production of ^{201}Tl from ^{206}Pb on the incident proton beam energy

One can see in Fig. 7 that the production cross sections are very high and, hence, this method can be used for effective production of ^{201}Tl. The only problem is the admixture of the neighbour isotopes with similar half-lives, ^{200}Tl ($T_{1/2}$ = 1.09 d) and ^{202}Tl ($T_{1/2}$ = 12.23 d). In this case, the mass-separator method of production of high purity ^{201}Tl can be used.

In the experiment on production and extraction of thallium isotopes, the target of 1 g lead of natural abundance was irradiated by the 1 GeV proton beam of the PNPI synchrocyclotron for 24 hours. After 10 days of cooling, it was transported to the experimental hall of the IRIS facility and was placed on the vacuum test bench into a tungsten container to be heated. The gamma-spectrum of the irradiated lead sample before its heating is shown in Fig. 8.
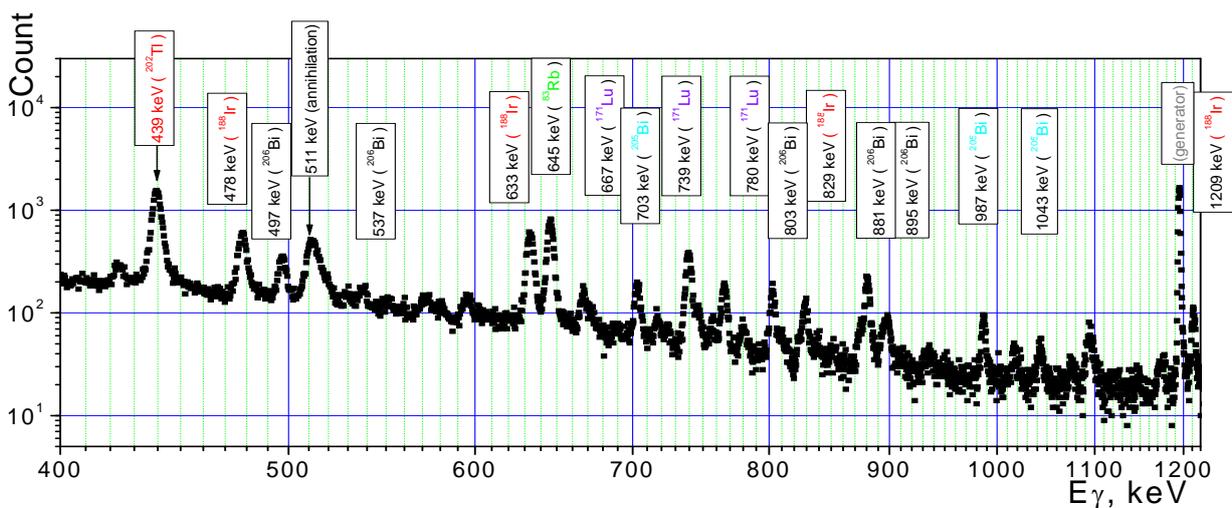

Fig. 8. Gamma-spectrum of the irradiated 1 g lead sample of natural abundance after 10 days of radiation cooling. The gamma-line of 439 keV is from the decay of ^{202}Tl ($T_{1/2}$ = 12.23 d)

The main goal of the first experiment on Tl isotopes production from a lead target was to figure out the heating conditions for selective Tl extraction from the irradiated lead sample. It was expected that thallium, which is a very volatile element, has the rate of evaporation from the melted lead target material exceeding that of other radioactive species. Since the melting point of lead is 327 °C, the extraction was carried out at 400 °C to make sure that the lead sample was completely melted. The gamma-spectrum of the species evaporated at 400 °C from the lead sample and deposited onto the cooled tantalum collector is shown in Fig. 9.
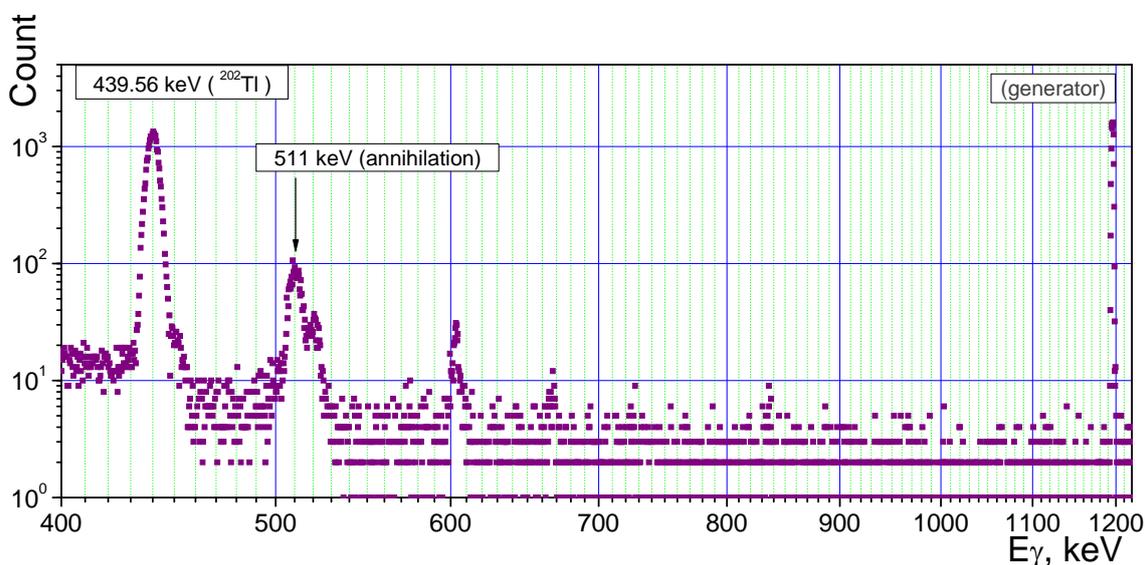
Fig. 9. Gamma-spectrum of the species evaporated at 400°C from the lead sample and condensed on a cooled tantalum collector. The time of evaporation was 2 hours

Comparing the gamma-spectra in Figs. 8 and 9, we see that the selective evaporation of thallium from the melted lead target is very fast. In two hours of heating, about 80 % of ^{202}Tl escaped from the target and was absorbed by the collector. In this case, the situation is very different from the case of strontium extraction, where the target material (niobium foils or yttrium carbide for RIC-80) had to be heated up to 2000 °C.

4. Production of alpha decaying radium isotopes from a uranium carbide target

Radionuclides decaying by alpha particle emission can be a very effective tool for therapy of malignant tumors at very early stages of their formation. The main advantage of alpha particles (the so called "alpha-knife") is their very short range (60–80 µm) in biological tissue, which is very important for treatment of small malignant formations. The action of radionuclides emitting alpha particles is very effective, as it is very local and does not destroy the surrounding tissues. Among the alpha decaying radionuclides that can be used for therapy, there are two isotopes – ^{223}Ra ($T_{1/2} = 11.4$ d) and ^{224}Ra ($T_{1/2} = 3.66$ d) – that can be effectively produced by proton irradiation of uranium or thorium targets. The cross section for ^{227}Th production from a thorium target [5] is presented in Fig. 10.

This nuclide has a rather high value of the cross section for production in the spallation reaction for the case of a natural ^{232}Th (100 %) target and the proton beam with the energy close to 80 MeV. The subsequent alpha decay of ^{227}Th produces ^{223}Ra:

$$^{227}\text{Th}(18.7 \text{ d}) \rightarrow {}^{223}\text{Ra}(11.4 \text{ d}) \rightarrow {}^{219}\text{Rn}(3.96 \text{ s}) \rightarrow {}^{215}\text{Po}(1.8 \text{ ms}) \rightarrow {}^{211}\text{Pb}(36.1 \text{ min}) \rightarrow$$

$$\rightarrow {}^{211}\text{Bi}(2.14 \text{ min}) \rightarrow {}^{207}\text{Tl}(4.77 \text{ min}) \rightarrow {}^{207}\text{Pb}(\text{stable}). \tag{1}$$
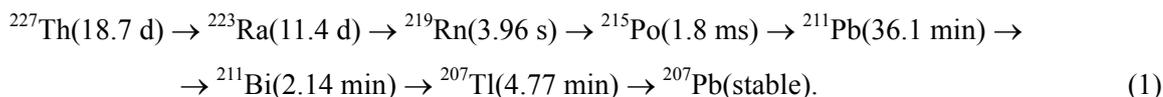
In the decay chain presented above, the decay of the selected ^{223}Ra produces three alpha particles and considerably increases the efficiency of therapy.
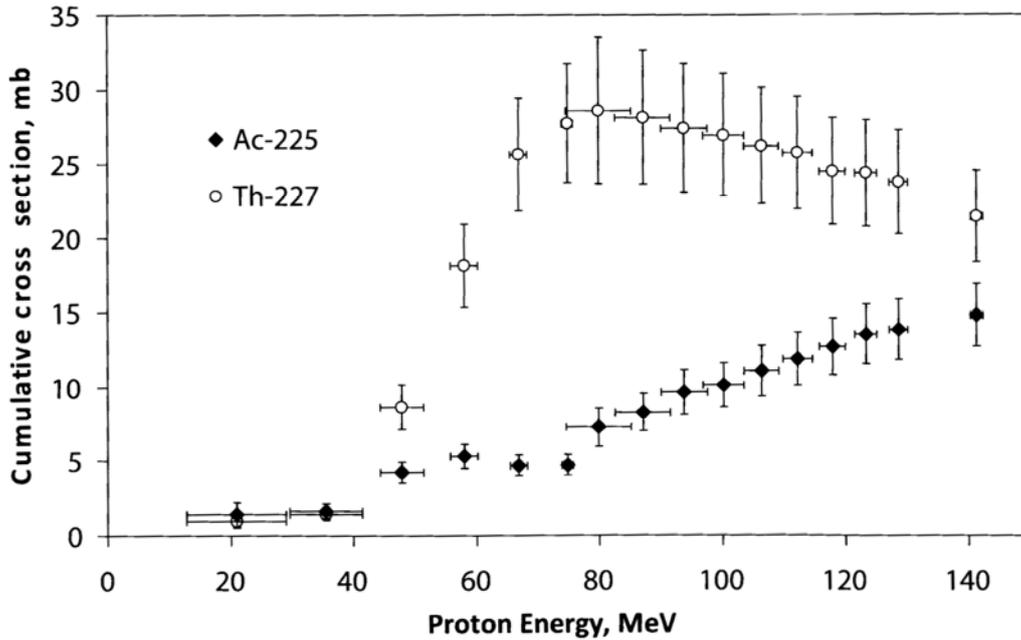
Fig. 10. Cross sections for ^{227}Th production in a thorium target *vs* the energy of protons. The open circles show the cross section for ^{225}Ac production

In our experiments, we used a ^{238}U target (uranium monocarbide of high density [6]) for production and high temperature extraction of radium isotopes. The Uranium Carbide (UC) target with the density of 11 g/cm^3 was irradiated by the proton beam with the intensity of 0.1 µA for 24 hours at the PNPI synchrocyclotron. The target mass was about 1 g. After two months of radiation cooling, the target was placed into the heating tungsten container on the vacuum test bench. The radium isotope extraction was carried out at the temperature of about 2400 °C, which is close to the melting point of the uranium monocarbide target material (2500 °C). The alpha-spectrum of the species evaporated at 2400 °C from the UC target and deposited on a cooled tantalum collector is shown in Fig. 11.
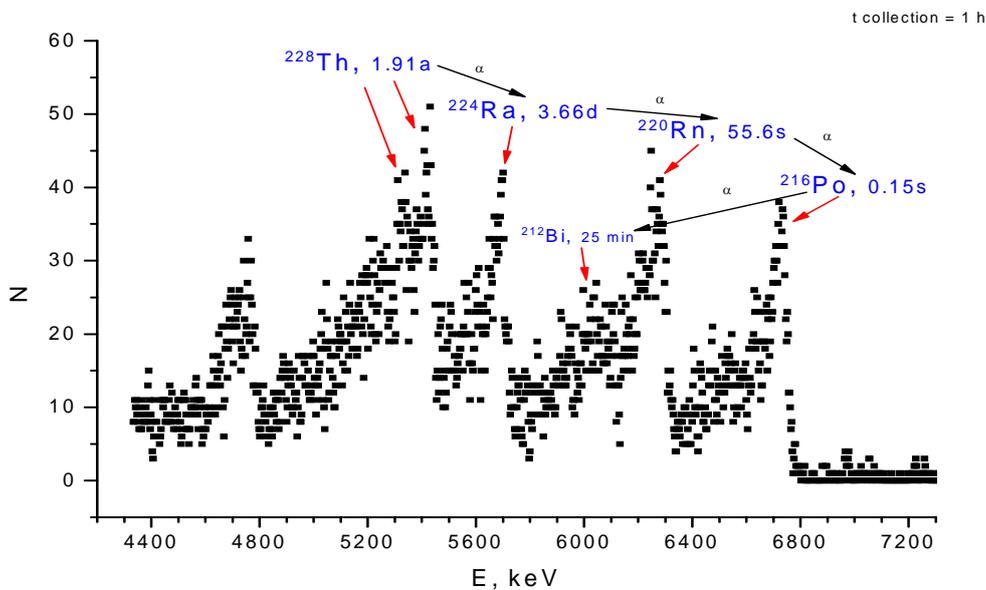
Fig. 11. Alpha-spectrum of species evaporated at 2400 °C from the UC target and deposited on a cooled tantalum collector

353

As the irradiated target was cooled down during a rather long period, we detected the alpha particles emitted only by the long-lived ^{228}Th ($T_{1/2}$ = 1.9 y). In Fig. 11, we can see the chain of alpha lines after the decay of the extracted ^{228}Th:

$$^{228}\text{Th}(T_{1/2} = 1.9 \text{ y}) \rightarrow {}^{224}\text{Ra}(T_{1/2} = 3.66 \text{ d}) \rightarrow {}^{220}\text{Rn}(T_{1/2} = 56 \text{ s}) \rightarrow {}^{216}\text{Po}(T_{1/2} = 145 \text{ ms}) \rightarrow$$

$$\rightarrow {}^{212}\text{Pb}(T_{1/2} = 10.6 \text{ h}) \rightarrow {}^{212}\text{Bi} (T_{1/2} = 25 \text{ min}) \rightarrow {}^{208}\text{Tl}(T_{1/2} = 3 \text{ min}) \rightarrow {}^{208}\text{Pb}(\text{stable}). \quad (2)$$
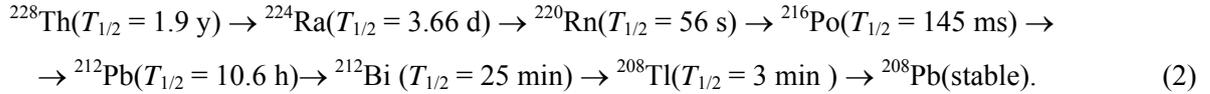
The experiment on ^{224}Ra production demonstrated the principal possibility to obtain alpha emitting radium radionuclides from high density UC targets. There is also a possibility to increase the yields of Ra isotopes by more than an order of magnitude with a ThC target instead of the UC target. The technology of ThC targets has already been developed. Next year, we plan to test this target material for production of radium and other alpha emitting isotopes for medicine.

5. Conclusion

This work can be considered as the first stage of developments of targets for production of several radionuclides from a large set of isotopes for nuclear medicine planned to be produced at the RIC-80 facility. In our tests, several kinds of target materials were explored. The tested target materials will be used for manufacturing of real target prototypes for the PNPI radioisotope complex. All these target materials can be also used to construct the mass-separator targets for production of radioisotopic medical beams of high purity at RIC-80. The following stage will be the construction of a target unit prototype with the amount of the target material of 5–10 g for medical radionuclide production at the RIC-80 complex.

References

1. V.N. Panteleev et al., Abstracts of 7th Int. Conf. on Isotopes, 4–8 Sept. 2011, Moscow, p. 35.
2. G. Battistoni et al., Proc. of the Hadronic Shower Simulation Workshop 2006, Fermilab, 6–8 Sept. 2006, Eds. M. Albrow and R. Raja, AIP Conference Proceeding **896**, 31 (2007).
3. A. Fassò et al., CERN-2005-10 (2005), INFN/TC_05/11, SLAC-R-773.
4. V.N. Panteleev et al., Eur. Phys. **150**, 297 (2007).
5. V. Chudakov et al., Absracts ICI7, 4–8 Sept. 2011, Moscow, p. 42.
6. V.N. Panteleev et al., Eur. Phys. A **42**, 495 (2009).

NEW EXPERIMENTAL METHOD FOR INVESTIGATION OF THE NUCLEON POLARIZABILITIES

G.D. Alkhazov, V.P. Chizhov, E.M. Maev, E.M. Orischin, G.E. Petrov, V.V. Sarantsev, Yu.V. Smirenin

1. Introduction

The electric α and magnetic β polarizabilities are basic structure constants of the nucleon, which characterize the response of the internal nucleon structure to the action of external electric and magnetic fields. The knowledge of α and β provides a stringent test of models describing the quark-meson structure of the nucleon, *e.g.*, in Chiral Perturbation Theory [1]. These polarizabilities are found by measuring Compton scattering cross-sections as a function of the photon energy and scattering angle and by a best fit using a theoretical description with the quantities of interest as open parameters. Experiments focus on photon energies below the pion mass because at these energies the Compton scattering cross-sections can be related model-independently to the polarizabilities through a Low Energy Theorem [2], which takes into account the proton structure in lowest order and shows that the scattering amplitude of Compton scattering off a system with spin ½ can be expanded in powers of E_γ.

Recent experiments on Compton scattering to measure the polarizability of the proton and the deuteron were mostly performed using quasi-monoenergetic photons from bremsstrahlung tagging (see review of Shumacher [3]). The photons were scattered on liquid hydrogen or deuterium, and the scattered photons were detected under one or several scattering angles with NaI or BaF_2 spectrometers. These experiments provided the four-vectors p_i and the numbers of the incoming and scattered photons. A disadvantage of this method is a limited photon flux a tagger system can provide. To increase the luminosity, thick liquid targets were used.

In contrast to the above experiments, in the method proposed in [4] and developed at the Superconducting Darmstadt Electron Accelerator S-DALINAC, bremsstrahlung photons produced by an electron beam are used, and not only the angle and energy of the scattered photons but also the angle and energy of the recoiling protons (deuterons) are measured. This approach (sketched in Fig. 1) increases the luminosity and lowers the background considerably, especially below 50 MeV.
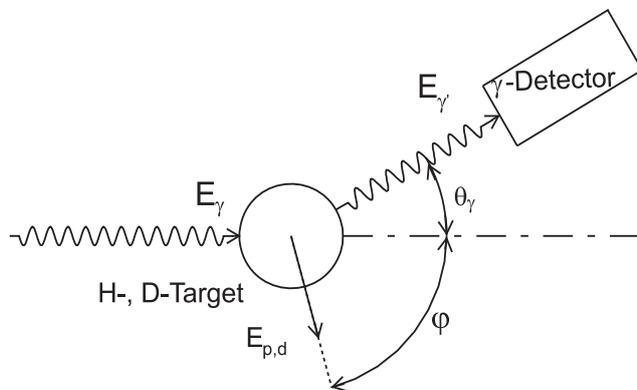

Fig. 1. Experimental method (schematic). A photon beam with a full bremsstrahlung spectrum is scattered from a gaseous hydrogen/deuterium target inside a high pressure ionization chamber, the energy of the scattered photons is determined in a γ-detector under a certain angle. By detecting the scattered bremsstrahlung photon in coincidence with the recoiling proton (deuteron) in the ionization chamber the incoming photon energy is determined

In this report, we describe the new method and a new experimental set-up for measuring the nucleon polarizabilities, and the performed test experiments. The photons scattered off protons in the ionization chambers are detected under two angles, 90° and 130°, by means of 10×14 in^2 NaI(Tl) detectors. The energies of the scattered photons are measured with the NaI(Tl) detectors, while the energies of the scattered recoil protons are measured with the ionization chambers (ICs), which serve simultaneously as targets and detectors.

2. Bremsstrahlung photon facility

A high-energy bremsstrahlung photon facility was built at the S-DALINAC [5]. The aim was to generate a high-intensity, nearly background-free photon beam. In this facility, a fully controlled electron beam is transformed into a photon beam by passing through a 0.3 mm thick (corresponding to 0.1 radiation lengths) bremsstrahlung-radiator made of gold. After the passage through two lead collimation systems into a 3 m concrete wall, the photon beam enters the experimental hall, where the Compton scattering set-up is installed. The position and intensity of the photon beam is measured downstream from the experiment by means of two special ionization chambers placed inside a hole in a concrete wall directly in front of the γ-beam stop for background minimization. The first chamber has segmented anode and cathode plates and allows an online determination of the photon beam position. In future experiments, the position of the electron beam on the radiator target, and therefore the position of the photon beam will be steered with the help of the output signals of this detector. The second ionization chamber is the so called Gaussian quantameter [6]. It allows to measure the γ integrated beam power in a wide energy range from 10 MeV up to several GeV.
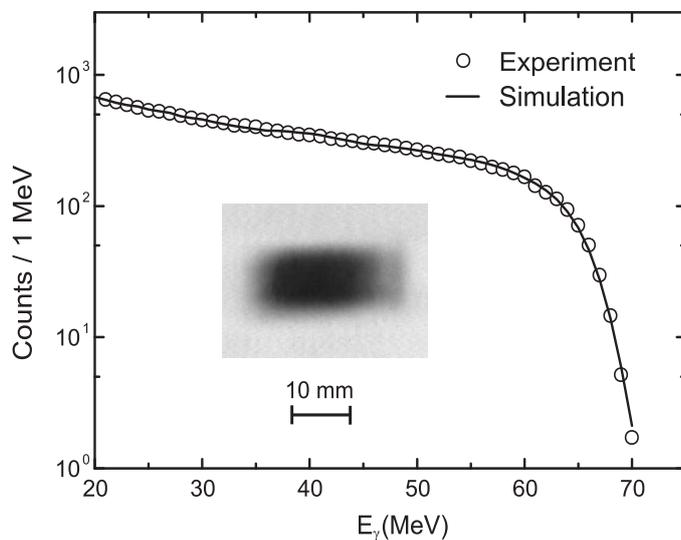
Fig. 2. Bremsstrahlung spectra and a part of a colour inverted Polaroid picture of the collimated bremsstrahlung beam approximately 3 m behind the bremsstrahlung target: Areas with high beam intensity are dark, with low intensity are grey. Circles correspond to the measured bremsstrahlung spectrum. The curve shows a folded simulation spectrum

In order to determine the absolute cross-sections for the Compton scattering off the proton (deuteron) with the reported technique, it is essential to know not only the integral intensity of the photon beam measured with the above-mentioned quantameter, but also the shape of the energy spectrum of the beam. The shape of this spectrum is determined with two additional 10×10 in^2 NaI-spectrometers, which detect Compton scattered photons from the atomic electrons in the exit beryllium window of the ionization chambers. They are placed approximately 10 m downstream from this window under angles of 1.89° and 2.42°, respectively. Photons Compton scattered from electrons under these angles have the same energies as photons Compton scattered off the proton in the ionization chambers at 90° and 130°. The 10×10 in^2 spectrometers are equipped with the same active and passive shielding as the main γ-spectrometers. With the knowledge of the response functions of the NaI(Tl) crystals it is possible to evaluate the intensity as well as the shape of the energy spectrum of the incoming bremsstrahlung beam. Figure 2 shows the energy spectrum of the bremsstrahlung beam measured with the above-mentioned γ-spectrometer in comparison with the results of GEANT4 calculations. Excellent agreement is observed. A colour-inverted Polaroid picture of the collimated γ-beam cross-section obtained 3 m behind the bremsstrahlung target is also shown as insert in this figure. The beam spot size at this position corresponds to a size of 20×10 mm^2 inside the ICs.

3. γ-ray spectrometers

All NaI(Tl) photon spectrometers for detecting the scattered photons are items on loan from the Institute of Nuclear Physics of the Johannes Gutenberg-Universität, Mainz. Those used to detect the photons scattered from protons (deuterons) are 10×14 in^2 in size. Compton scattered photons from the ionization chambers enter these γ-spectrometers through collimation systems, which determine a solid angle of about 10 msr. With this collimator system only the inner part of the γ-detectors is hit, which reduces the low-energy tails in the response functions. An energy calibration was achieved up to $E_\gamma = 4.44$ MeV with the help of standard γ-sources. At higher energies, the energy calibration was performed by using an electron beam with the known energy, and detecting electrons scattered from an aluminum target replacing the hydrogen ionization chamber. According to GEANT4 simulations, the response functions of the detectors for photons and electrons are practically identical. An extrapolation of the energy calibration parameters to the low-energy region shows good agreement with the results of the γ-source measurements. Since these detectors work as trigger detectors and the dead time of the ionization chamber is rather long (about 4 μs), it is essential to minimize their background counting rate. Therefore, the NaI(Tl) crystals are well shielded.

4. High pressure ionization chambers

The detector of recoil protons (deuterons) consists of two ionization chambers combined in one volume. The incident photons scattered on the filling gas of the first (second) chamber are detected under the angle of 90° (130°). Both chambers have a cathode, a grid and an anode divided in strips (Fig. 3).
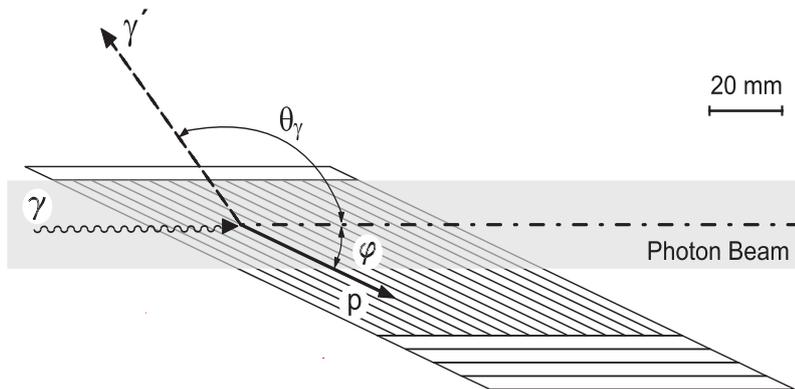

Fig. 3. Top view on a multi-strip anode: the 2 cm broad photon beam enters the volume of the IC from the left side. In the case a photon is scattered under the angle θ = 130°, the scattered proton gets a momentum along an anode strip (at φ = 22°)

The body of the chamber is made of stainless steel with a wall thickness of 14 mm. The photon beam enters (leaves) the chambers through 6 mm (7 mm) beryllium windows. This material was chosen in order to minimize the absorption of photons and production of e$^+$e$^-$-pairs. The Compton scattered photons on hydrogen at these selected angles (θ$_\gamma$ = 90°± 4° and θ$_\gamma$ = 130°± 3°) leave the IC's through 9 mm beryllium windows to the γ-spectrometers. The ICs operate in the electron collection mode, *i.e.* the signals result from the electrons collected after ionization produced by protons. The applied high voltages are –40 kV on the cathode and –3.5 kV on the grid, the anode being at zero potential. The electron drift times are 3.5 and 0.12 μs for the cathode-grid and grid-anode distances, respectively. To select the recoiling proton, a special geometry of the IC anode is used. It is designed to detect tracks of recoiling protons in a background of tracks of Compton scattered electrons and secondary electron-positron pairs. The anode of the IC consists of several strips aligned along the direction of the recoil protons. In particular, in the case of Compton scattering under θ = 130°, the proton recoil angle φ is 22°. Along its path, the proton ionizes hydrogen molecules. As schematically shown in Fig. 4a, ionization electrons drift towards the anode and are collected there on one or two anode strips. When Compton scattered electrons and electron-positron pairs are formed, they have angles different from that of the recoil protons. The charges released by them are collected by several strips and produce only small signals on a single strip. In Fig. 4b, different simulated proton pulse forms are shown. At an azimuthal angle 0° (the proton track is parallel to the anode), the pulse lengths have a

minimal value and are equal for all energies. For protons with higher energies and at larger azimuthal angles, the pulse shape becomes wider and asymmetric.
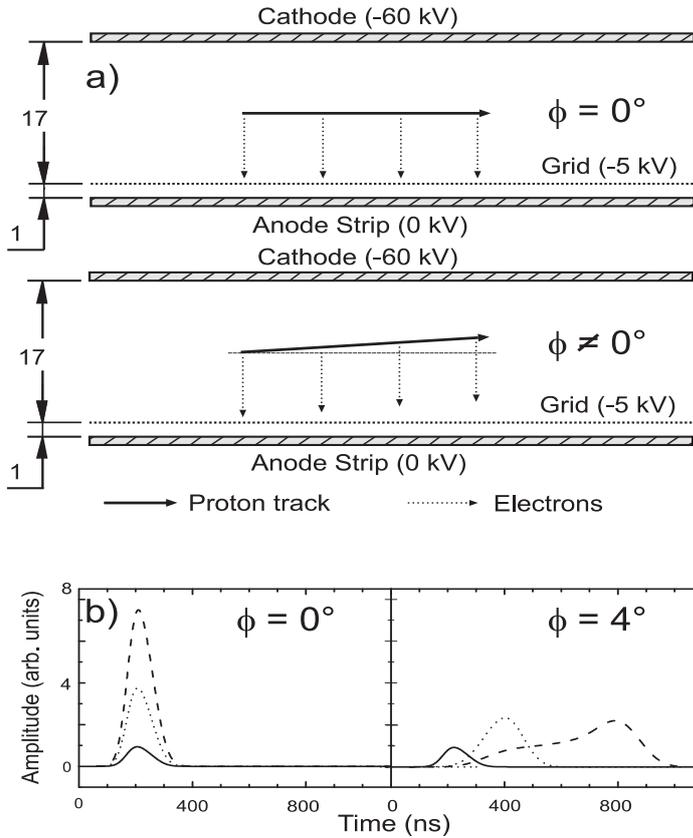

Fig. 4. a – side view of the chamber electrodes. The upper part shows a track of a proton, parallel to the anode. The lower part demonstrates a track of a proton under a finite angle. Dimensions are in mm; b – simulated pulse form for different azimuthal angles and for different proton energies: 1 MeV (solid line), 4 MeV (dotted line) and 8 MeV (dashed line)

Due to high hydrogen pressure in the ICs (75 bar), the effect of recombination of the electrons and positive ions formed by an ionizing particle becomes significant. The effect of recombination was studied for α-particles with a ^{237}Pu source ($E_\alpha = 5.15$ MeV) mounted on the IC cathodes. It was found to be rather large, reducing the registered signals by about 30 %. The effect of recombination in case of ionizing protons is expected to be noticeably smaller. According to [7], the collected charge produced by protons with energies $E_\mathrm{p} \geq 0.5$ MeV in hydrogen at the conditions of our experiment can be estimated by the following empirical formula: $Q = e K (E_\mathrm{p} - E')/W$, where $E' = 0.15$ MeV, $K = 0.9$, e is the electron charge, and $W = 36.3$ eV is the energy for electron-ion pair production in hydrogen. The proton recoil energy is thus

$$E_\mathrm{p} = E' + QW/eK. \tag{1}$$

Another process that might cause a reduction of the registered signals is the attachment of electrons to electronegative impurities (such as O_2 and H_2O) in the working gas of the chambers. To reduce the amount of gas impurities, the chambers were heat trained under vacuum pumping. The hydrogen used for experiments contained less than 1 ppm impurities. Signals from a ^{237}Pu α-source were used for checking the gas quality. During the test experiments, the position of the energy peak of the 5.15 MeV α-particles decreased by ~ 5 % per week, indicating slow evaporation of contaminants from the chamber walls. As simulations have shown, a noticeable amount of electrons (on the level of 0.1 %) appears in the photon beam in the active regions of the ionization chambers due to interaction of photons with the working gas of the chambers. To exclude registration of scattered electrons in the γ-ray spectrometers, anticoincidence scintillation counters, the so-called veto detectors, were placed in front of the NaI detectors.

5. Electronics

The electronics used in the data acquisition consisted mostly of standard NIM, CAMAC and VME components. The signals on the anodes of the ICs were registered by special low-noise preamplifiers, amplifier-discriminators and 14-bit 100 MHz Flash ADCs (FADCs). The FADCs digitize the analog signal in 10 ns steps continuously and hold the values for 4.5 µs in a ring buffer memory. This is necessary, since the signals from ICs are delayed relative to the trigger pulse of the NaI(Tl) detectors by the drift time of electrons produced by recoil protons in the Compton scattering event. The trigger signals define a time window of 4.5 µs, in which the proton pulse is expected to take place. The current on the IC anodes is always recorded within this window by the FADCs when a trigger signal is generated. Figure 5 shows an example of a recoil proton signal, registered by a FADC, in comparison with a GEANT4 simulation. The results of the measurement and the simulation are in good agreement.
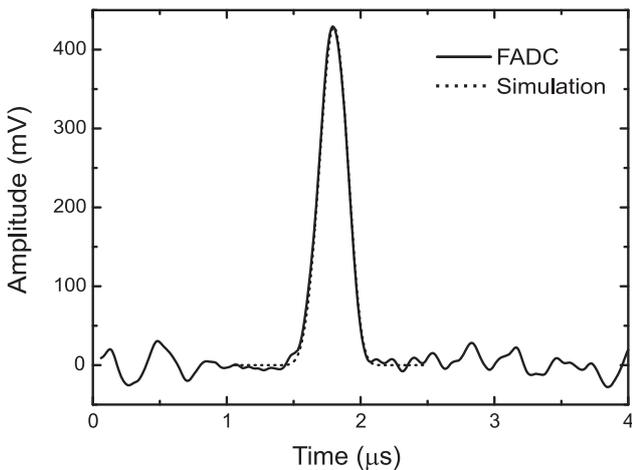
Fig. 5. Example of a signal in the IC from a 4 MeV recoil proton, registered by a FADC, compared to a GEANT4 simulation

The channels of the FADC have to be read out for each IC, which takes quite a long time (about several µs) making it necessary to minimize the trigger rate. In order to improve the signal-to-noise ratio, the registered signals can be treated off-line with digital filters. A preliminary energy calibration of the amplifier channels was performed by inserting calibrated charges through a small capacitance to the anodes of the ICs. The NaI(Tl) detectors, which act as trigger detectors, are operated in anticoincidence mode with the surrounding plastic detectors. The signal is split in two: one signal starts the whole readout from the trigger module, the second signal is delayed by 4.5 µs and stops the recording of the FADCs, which are then read out. This trigger unit also starts the readout of the ADCs, which digitize the NaI(Tl) energy pulses. In addition to the energy signals from the main γ-detectors (for registering γp-scattering) and the pulses on the anode strips of the ICs, data of other detectors like the quantameter, the position detectors, the Faraday cup and the signals from the γ-detectors for the beam monitoring are continuously read out and written onto tape or disk using the MBS data acquisition system.

6. Test experiments

Test experiments were performed at the S-DALINAC using bremsstrahlung photon beams with endpoint energies of 60 and 79.3 MeV. Electron beam currents ranged from 1 to 5 µA. The ICs were filled with hydrogen gas of high purity (99.9999 %) at a pressure of 75 bar. The gas pressure was measured with a precision of about 0.5 %. In these test experiments about 5000 Compton scattered events in total were collected in coincidence with recoil protons. Figure 6 shows a typical drift-time distribution of signals which appeared at the IC anodes. This distribution reflects the γp-interaction points in the vertical direction. The width of this distribution corresponds to a vertical photon beam size of about 1 cm. It is seen that the position of the photon beam was not in the middle of the gap between the IC grid and the cathode, but closer to the grid. The number of events in the drift time interval from 2.5 to 3.5 µs is small demonstrating that

359

the coincidence between the signals from the γ-spectrometers and the ionization chambers suppresses the background very efficiently. At the same time, one can see some events in the drift time interval of 0–0.5 μs and 2–2.5 μs. Presumably, these events appear due to some halo of the photon beam.
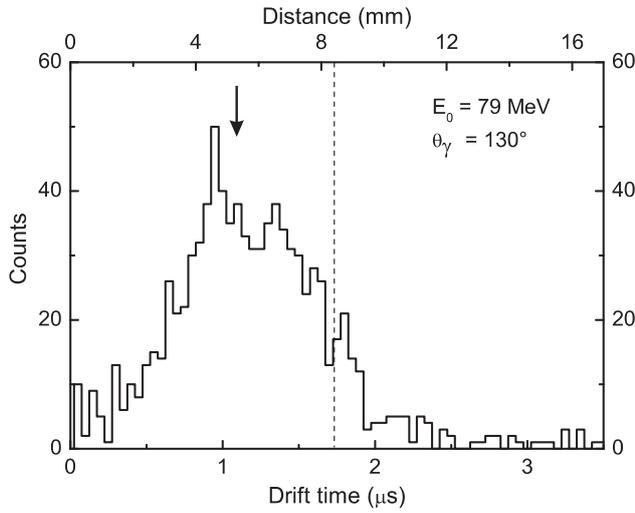

Fig. 6. Drift-time distribution of proton signals in an IC. The dashed line denotes the centre of the active volume between electrodes. The actual location of the photon beam is indicated by the arrow

The measured energy correlation between the scattered photons and recoiled protons is shown in Fig. 7 for the data taken at $E_0 = 60$ MeV, $\theta_\gamma = 130°$ and energies $E_\gamma > 20$ MeV, $E_p > 1$ MeV. The experimental data are in good agreement with the expected kinematical relation. This figure also demonstrates that the background is rather small. Events on the left side of the (E_γ, E_p) correlation curve are partly due to tails of the γ-response function and partly due to background, which may be reduced in the future by building additional shielding for the γ-spectrometers.

The cross sections obtained in the experiments at $E_0 = 60$ and 79.3 MeV are shown in Fig. 8. The overall normalization of the (γ, p) cross sections measured as a function of the photon energy was performed with the help of the theoretical curve with $\alpha = 11.8$, $\beta = 2$ (dashed line). The resulting cross sections are in good agreement with a previous measurement [8] at comparable photon energies.
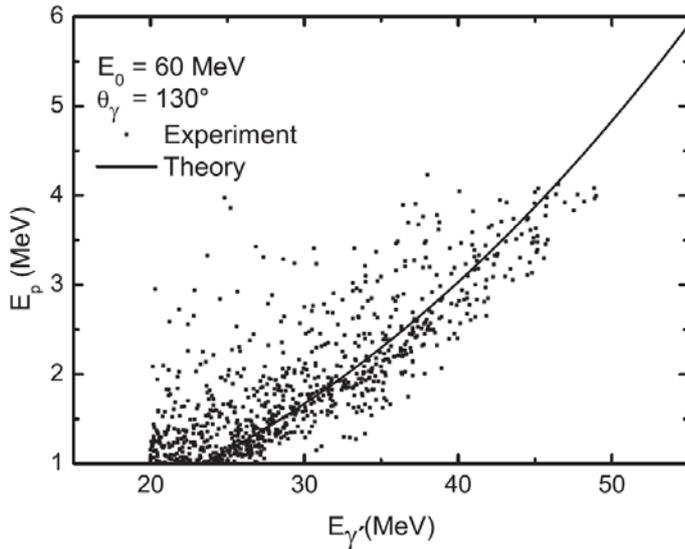

Fig. 7. Measured energy correlation of the scattered photons ($E_\gamma > 20$ MeV) and recoil protons ($E_p > 1$ MeV) in comparison with the expected kinematic relation for E_γ and E_p (solid curve) for the data taken at $E_0 = 60$ MeV and $\theta = 130°$. The proton recoil energies are determined from the measured charges, collected on the IC anodes, with the help of Eq. **(1)**

Of course, the low statistics collected in the test experiment is not sufficient to extract meaningful results on the proton polarizabilities. From those measured values and the range of results from theoretical calculations [2] it has been estimated that in order to determine the values of α and β for the proton with a precision of $\Delta\alpha = 0.3$ and $\Delta\beta = 0.4$ with this technique it is necessary to perform measurements at a 100 MeV

electron beam (to increase the photon flux per incident electron) with an integrated beam current of 2.5×10^4 μAxh. The proposed new experimental method and the results of two test runs have shown that future high-statistics experiments to determine α and β are indeed feasible.
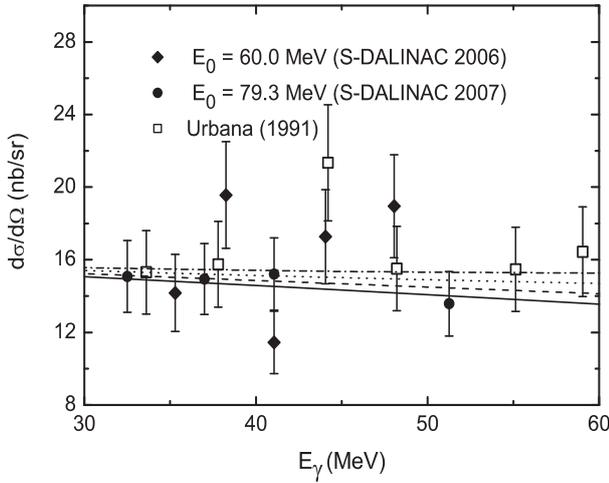

Fig. 8. Differential cross sections for Compton scattering on the proton obtained in the experiments at the S-DALINAC at $E_0 = 60$ MeV (full diamonds) and $E_0 = 79.3$ MeV (full circles) at an angle $\theta = 130°$. Data from [8] in the same energy region and at an angle of 135° are given as squares. The lines correspond to calculations for different values of α and β: $\alpha = 13.8$, $\beta = 0$ (solid line), $\alpha = 11.8$, $\beta = 2$ (dashed line), $\alpha = 9.8$, $\beta = 4$ (dotted line), $\alpha = 7.8$, $\beta = 6$ (dashed-dotted line). The error bars include statistical contributions only. The data from the S-DALINAC are normalized with the theoretical curve shown as dashed line

7. Conclusion

A new method for measurements of the electric and magnetic polarizabilities (α and β) of the proton and deuteron has been proposed and tested. The new approach for determination of α and β is based on Compton scattering of untagged bremsstrahlung photons and registration of the recoil protons (deuterons) with special high-pressure hydrogen ionization chambers, which serve as targets and detectors. The scattered photons are registered with NaI(Tl) spectrometers. Test experiments have shown that the whole set-up functions in the expected way. The new experimental set-up for measuring the electric and magnetic nucleon polarizabilities is described in more detail in [5].

This work was performed in collaboration with O. Yevetska, S. Watzlavik, P. von Neumann-Cosel, J.-M. Porté, A. Richter, and G. Schrieder (Institut für Kernphysik, Technical University Darmstadt, Germany).

References

1. V. Bernard, N. Kaiser, U.-G. Meissner, Int. J. Mod. Phys. E **4**, 193 (1995).
2. A.I. L'vov, V.A. Petrun'kin, M. Schumacher, Phys. Rev. C **55**, 359 (1997).
3. M. Schumacher, Prog. Part. Nucl. Phys. **55**, 567 (2005).
4. D.V. Balin, M.J. Borkowski, V.P. Chizhov, G.A. Kolomensky, E.M. Maev, D.M. Seliverstov, G.G. Semenchuk, Yu.V. Smirenin, A.A. Vasiliev, A.A. Vorobyov, N.Yu. Zaitsev, Preprint PNPI-**2104**, Gatchina (1996).
5. O. Yevetska *et al.*, Nucl. Instr. and Meth. A **618**, 160 (2010).
6. A.P. Komar, S.P. Kruglov, I.V. Lopatin, Nucl. Instr. Meth. **82**, 125 (1970).
7. V.A. Volchenkov, E.M. Maev, V.P. Maleev, G.A. Ryabov, G.G. Semenchuk, Preprint PNPI-**1368**, Gatchina (1988).
8. F.J. Federspiel, R.A. Eisenstein, M.A. Lucas, B.E. MacGibbon, K. Mellendorf, A.M. Nathan, A. O'Neill, D.P. Wells, Phys. Rev. Lett. **67**, 1511 (1991).

GAS-FILLED POSITION-SENSITIVE THERMAL NEUTRON DETECTOR

V.A. Andreev, G.A. Ganzha, E.A. Ivanov, D.S. Ilyin, L.M. Kochenda, S.N. Kovalenko, M.R. Kolkhidashvili, A.G. Krivshich, A.V. Nadtochy, A.I. Okorokov, V.V. Runov, G.D. Shabanov, V.A. Solovei

1. Introduction

Multi-wire proportional chambers filled with the ^{3}He + CF$_4$ gas mixture with a delay line readout are widely used for thermal neutron detection, especially in Small-Angle Neutron Scattering (SANS) instruments [1–3]. The purpose of the discussed work was to find a set of strongly interrelated detector design parameters with the aim to improve the detector performance. After careful consideration of important detector parameters, such as the space resolution, the efficiency and differential and integral nonlinearity, a satisfactory solution was found. In order to guarantee a reliable and optimal operation of the neutron detector, a wide range of scientific and technological investigations was carried out to:

- improve and optimize the detector mechanical characteristics, simulations of the detector pressure behavior up to 10 bar were performed;
- minimize the detector outgassing, a new technology for fabrication of the detector electrodes was successfully developed. It has opened a way to improve the gas purity by a few orders of magnitude;
- minimize the gas leakage to a level smaller than 0.03 % per day, the detector gas sealing technology was improved.

This paper describes general approaches and technological solutions that have allowed us to develop thermal neutron detectors for the SANS diffractometers "Vector" and "Membrana-2" at the VVR-M reactor of PNPI. The required parameters of the detector are listed in Table 1.

Table 1

The required characteristics of 2D-detectors

Characteristic	Diffractometer	
	"Membrana-2"	"Vector"
Neutron wave length, Å	3	9
Entrance window $X \times Y$, mm^2	200×200	300×300
Neutron efficiency, %	≥ 70	≥ 70
Position resolution $X \times Y$, mm^2	2×2	2×2
Counting capability, kHz	≤ 100	≤ 100
Intrinsic noise, Hz	< 0.5	< 0.5
Life time, years	≥ 5	≥ 5

2. Detector design principles

2.1. Thermal neutron detection

Neutrons are detected by their capture in the ^{3}He gas according to the nuclear reaction

$$^3\text{He} + n \rightarrow p + {}^3\text{H} + 764 \text{ keV}. \tag{1}$$

Achieving the highest detector efficiency was one of the first problems to be solved by detector construction. From this point of view, ^{3}He is very convenient gas to use because it has a large cross-section for capture of thermal neutrons, 26500 b for 9 Å neutrons.

2.2. Detector construction

Several model calculations (ANSYS 8.1) of different versions of the mechanical design of the neutron detector have been carried out using the finite-element method. The most successful design was chosen from the point of view of minimal deformations of the entrance window under internal pressure. The chamber

prototype was constructed from the aluminum alloy AMg5. This alloy has the most suitable combination of the mechanical strength and good neutron transmission properties. Moreover, as it was measured, this material has a minimal cross section for neutron small-angle scattering compared to other investigated materials for detector construction.

To ensure uniformity of the detector efficiency across the detector entrance window, it was necessary to avoid deformations of the entrance window under gas pressure. After improvements of the detector design it became possible to minimize deformations of the entrance window (of 10 mm thickness) to 0.2 mm.
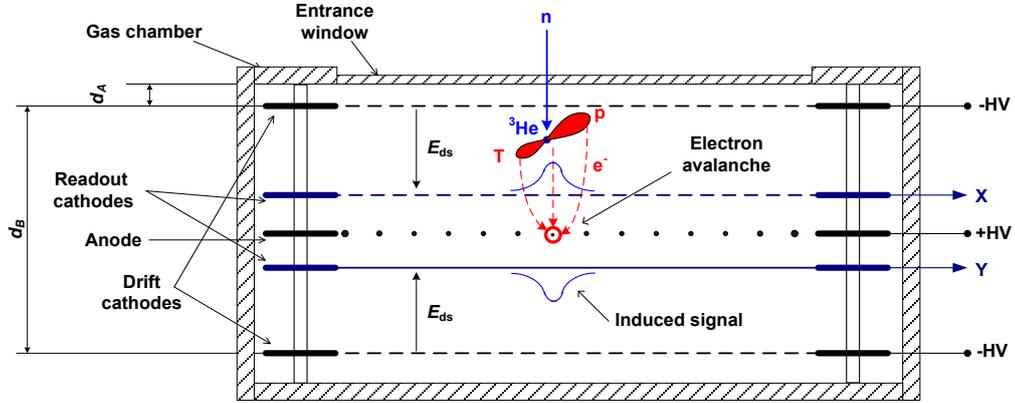
Fig. 1. Schematic diagram of the 2D-detector: E_{dr} – direction of the electric field in the drift gaps, d_A = 1.5 mm – the gap between the entrance window and the plane delimiting the detector sensitive volume (detector insensitive zone), d_B = 32 mm – the thickness of the sensitive volume, +HV and –HV – the potentials applied to the anode and the drift electrodes, respectively

The detector design (Fig. 1) was based on a Multi-Wire Proportional Chamber (MWPC). It has a conventional design with two orthogonal cathode grids symmetrically located about the central anode grid. The anode consists of gold plated tungsten wires with the diameter 25 μm, the wire spacing being S = 4 mm. The anode-cathode distance is L_c = 4 mm. The cathode wires diameter is 55 μm, the wire spacing is 1 mm. Every three wires are connected together into one strip, which is connected to a delay line with an impedance of 100 Ohm with a specific delay of 6 ns per strip. So, the strip pitch is w = 3 mm. In order to increase the detector efficiency, there were two 12 mm absorption/drift regions, which were adjacent to both cathodes of the MWPC. In this way, the detector active thickness was 32 mm.

In order to achieve the best physical parameters of the detector, it was necessary to optimize the anode signal transmission to cathode strips. For this purpose, some other geometrical parameters of the MWPC were selected close to the optimum condition: $w / L_c \approx 0.8$, which provided both high amplitude of signals induced on the cathode, Q_c, and a minimal level of the differential nonlinearity.

Because of a high cost of the ^{3}He gas, much attention was paid to the problem of gas leakage from the chamber volume. At the stage of the detector design, significant efforts were undertaken to decrease the gas leakage. To evaluate the final value of this parameter, the temperature and pressure of the gas mixture were measured in the chamber during a period of about 400 days. The time dependence of the relative density of the gas mixture was calculated. It was shown that the leakage rate was about 0.03 % per day.

2.3. Neutron efficiency

The efficiency of a neutron detector is determined by a set of factors such as the partial pressure of ^{3}He, the construction and material of the gas chamber, the geometry of the MWPC, and its location in the chamber. Special attention was paid to inevitable losses of neutrons both in the entrance window and in the intermediate gas gap between the entrance window and the first drift cathode (Fig. 1). The efficiency of the detector was calculated as

$$\varepsilon = \exp(-\mu_{Al}d_{Al}) \times \exp(-\mu_A d_A) \times [1 - \exp(-\mu_B d_B)], \tag{2}$$

where $\mu = n \times \sigma$; n is the gas atomic concentration, σ is the neutron capture cross-section, d_{Al} is the entrance window thickness, d_A is the gap thickness between the entrance window and the upper drift cathode, d_B is the thickness of the detector active area.
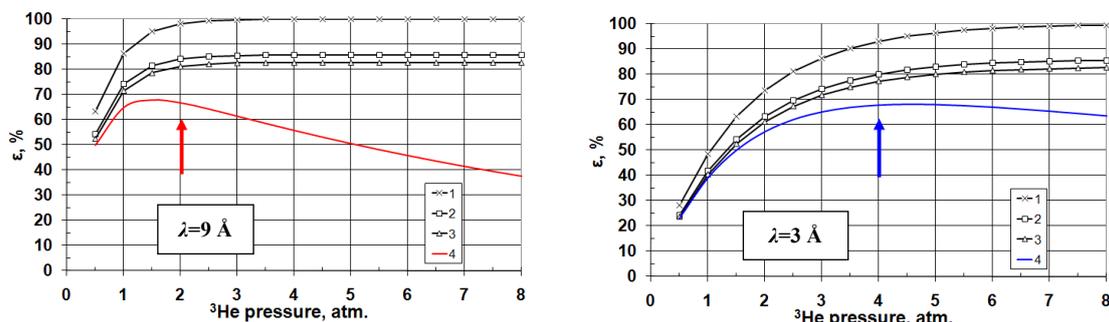

Fig. 2. Calculated efficiencies of the neutron detectors for the spectrometers "Vector" (left) and "Membrana-2" (right). (1) – neutron conversion efficiency without attenuation factors; (2) – the same as (1) with neutron losses in the entrance window; (3) – the same as (2) with losses in the upper drift electrode; (4) – the same as (3) with losses in the gap between the entrance window and the sensitive volume. This is the final detector efficiency

To achieve the required efficiency $\varepsilon \geq 70\,\%$ (Table 1), the gap between the entrance window and the upper drift cathode was reduced to $d_A = 1.5$ mm. The drift electrode was made of thin (2.5 mm) plane of quartz glass with metallic coating 15 μm thick.

The detectors were designed for different wavelengths of neutrons. The 2D-detector for the diffractometer "Vector" ($< \lambda > = 9$ Å) has achieved efficiency $\varepsilon \approx 70\,\%$ at the partial ^{3}He pressure $P(^3\text{He}) = 2$ bar, and the 2D-detector for the diffractometer "Membrana-2" ($< \lambda > = 3$ Å) has achieved the same efficiency only at $P(^3\text{He}) = 4$ bar, Fig. 2. To keep the detector efficiency stable for a long time and to make it insensitive to possible gas leakage from the gas volume, the working pressure of the ^{3}He gas was chosen on the plateau, indicated by arrows in Fig. 2.

2.4. Design of the electrodes

The neutron detectors are closed in a sealed gas-filled volume. To guarantee long-term detector performance and to prevent degradation of the energy resolution, it is necessary to maintain a high level of the gas mixture purity. In other words, the detector must be fabricated from the materials which can be pumped to high vacuum and heated up to at least 100 °C. To minimize outgassing of the detector inner parts, we have developed a new technology of fabrication of the detector electrodes. Now, all electrodes are fabricated from quarts glass and are subject to high vacuum pumping and heating up to 130 °C. The properties of the deposited printed circuits are staying constant even after heating of the frame up to 150 °C. The wire soldering is done by a solder with the melting point at 280 °C. This technology has opened a way to improve the gas purity by several orders of magnitude. No glues are used in the detector construction.

The new technology has provided an increased lifetime and stable operation of the detectors since 2007 without refilling the gas.

3. Experimental results

3.1. Detector efficiency

To measure the detector efficiency, a reference proportional counter filled with the ^{3}He gas under 10 bar pressure intended for thermal neutron detection with the efficiency of about 100 % was used. Our detector of neutrons and the proportional counter were irradiated by a collimated neutron beam independently. The ratio of the counting rates demonstrated us that our detector has the efficiency about $\varepsilon = 70\,\%$, which is in good matching with the results of calculations (see section 2.3). The neutron beam flux density was 1.7×10^4 s^{-1}cm^{-2}.

3.2. Differential nonlinearity

The differential nonlinearity is the derivative dx_m/dx of the position calibration curve $x_m = f(x)$, where x_m is the measured neutron position and x is the true position. A measure of the differential nonlinearity is prompted by the flat response of a uniform illumination spectrum. Any nonuniformity of the detector efficiency is also encompassed by this spectrum. Figure 3 shows a uniform illumination spectrum along the anode wires (X-axis) obtained with a wide beam of thermal neutrons. The differential nonlinearity of this measurement is very small and does not exceed $\pm 7\%$. This parameter is very sensitive to boundary discontinuities between the two multi-pin connectors transferring the signals from the cathode strips. There was no indication of discontinuities at the section boundaries.
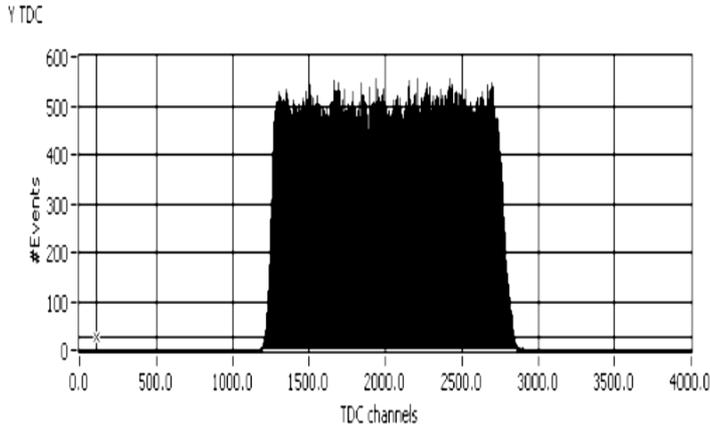
Fig. 3. Uniform illumination spectrum along the fine resolution axis (parallel to the anode wires)

3.3. Position resolution

We point out three more important parameters, which are directly related to the detector position resolution: the ranges of particles produced in the reaction (determining the physical limit of the detector position resolution); the geometrical structure of the MWPC, and the intrinsic resolution of the detector.

3.3.1. The range of primary particles

The physical limit of the detector position resolution is determined by the particle ranges from reaction (1) and their ionization losses. The proton and the triton are emitted in opposite directions from the point of the nuclear reaction, the emission being isotropic. The centroid of the ionization charge is displaced with respect to the point of the nuclear reaction due to different ionization losses of protons and tritons. The loci of the centroids for many neutrons are uniformly distributed on the surface of a sphere. The resulting probability distribution along any axis is rectangular. According to Ref. [1], the spheroid diameter is $D_{sph} = 0.7 \times R_p$, where R_p is the proton range.

The gas ^{3}He has low stopping power, and that is why CF_4 was used as a stopping gas to reduce the particle ranges. It localizes the electron avalanche near the anode wire in the point of its formation, and it has good quenching properties.

The position resolution of the detector is limited to D_{sph}, it is determined by the pressure $P(CF_4)$ of CF_4:

$$D_{sph} = 0.7 \times R_p \approx 2.8 \text{ mm} / P(CF_4) \text{ [bar]}. \tag{3}$$

So, the physical limit for the space resolution will be about 1.4 mm under the CF_4 pressure of 2 bar.

3.3.2. Readout method

The cathode strip Delay Line (DL) readout method was chosen to acquire the signals from the MWPC. It provides a high position precision and high integral counting capability (limited by the DL length, typically $T_{DL} < 1$ µs) with the minimum number of electronic channels – only five.

The induced pulses come from the ends of a DL to a charge-sensitive PreAmplifier (PA), Fig. 4. The zero-crossing method was used to fix the signal arrival time to the PA. The time delay between the arrival of signals to the PAs was determined by the coordinate of the electron avalanche

$$x = \left(1 - \frac{t_2 - t_1}{T_{DL}}\right)\frac{L_{det}}{2}. \tag{4}$$

Here t_1 and t_2 are the times of arrival of signals at the ends of the DL, T_{DL} is the time length of the DL (ns), L_{det} is the geometric length of the cathode sensitive area along the coordinate X.

The structure of the MWPC and the readout method determine the measurement of coordinates. The coordinate spectrum along the X-axis (perpendicular to the anode wires) is discrete. The position resolution along the X coordinate (FWHM$_X$) is determined by the anode pitch S if the condition $D_{sph} < S$ is satisfied. The coordinate spectrum along the Y-axis (parallel to the anode wires) is continuous. The position resolution along the coordinate Y (FWHM$_Y$) does not depend on the anode pitch. It is determined by the value D_{sph} and the intrinsic resolution of the detector (FWHM$_{int}$):

$$\text{FWHM}_Y = \sqrt{D_{sph}^2 + \text{FWHM}_{int}^2}. \tag{5}$$
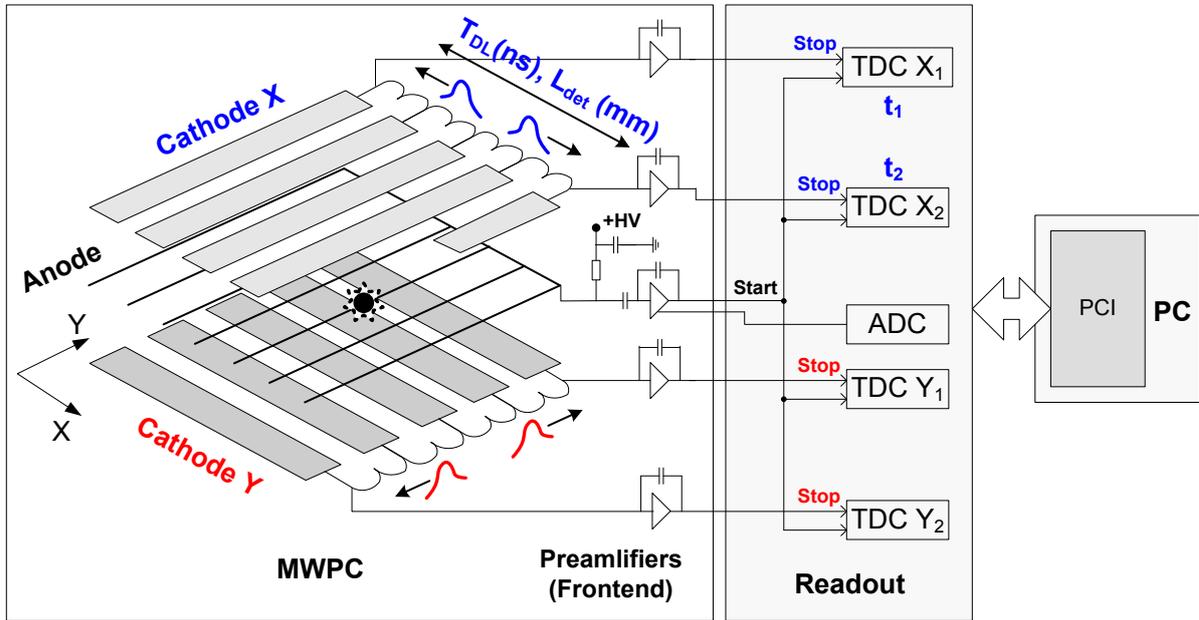
Fig. 4. Scheme of information readout from the MWPC. The cathode strips with a DL ($Z = 100$ Ohm), cathode preamplifiers (PAs with the input impedance $R_{in} = 100$ Ohm), Time-to-Digital Converters (TDCs), Analog-to-Digital Converters (ADCs), and the computer (PC) with a PCI-interface card are shown

The intrinsic resolution of the MWPC is determined by its design, by induced charge amplitudes, by the signal transmission quality of the DL, and by the noise level of the front-end electronics. In practice, the intrinsic position resolution FWHM$_{int}$ is limited by the noise generated in the termination of the DL with the PA:

$$\text{FWHM}_{int} \cong \frac{1}{\theta}\frac{e_n}{ZQ_c}\sqrt{\tau}. \tag{6}$$

Here $\theta = T_{DL}/\tau$ is the "quality" factor of the DL, τ is the dispersion of a signal in the DL, e_n is the noise spectral density (V / Hz$^{1/2}$).

To achieve the best physical parameters of the detectors, it was necessary to reach the required intrinsic resolution at the minimal gas gain. This regime is characterized by a lower level of the high voltage noise of the MWPC, a higher level of the gas gain uniformity and a higher amplitude resolution.

The designs of the DL and preamplifiers were refined in the detector prototype. In order to reach the value $FWHM_{int} \leq 1$ mm, the impedance of the DL was chosen as high as possible, $Z = 100$ Ohm. To minimize the electronic noise, the input impedance of the cathode preamplifiers was chosen the same as the DL impedance $R_{in} = Z$ (the "electronic cooling" mode). In the result, the intrinsic resolution of the detector has reached the value $FWHM_{int}t \leq 1$ mm at the gas gain $M \geq 130$ and $FWHM_{int} = 0.5$ mm at $M = 200$.

3.3.3. Position readout in the direction perpendicular to the anode wires (*Y*-axis)

As one can see from the differential nonlinearity presented in Fig. 3, the uniform illuminated spectrum has a flat response, and no edge effects in this spectrum are observed, which usually manifest themselves as a rise of the local intensity at the spectrum edges. This means that the absolute position error in the *X*-direction is small.

Figure 5 shows the uniform illumination spectrum as seen in the *Y*-direction. One can see good shaped independent peaks with the modulation period of the anode wire spacing. Because the peak positions are determined by the gas avalanches surrounding the anode wires, it allows us to conclude that the integral nonlinearity along the *Y*-direction is less than 0.4 % (this is the measured absolute position error).

Generally speaking, it is possible to state that the absolute position error in both *X*- and *Y*-directions is small and considerably smaller than the space resolution determined by physical reasons.

It is essential to note that the width (FWHM) of these peaks means the real (intrinsic) resolution of the detector, which is affected by the electronic noise, the DL quality, the electric field structure, *etc*. The obtained results are presented in Fig. 6. As one can see, the intrinsic resolution of the detector is 0.6 mm, which is several times better than the physical limit D_{sph}.
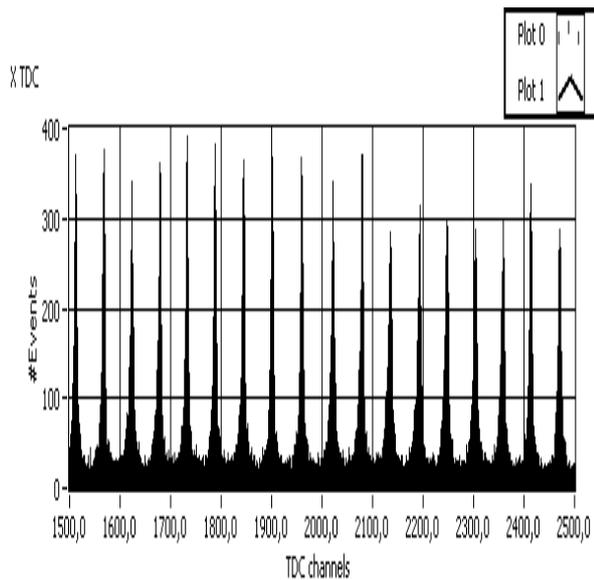

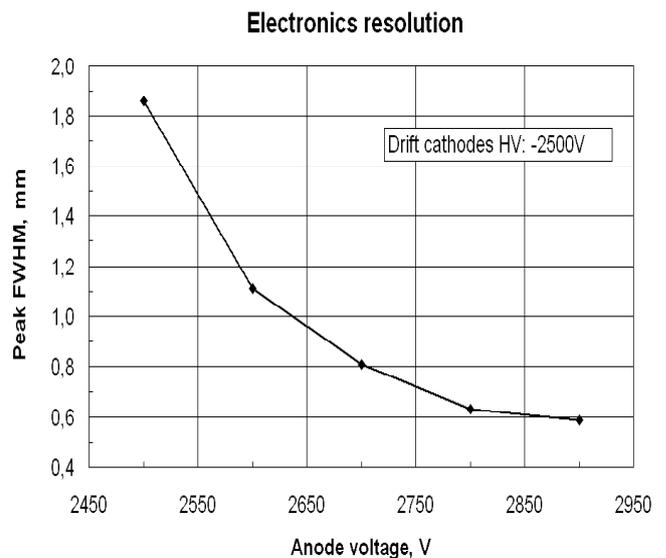**Fig. 5.** Uniform illumination spectrum along the discrete axis (perpendicular to the anode wires)

Fig. 6. Intrinsic resolution of the detector *vs* high voltage

3.3.4. Position resolution in the direction along the anode wires (*X*-axis)

To measure the space resolution, the detector was irradiated by a narrow neutron beam with its width being discretely changed in the range from 4.0 to 0.5 mm by cadmium collimators. A typical view of the obtained spectra is shown in Fig. 7. As one can see from the obtained data in Fig. 8, the detector spatial resolution is about $FWHM = 1.5$ mm.

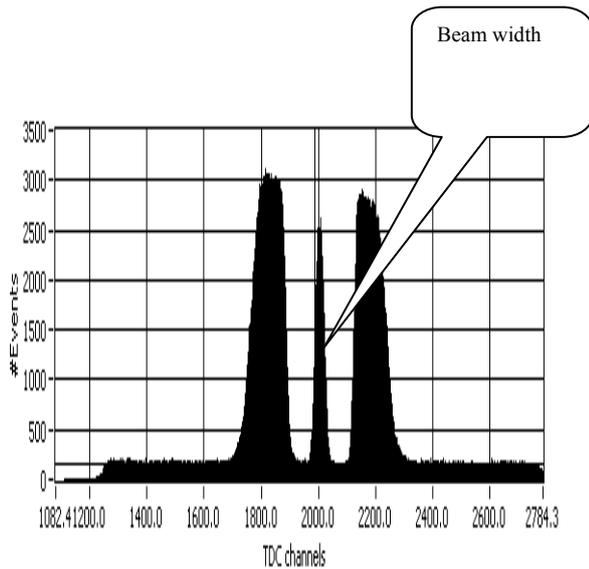This is in good matching with the expected neutron resolution.

Fig. 7. Experimental method of the neutron position response measurement along the fine resolution axis
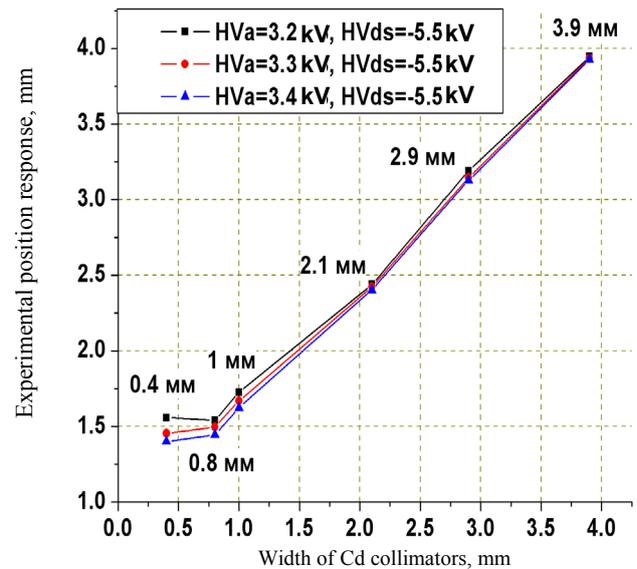

Fig. 8. Results of measurements of the spatial resolution of the detector

3.4. Energy spectra

The shape of the amplitude spectra is an important characteristic of the neutron detector. It is determined by the gas composition and its purity, the gas pressure, the gas gain and its uniformity along the detector window, the applied anode and cathode voltages.

3.4.1. Amplitude spectra of the neutron detectors and the standard neutron counter

The pulse height spectra dependence on the anode high voltage and the electric field in the drift regions was investigated. It was shown that the neutron detector spectra (Fig. 9b) are very similar to those obtained with the reference proportional counter with the gas pressure of 10 bar and look like a "dark body" for thermal neutrons, Fig. 9a.

The energy spectrum has a well-defined peak corresponding to the energy released in reaction (1). There are bumps corresponding to the energies of the proton (573 keV) and the triton (191 keV). Some distinctions are due to the fact that the detectors were filled with different gas mixtures (various concentrations of ^{3}He and CF_4 in the gas mixtures and different pressures) and that the 2D-detector is a multi-wire detector consisting of several hundred of anode wires.
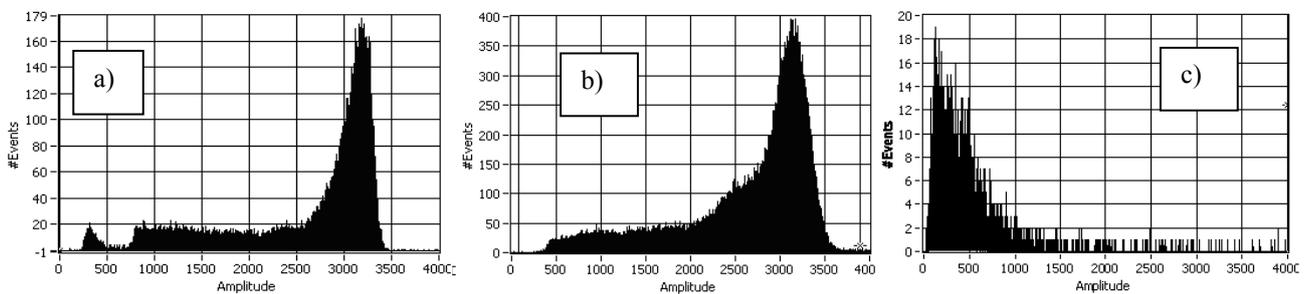

Fig. 9. Amplitude spectra measured with the neutron detectors. a – standard neutron counter SNM-50, high voltage was 2.0 kV; b – neutron detector, anode high voltage is H_A = 2.6 kV, cathode high voltage HV_{DS} = –2.5 kV. The intrinsic noise of the detector was rejected by the PA threshold; c – intrinsic noise of the neutron detector. The PA threshold is about zero

The intrinsic noise and the background spectrum of the neutron detectors are located in the low-amplitude part of the spectrum (Fig. 9c). Therefore, a correct choice of the events discrimination threshold can provide a minimal level of noise, keeping the neutron efficiency value constant. It corresponds approximately to the triton energy E_T =191 keV or ¼ of the peak amplitude of the total energy.

3.4.2. Amplitude spectra and background discrimination

An investigation of γ-sensitivity of the detectors has shown that amplitudes of events caused by registration of γ-rays are rather small. Therefore, if necessary, a rejection of low-amplitude events can provide very low γ-sensitivity of the detectors, $\varepsilon_\gamma \approx 1.8 \times 10^{-8}$ with small reduction of the neutron detection efficiency, < 5 % (Fig. 10). This feature allows to effectively register thermal neutrons in a high background of γ-quanta.
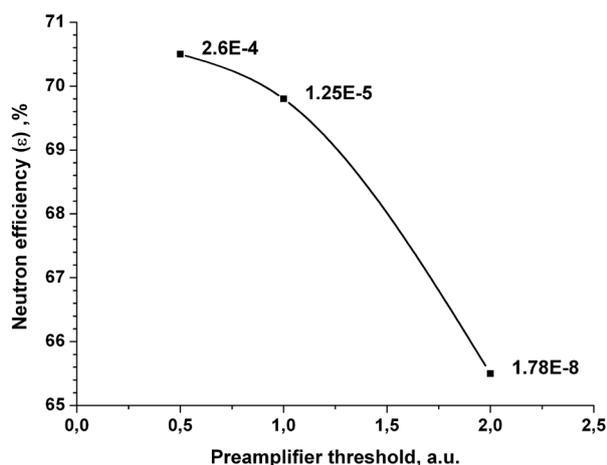
Fig. 10. Neutron- and γ-sensitivity of the detector with the entrance window 200 × 200 mm^2 *vs* the preamplifier threshold. The γ-source ^{137}Cs: A = 80 MBq, E_γ = 0.662 MeV

3.4.3. Gas purity control

Insufficient purity of the working gas dramatically affects the operation of the detector. It leads to violation of the operating parameters and makes impossible to ensure the correct functioning of the detector. Therefore, at the stage of the gas filling of each detector, the amplitude spectra were measured with the proportional counter SNM-50. Typical spectra are shown in Fig. 11.
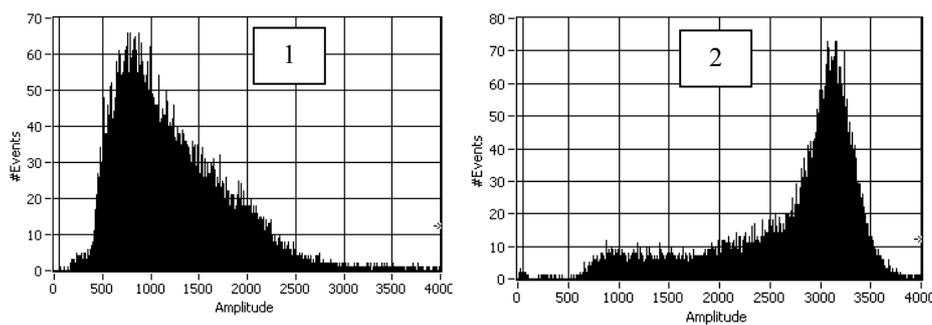

Fig. 11. Amplitude spectra measured by the neutron counter SNM-50 filled with the investigated gas. 1 – before ^{3}He cleaning. Gas mixture: (4 bar ^{3}He + + 100–300 ppm of O_2) + 2 bar CF_4; 2 – after ^{3}He cleaning. Gas mixture: 4 bar ^{3}He + 2 bar CF_4

4. Conclusion

Thermal neutron detectors for the diffractometers "Vector" and "Membrana-2" have been designed, constructed and successfully tested [4]. All required parameters have been achieved, as in Table 2. These detectors were successfully used in neutron diffraction experiments at the reactor VVR-M of PNPI.

Table 2

Working characteristics of the designed detectors

Characteristic	Diffractometer	
	"Membrana-2"	"Vector"
Neutron wave length, Å	3	9
Entrance window, mm	200×200	300×300
Gas mixture (^{3}He + CF$_4$), bar	4 + 2	2 + 2
Gas leakage, %/year	< 7	5
Neutron efficiency, %	70	72
Position resolution (FWHM$_{X, Y}$), mm	1.6×2.0	1.5×2.0
Plateau voltage range, kV	HV$_A$ = + (2.9–3.4) HV$_{DS}$ = – (1.0–6.0)	HV$_A$= + (2.9–3.3) HV$_{DS}$= – (1.0–6.0)
Intrinsic noise, Hz	< 0.2	< 0.3
Maximum counting rate (limited by the readout electronics; 10%-level of miscalculations), kHz	125	125
γ-sensitivity (^{137}Cs)	$< 2 \times 10^{-8}$	$< 2 \times 10^{-8}$

The approaches applied for optimization of the detector parameters have allowed us not only to achieve the required set of the detector characteristics, but also to ensure stable operation of the detectors over a wide voltage range, with very low noise and high stability of their characteristics. The technology developed for fabrication of the detector electrodes opens a way to improve the level of gas purity in the detectors by a few orders of magnitude and provides a longer detector lifetime in comparison with similar devices.

References

1. V.A. Andreev *et al.*, Nucl. Instr. Meth. A **581**, 123 (2007).
2. V.A. Andreev *et al.*, Bull. RAS: Physics **72**, 1001 (2008).
3. V.A. Andreev *et al.*, Preprint PNPI-**2780**, Gatchina (2008).
4. V.A. Andreev *et al.*, Phys. Solid State **52**, 1029 (2010).

TESTS OF THIN-WALL DRIFT TUBES DEVELOPED FOR PANDA TRACKERS

A.P. Kashchuk, O.V. Levitskaya

The PANDA experiment will be carried out at the international FAIR facility in the GSI laboratory (Darmstadt, Germany). According to the Technical Design Report, the Forward Tracker (six stations FT1–FT6) [1] and the Central Straw Tube Tracker (STT) [2] will be composed from thin-wall drift tubes (called straw-tubes below) in large quantities, 13500 and 4600 tubes, respectively. The straw-tubes used here were produced by winding and gluing two Mylar aluminized films of 12 μm thickness (the wall thickness including the glue was ~ 27 μm). The tube wall was used as a cathode (R_{tube} = 5 mm), and the coaxial gold-plated W-Re wire was used as an anode of the counter (R_{wire} = 10 μm). The Mylar material was preferred to the Kapton one because of its better mechanical properties – a higher Young's modulus and tensile strength. The drift tubes are filled with two-component gas mixture Ar(90 %) + CO_2(10 %) at the 1 bar overpressure, *i.e.* at the 2 bar absolute gas pressure. The overpressure stretches the tube and prevents the wire sagging. The detector plane consisted of two mono-layers of drift tubes shifted by the radius R_{tube}, see Fig. 1a. The radiation length of a single tube X is characterized by X/X_0 = 0.05 %, where X_0 is the media radiation length. As a calculation shows, the maximum sag of a 20 μm wire inside of a 1.5 m long horizontal straw tube due to its weight is smaller than 35 μm at the wire tension of 50 g.

In this report, we summarize various laboratory measurements made on straw tubes of 0.75 m and 1.5 m lengths (Fig. 1a), as well as on two module prototypes. The experimental set-up is shown in Fig. 1b. The modules were installed horizontally (as in the STT) and also vertically (as in the FT).

An intense 1.3 GBq ^{137}Cs γ-source (660 keV) was used for gas gain measurements, because a very low ionization current (pA) had to be detected. A low intensity ^{55}Fe X-ray source producing a point-like ionization in only one straw tube within the module was used for gas gain uniformity tests and to investigate the counting characteristics and cross-talks. A collimated ^{90}Sr β-source (emitting electrons of ≤ 2.3 MeV) with the intensity 11 MBq was used for efficiency measurements and for estimation of the spatial resolution of a single straw tube within the straw-module prototype.

The gas gain measurements were performed in order to specify the operational voltage at the 2 bar absolute gas pressure and to study the gas gain variations versus voltage, pressure, temperature and wire diameter. The ionization current corresponding to the unity gas gain was measured using the intense 1.3 GBq ^{137}Cs γ-source. In order to eliminate offsets in measurements of very small currents, we used batteries (as a floating voltage source) at both positive and negative voltages applied to the anode wire with respect to the cathode. The auto-ranging Keithley-485 pico-ammeter with the sensitivity of 0.1 pA was connected between the cathode and the ground. The ionization current I_0 = 1.68 ± 0.17 pA was measured at ± 50 V and I_0 = 1.73 ± 0.12 pA at ± 100 V. The resulting value of I_0 = 1.70 ± 0.21 pA was obtained by averaging the partial results. The gas gain at any voltage V was calculated as the ratio I/I_0, where I was the current corresponding to the voltage V. Now the voltage was incremented in the range 1000–1900 V and the corresponding gas gain changed from 10^2 to 10^5, see Fig. 2a.

The gas gain versus voltage at several gas overpressures (above the atmospheric pressure) at fixed temperature is presented in Fig. 2b. The results of measurements were fitted by the Diethorn formula with two parameters, E_{min} and ΔV [3]:

$$G(V,\rho) = \left[\frac{V}{a\ln\left(b/a\right)\cdot E_{min}\dfrac{\rho}{\rho_0}} \right]^{\dfrac{V}{\Delta V}\cdot\dfrac{\ln 2}{\ln(b/a)}}. \tag{1}$$

Here, a and b are the radii of the anode wire and cathode tube, respectively, E_{min} is the minimal electric field needed for ionization, ΔV corresponds to the minimal voltage difference required to produce free electrons in an avalanche; $\rho/\rho_0 = (P/T)/(P_0/T_0)$ and P/T are the ratios of gas density, pressure and temperature at the real conditions to the reference ones P_0 = 1000 mbar, T_0 = 293 K, respectively.
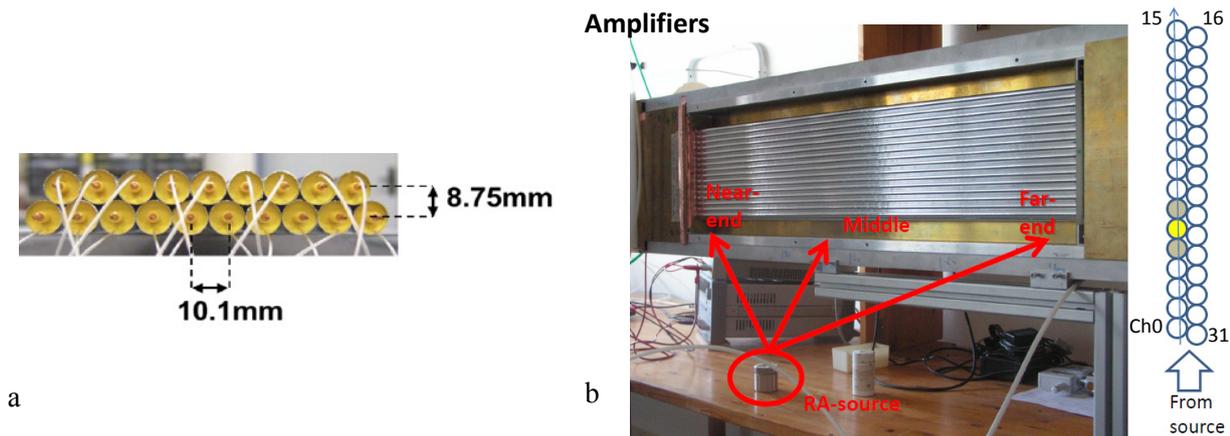
Fig. 1. Two mono-layers of thin-wall drift tubes filled with Ar(90 %) + CO$_2$(10 %) mixture at the 2 bar absolute gas pressure (a) and double layer 32-straw module prototype used in laboratory tests with various radioactive sources (b)
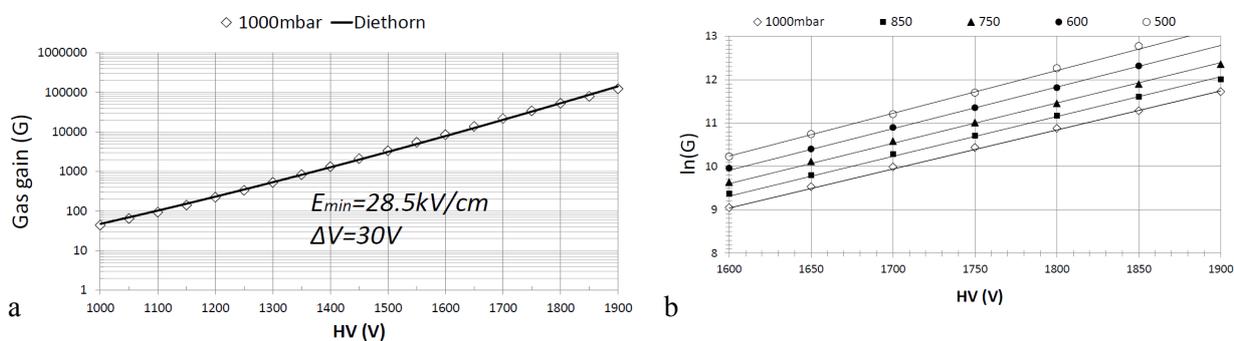

Fig. 2. Gas gain *vs* voltage for Ar(90 %) + CO$_2$(10 %) gas mixture at the 1000 mbar overpressure, (at the 2 bar absolute gas pressure) and the Diethorn parametrization of the measurement results (a). The gas gain *vs* voltage at various gas overpressures ranged from 1000 mbar down to 500 mbar (b). The points correspond to the measurements, the lines – to the parameterization function

Tests with the [55]Fe-source were performed to find a set of characteristics. In these measurements, the straw-tube impedance was terminated with the amplifier impedance via a 350 Ohm resistor connected in series to the amplifier, while the far-end of the straw-tube was un-terminated [4]. In Fig. 3a, a typical amplitude spectrum is presented, which was used to verify the gas gain uniformity along the straw-tube. In the case of an individual straw tube, the sag can modify the gas gain dramatically in the middle of the tube. But for the 32-straw module where the tubes were arranged in double layer and glued together, the gas gain is rather uniformly distributed. In this case the gas gain non-uniformity in the middle of any tube within the module is below 1 %, as it is shown in Fig. 3b.

Figure 4a shows three typical regions observed in the counting characteristics measured with the [55]Fe-source: the beginning of the plateau (the point corresponding to 5.9 keV), the constant rate region (the plateau) and the region of increasing counting rate above the end of the plateau. The measurements show rather similar counting rates for all straw tubes within the 32-straw module in all regions mentioned above: at the near-end (at the amplifier side), in the middle and at the far-end. The rise of the counting rate correlates with the growth of the dark current and appearance of two and more pulses (cross-talks). The position of the plateau end strongly depends on the quality of straw-tube production. The [55]Fe X-ray source produces point-like ionization in the gas and generates signals in one and only one straw tube. This feature makes possible to measure the cross-talks in any pair of tubes within the module. As is shown in Fig. 4b, typical cross-talks were observed on the level of 0.2 % in a wide range of voltages up to 1900 V in some cases, and only near the end of the plateau they could reach 10 % and even 100 %.

The efficiency of particle detection was measured with the collimated ^{90}Sr-source with the aim to specify the operational voltage for registration of MIPs (minimum ionizing particles). The particles emitted by the ^{90}Sr-source cross many tubes, as illustrated in Fig. 5a. A set of three neighboring tubes was used to find the efficiency of the inner tube with respect to the outer tubes. The efficiency was measured at both ends and in the middle of the tube. Figure 5a shows the efficiency versus voltage at a fixed threshold of 10 fC. Figure 5b shows the dependence of the efficiency on the threshold for several voltages.
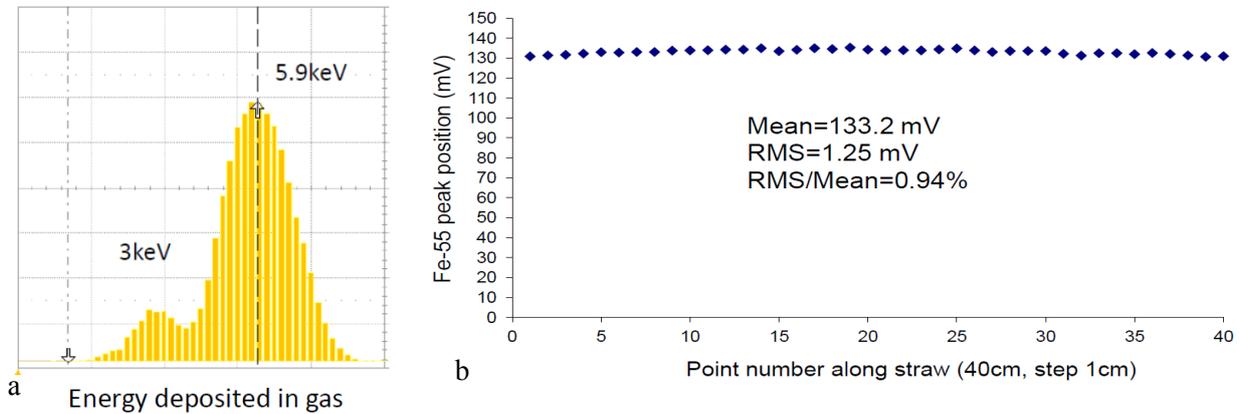
Fig. 3. Typical amplitude spectrum measured with the ^{55}Fe-source in a single tube within a 32-straw module (a). Gas gain variation in the tube measured as the position of the 5.9 keV peak along the distance of 40 cm in the middle of the tube (b)
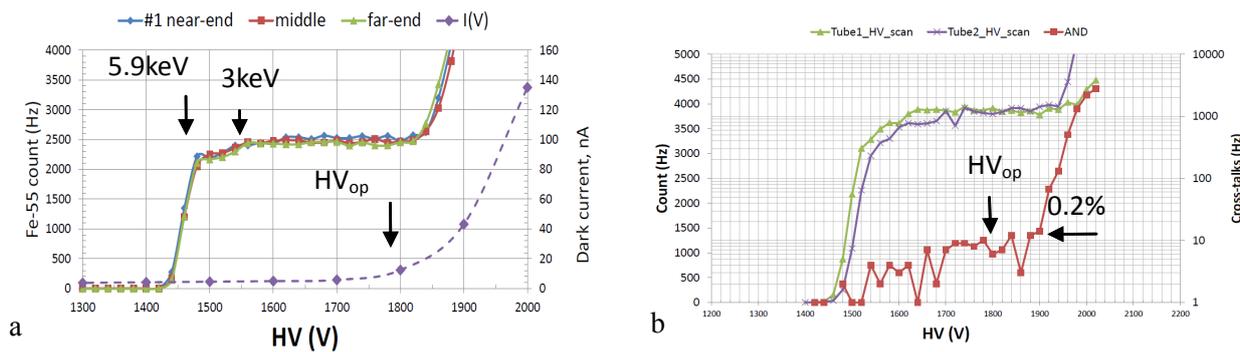
Fig. 4. Counting characteristics measured with the ^{55}Fe-source at a sequence of points along a 0.75 m straw tube filled with Ar(90 %) + CO$_2$(10 %) mixture at the 2 bar absolute gas pressure (a). The cross-talks measured with the ^{55}Fe-source between two straw tubes of 1.5 m length (b). HV$_{op}$ = 1800 V is indicated as the operational voltage for registration of MIPs

We have compared the results of the efficiency measurements obtained with the ^{90}Sr-source and with Cosmic Rays (CR), performed at large statistics, collected for many days, for all straw tubes within the 32-straw module. The measurements with CR were made at the HV = 1800 V (Fig. 6a) and HV = 1700 V (Fig. 6b). One can notice that the results obtained with ^{90}Sr and CR are consistent. Comparing the data in Figs. 5a, b and 6a, b we see that the operational voltage should be at least 1800 V. According to Fig. 2a, the gas gain at the HV = 1800 V is equal to 5.5×10^4. A similar gas gain at the HV = 1800 V was obtained in a cross-check using the ^{55}Fe-source by measuring both the rate (see the plateau in Fig. 4a) and the current. If the gas gain is known, we can map the threshold of 10 fC to 10 p.e. (primary electrons). Then, the efficiency with such a threshold has to be better than 95 % at 200 p.e./cm, which is the total number of primary electrons formed along the track of a MIP at the 2 bar absolute gas pressure, assuming a uniform distribution of primary clusters along the track. In reality, the efficiency will be better and close to 100 % in a 2-layer detector.
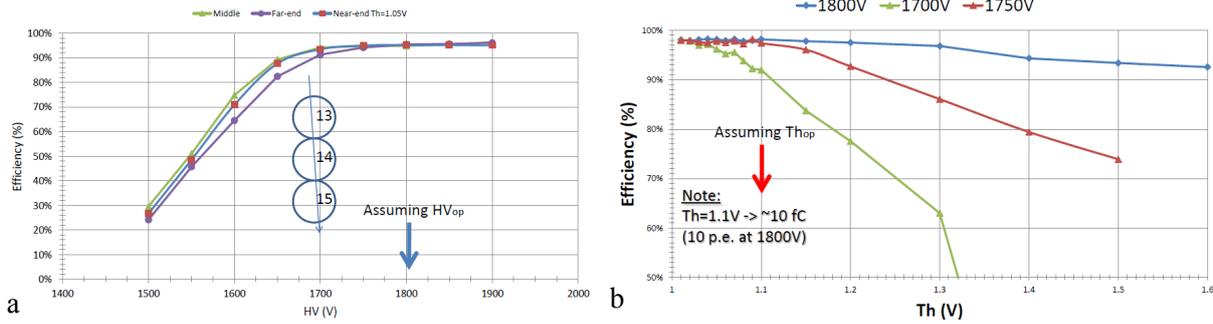
Fig. 5. Efficiency *vs* voltage at a fixed threshold for various points along a straw tube (a), and efficiency *vs* threshold at fixed voltages at the wire (b). Both characteristics were obtained in few minutes with the ^{90}Sr-source using the "three neigbouring tubes" method
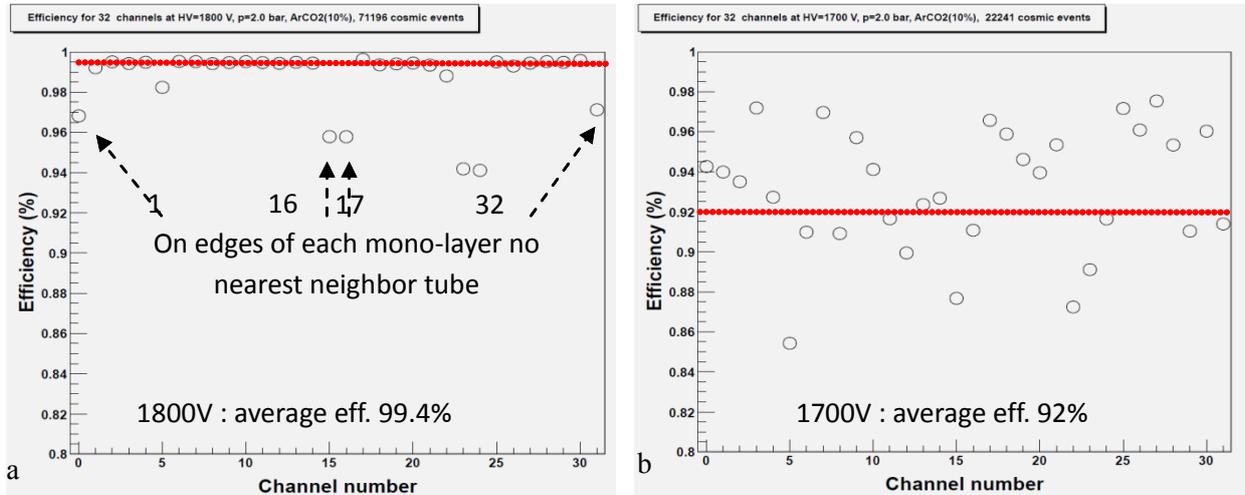

Fig. 6. Efficiency of straw tubes within a 2-layer (16 + 16 = 32 straw) module at the HV = 1800 V (a) and HV = 1700 V (b) obtained with CR with large statistics collected for many days

Further tests were performed to estimate the single-straw spatial resolution by observation of time spectra. The time-to-digit conversion was made with a 128-channel CAEN TDC module V1190A with the time resolution 100 ps/bin. Our ^{90}Sr source of charged particles for laboratory tests is a unique one, it allows to obtain large statistics in a few minutes (10^5 events in 20 min), while many days are required with CR. Nevertheless, this source in not appropriate for accurate measurements of the spatial resolution due to low energies of electrons (maximum 2.3 MeV), because significant multiple scattering in the gas and material of the detector deteriorates its spatial resolution.

Measurements of TDC-spectra with ^{90}Sr were carried out at the operational voltage of 1800 V and threshold 10 p.e. As one can see in Fig. 7a, b, primary electrons drift without multiplication practically through all the distance R_{tube}. Avalanches in the gas start at the distance $r \approx 102$ μm from the anode wire, at the electric field $E_{min} = 28.5$ kV/cm, as is shown in Fig. 2a.

Raw TDC-spectra measured with the ^{90}Sr-source are "corrupt" due to two main processes. The first process is clusterization of primary ionization along the track, the second is multiple scattering of low energy electrons emitted by ^{90}Sr. As it is illustrated in Fig. 8a, b, many primary electrons drift to the wire from the track with different starting velocities, and they can produce two or more pulses (hits). The first pulse is used as a rule to determine the spatial coordinate. However, the second pulse from the same track (or even the 3-rd) can be also registered with a multi-hit TDC. As one can see in Fig. 9a, b in the two-dimensional plot and its projections, low energy electrons scattered in the gas, on the wall and also on the glue can randomly "deform" the shape of the TDC-spectrum. In such a case, the 1-st pulse can be wrong, *i.e.* it can be not related to the closest electron cluster to the wire.

The spatial resolution of a single straw-tube was obtained using the so-called "auto-calibration" technique described in detail in [2]. Parameters of the TDC-spectrum and the corresponding $r(t)$-relation (Fig. 10a, b) for each channel were derived from a fit performed with the following empirical function:

$$\frac{dn}{dt} = p_1 + \frac{p_2[1 + p_3 \exp((p_5 - t)/p_4)]}{[1 + \exp((p_5 - t)/p_7)][1 + \exp((t - p_6)/p_8)]}. \tag{2}$$

Here, dn is the number of events within the time bin dt in the TDC-spectrum, the parameters p_5 and p_6 are the values t_{min} and t_{max}, their difference being the maximum drift time in the straw-tube; other parameters describe the spectrum shape.
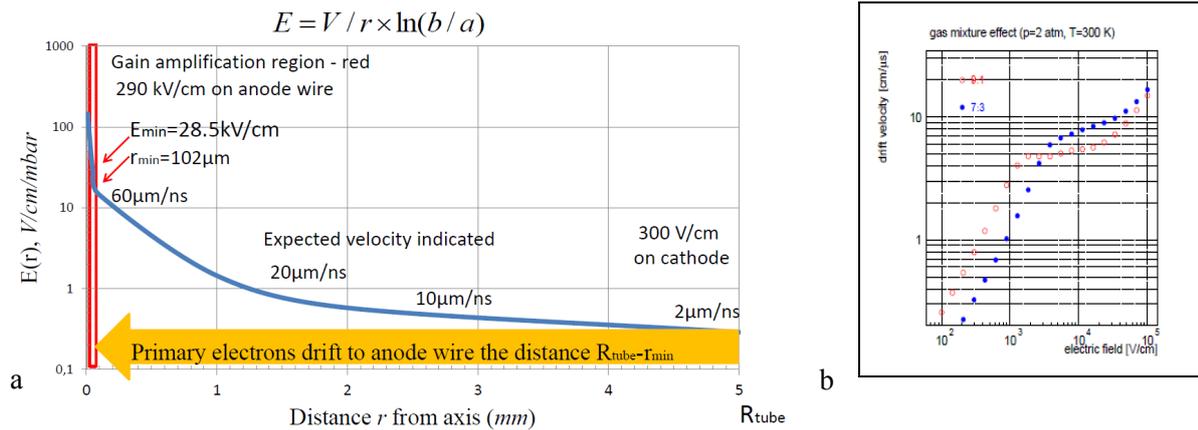
Fig. 7. Electric field strength in a tube at 1800 V with indication of the electron drift velocities at certain field values (a). Electron drift velocity *vs* electric field for two-component gas mixtures Ar + CO$_2$ at the 2 bar gas pressure [2]: open red points – our case of Ar(90 %) + CO$_2$(10 %), blue points – Ar(70 %) + CO$_2$(30 %) (b)
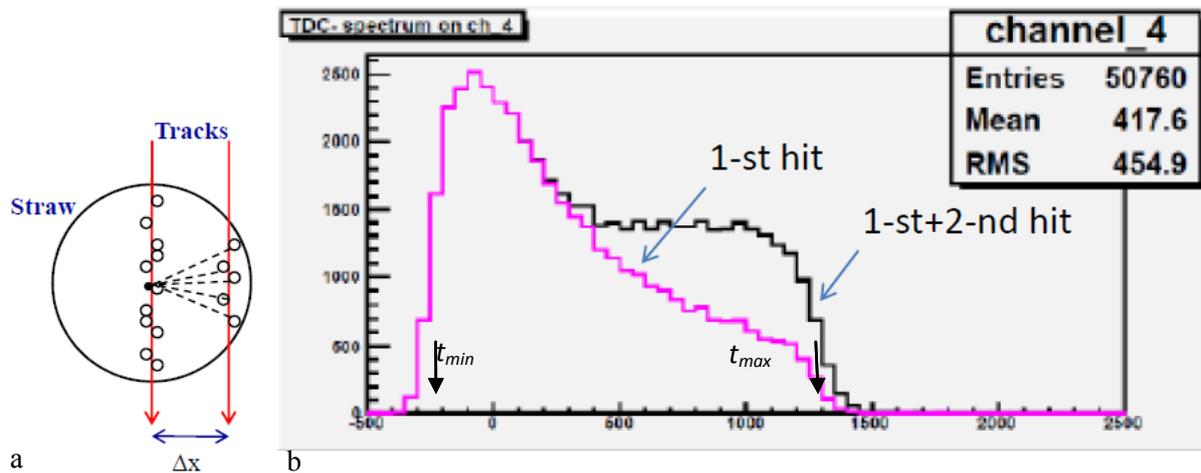

Fig. 8. Origin of multiple pulses due to clusterization of primary ionization along the track (a); TDC-spectrum measured with the ^{90}Sr-source including only the 1-st pulse and a sum of the 1-st and 2-nd pulses (b). With multiple scattering, the 1-st pulse can be generated by a cluster not nearest to the wire. The time scale is in the TDC sampling units, one histogram bin containing 50 sampling units
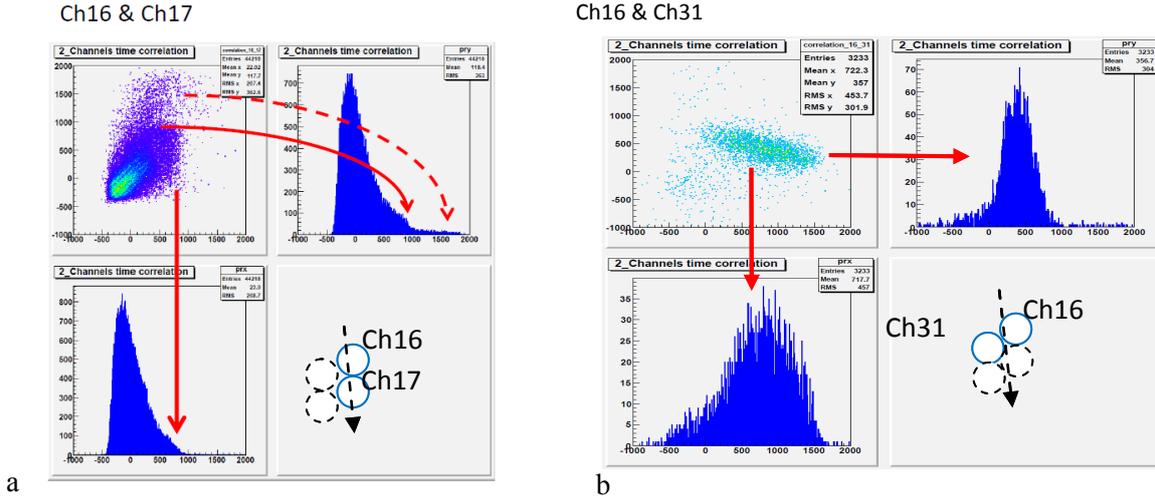
Fig. 9. 2D plot of the correlation between two time intervals for two tubes Ch16 and Ch17 from the same straw monolayer, measured with the ^{90}Sr-source with TDCs, and the 1D TDC-spectra obtained as its projections (a). The same plot for another pair of tubes Ch16 and Ch31 taken from different monolayers (b). The tails, as well as spurious hits on the level of ~ 20 % in the TDC-spectra, appear due to multiple scattering. To obtain correct TDC-spectra and the $r(t)$-relation, a special hit selection is provided in the event analysis

The $r(t)$-relation has been found from the TDC-spectrum with N_{tot} entries using the following formula:

$$r(t) = \int_{t_{min}}^{t_{max}} \frac{dr}{dt} \cdot \frac{dn}{dn} = \frac{R_{tube} - R_{wire}}{N_{tot}} \int_{t_{min}}^{t_{max}} \frac{dn}{dt} \approx \frac{\sum_{i=1}^{i=i_t} n_i}{N_{tot}} \cdot (R_{tube} - R_{wire}). \tag{3}$$

For further conversion from the measured time to spatial coordinate, the $r(t)$-relation was parameterized by the Chebyshev polynomial of the 5-th order:

$$r(t) = q_0 + q_1 t + q_2 (2t^2 - 1) + q_3 (4t^3 - 3t) + q_4 (8t^4 - 8t^2 + 1) + q_5 (16t^5 - 20t^3 + 5t). \tag{4}$$

Here, t is the time interval measured as the radius of an isochrone, *i.e.* the distance from the primary cluster to the wire; the parameter q in Fig. 10b has been replaced by p.
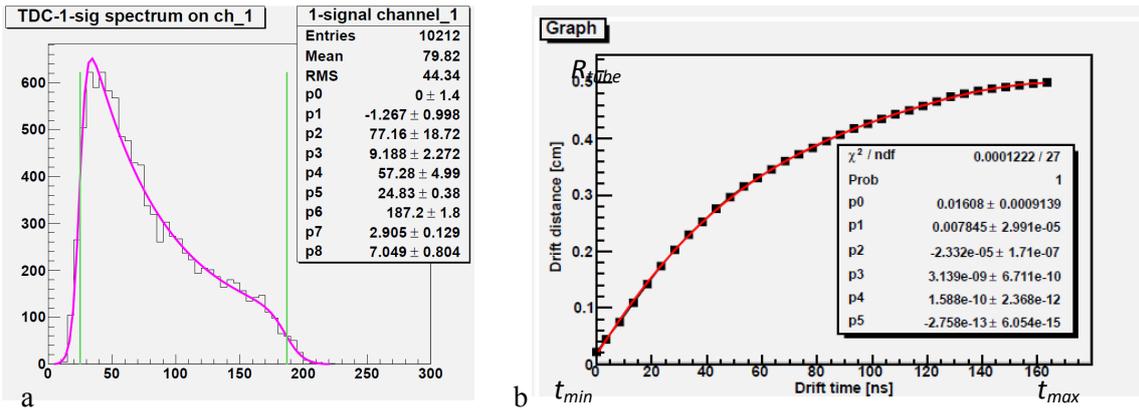

Fig. 10. TDC-spectrum measured with the ^{90}Sr-source for one straw tube (time in ns) (a), and the corresponding $r(t)$-relation with the parameters (b)
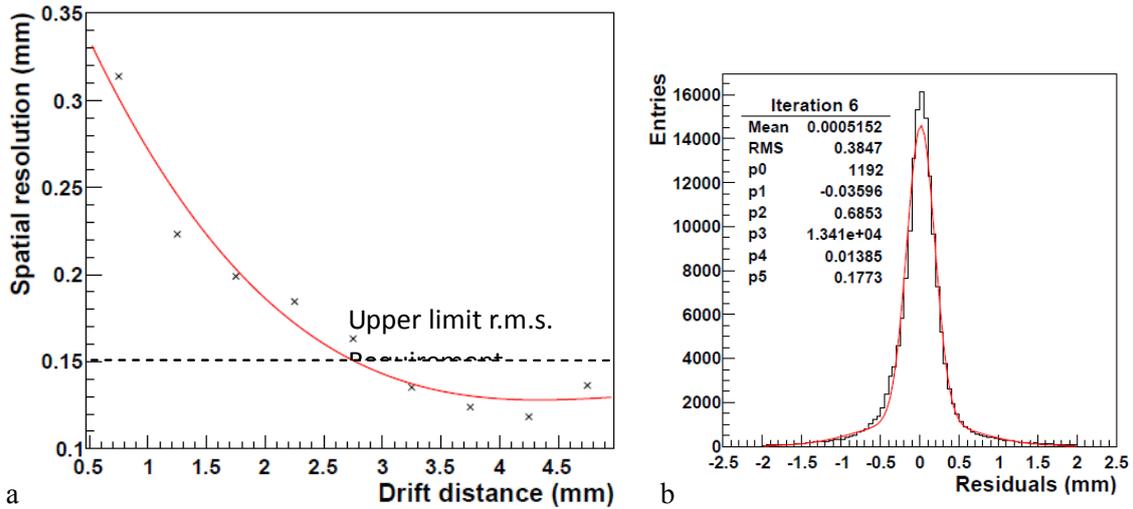
Fig. 11. Spatial resolution measured with the ^{90}Sr-source as a function of the distance between the track and the wire (a). The averaged distribution of residuals and its r.m.s., p5 = 177.3 µm (b). The spatial resolution specified for the PANDA experiment is indicated by the dashed line

According to the auto-calibration, the final $r(t)$-relation is obtained sequentially by iterations using various hit selection criteria. The residuals, which are the differences between the best track and $r(t_i)$, are minimized by this iterative procedure (t_i is the measured time interval in the i-th TDC-channel).

As one can see in Fig. 11a, a much better spatial resolution is obtained in the region from $R_{tube}/2$ to R_{tube} within each mono-layer shifted by R_{tube} if the data are not averaged over the full interval R_{tube}. Using this effect, one can combine the data properly from two independent monolayers in order to improve the spatial resolution.

The upper limit of the spatial resolution specified for the PANDA experiment is 150 µm (r.m.s.). According to the TDR, the resolution like that will provide the momentum resolution of the order of 1 %.

A large spread of the parameters of Eq. (2) describing the TDC-spectra of the 32-straw module was observed due to multiple scattering of low energy electrons, emitted by ^{90}Sr in a wide energy range around 2 MeV. As could be expected, this explains why the spatial resolution measured with the ^{90}Sr-source is worse than that predicted by simulations, see Figs. 11a, b and 12a, b, c.
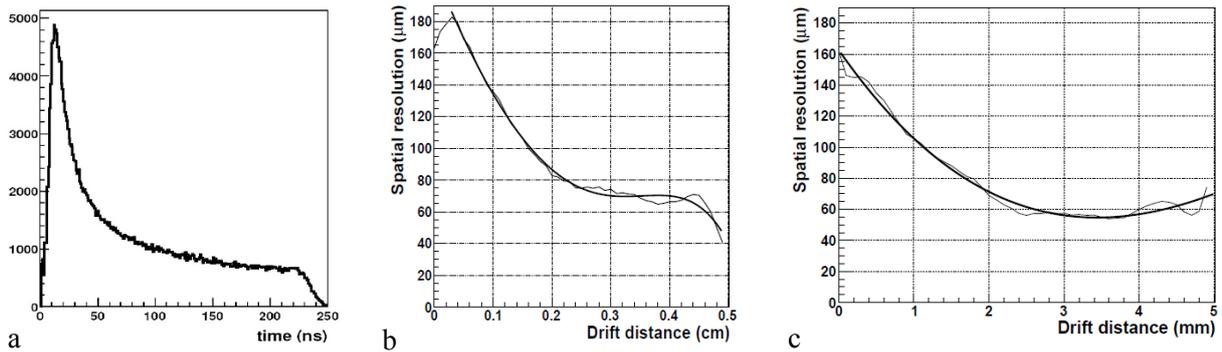

Fig. 12. Simulation of a TDC-spectrum for MIP particles. As the simulation shows, the magnetic field extends the drift time to 220 ns (a). Single straw-tube spatial resolution (r.m.s.) *vs* distance to the wire found without a magnetic field (b) and with a magnetic field (c). In the range between $R_{tube}/2$ and R_{tube}, the resolution is around 70 µm (r.m.s.). These results were taken from [2, 5]

Our goal at present is to prepare the apparatus, technique and software for beam tests with high energy particles at various rates with and without magnetic fields and to compare the results of measurements with

simulations. Note that tests with radioactive sources are good tools for straw-tube quality control at the mass production and provide feedback on possible improvements of the module assembly procedures.

This work was performed in collaboration with P. Gianotti and M. Savrie.

References

1. PANDA Forward Tracking System. Technical Design Report (in preparation).
2. PANDA Central Straw Tube Tracker. FAIR/Pbar/Technical Design Report, Darmstadt (2012), http://panda-wiki.gsi.de/pub/Tracking/WebHome/panda_tdr_trk.pdf
3. P. Gianotti, A. Kashchuk… O. Levitskaya *et al*., Note LNF-**11/05** (P), Frascati (2011).
4. A.P. Kashchuk… O.V. Levitskaya *et al*., Phys. of Particles and Nuclei Letters **8**, 40 (2011).
5. S. Costanza… A. Kashchuk… O. Levitskaya *et al*., Nuovo Cim. **34** C, 94 (2011).

CBM RICH PROTOTYPE GAS SYSTEM

L.M. Kotchenda, P.A. Kravtsov

1. Introduction

The Compressed Baryonic Matter (CBM) experiment is a heavy-ion experiment at the future FAIR facility being designed to explore the intermediate range of the QCD phase diagram in the beam energy range from 10 to 45 A GeV. With its physics program, CBM will investigate properties of the dense baryonic matter and the expected phase transition between the hadronic and partonic matter. Among the key observables are the low-mass vector mesons and the charmonium decaying into lepton pairs. In CBM, electrons with energies lower than 8 GeV/c will be identified by a RICH detector, which is being developed at several laboratories. In addition, the detector will improve the kaon/pion separation at the momenta higher than 4 GeV/c.

The concept of the RICH detector involves CO_2 as the radiator gas, spherical glass mirrors reflecting the Cherenkov radiation to an array of Multianode Photomultipliers as photo detectors. The CO_2 gas has been chosen because it has the Lorentz factor of 33.3, the radiation length of 183 m and the pion momentum threshold for Cherenkov light production of 4.65 GeV/c, thus representing a very good compromise to fulfill the CBM RICH requirements.

The RICH detector requires stable differential pressure of the CO_2 gas above the atmospheric pressure, as many of gaseous detectors, which requires to ensure mechanical stability of the detector volume. The radiator gas must be free of moisture and oxygen. Additional measurements should be carried out to investigate temperature influence on the detector performance.

2. Gas system design

The primary purpose of the CBM RICH Prototype gas system (Fig. 1) [1] is to provide pure CO_2 gas to the RICH prototype at the correct differential pressure. Its design is based on the gas systems for the STAR and PHENIX experiments at BNL [2–4]. The system operates nominally as a closed circuit gas system with the majority of gases recirculating through the prototype. During the normal operation, the fresh gas is added with a Burkert 8711 mass flow controller FM1. To support constant differential pressure at the 2 mbar level measured with the pressure transmitter PT4, the control system will change the flow through the FM1 controller. If the differential pressure is increasing, the gas flow through FM1 will be reduced. And vice versa, in the case of a differential pressure drop, the flow through FM1 will be increased. The gas system can be operated in an open configuration for purging.

A bypass valve (BMV1) is manually adjusted to enable the optimum flow rate through the prototype. The purity of the recirculating gas is monitored using Panametrics Oxygen (O2X1) and Humidity (MMS35) analysers. A fraction (up to 30 %) of the recirculating gas can be passed through the purifier and dryer to remove oxygen and moisture. There is a possibility to check the gas purity with the analysers after the purifier and dryer to determine their saturation.

The Purifier is filled with active copper. Its operating and regenerating temperature is 220 °C. A Temperature Indicating Controller TIC1 supports this temperature level. The mixture $CO_2 + 5$ % H_2 can be used to regenerate the Purifier. The oxygen content after the purifier is about 2–3 ppm. The Dryer is filled with NaX (13X) molecular sieves. Its normal operating temperature is 22 °C. The water content at this temperature is 1–2 ppm in the Dryer output flow. The regeneration of the Dryer is performed at 350–400 °C supported with the TIC2.

A computer driven data acquisition/control system monitors all the process variables and provides stabilization of the RICH prototype differential pressure. The computer system flags the quantities which fall outside of the predefined limits and initiates corrective actions. Using data from the TT1, PT4 and BP (Barometric Pressure) sensors, the computer system estimates the value of the CO_2 refraction index.

The gas system is assembled in a single 19″ rack and can be easily transported with the RICH prototype. It can also be used in the future for the complete RICH detector with minor changes.
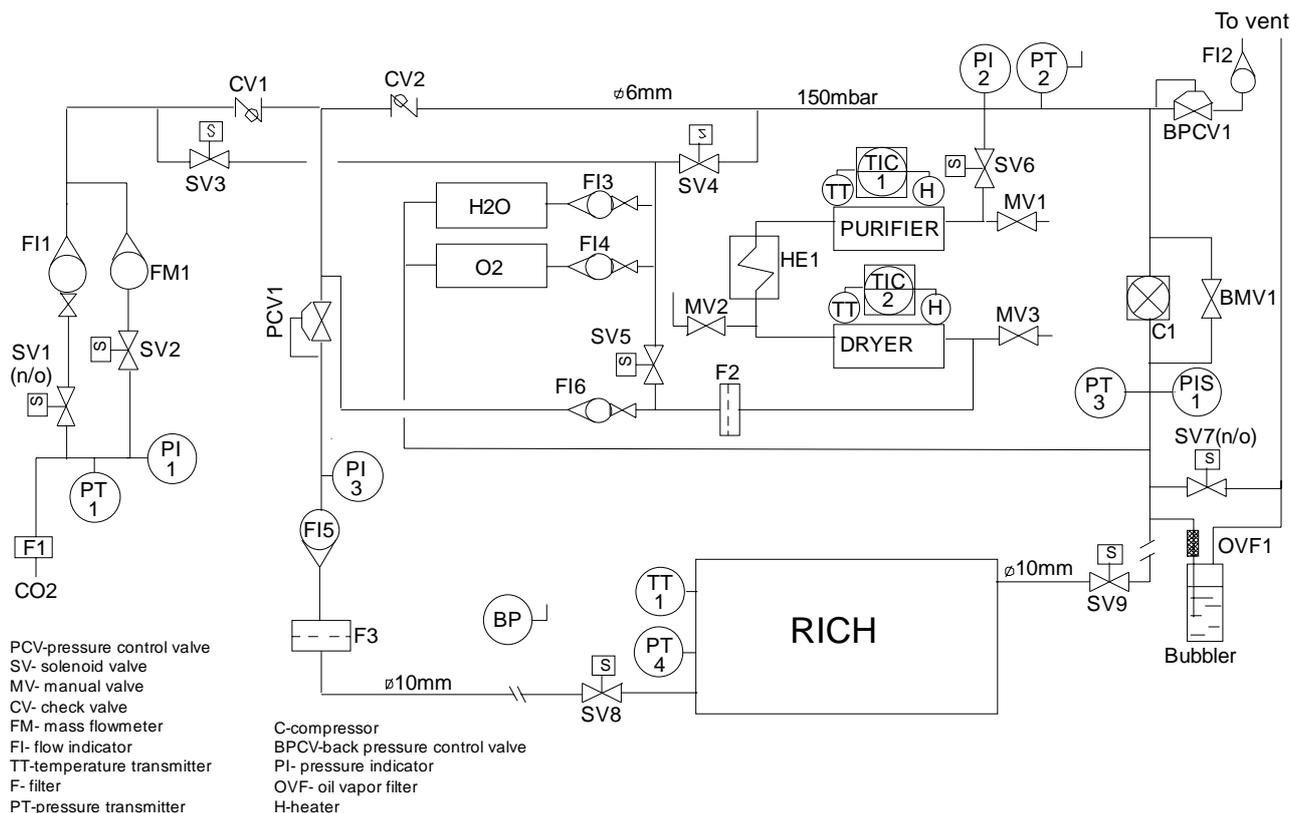
Fig. 1. CBM RICH Prototype gas system

3. Slow control subsystem

The CBM RICH gas system is controlled by a custom slow control subsystem [5] that is based on the data acquisition DAQ32 module [6]. This module was designed for controlling small cryogenic and gas supply systems. It provides reading of up to 32 sensors with industrial standard voltage or current outputs. The device precision is 0.004 % of the measurement scale, which can be selected from the range of +(0–4) V, ± 5 V, +(0–10) V, ± 10 V. The module is also equipped with 16 buffered digital outputs to control acting devices like solenoid valves or compressors, and 4 analog voltage outputs for flow controllers or heaters. Such input-output channel density allows to control small systems like the CBM RICH gas system with a single module.

The variety of data exchange interfaces simplifies the connection of the instrument to an external control system or to a computer. Flexible controller firmware allows implementing the necessary control algorithms like the PID regulation, directly in the firmware. Two of these modules (one working and one spare) are mounted in the gas system rack.

Control computer software [7] has been developed for the Windows platform. It provides reliable data acquisition, automated handling of alarm conditions and manual control of the gas system. All the alarm events and system variables are logged into a database. The software is split into multiple processes that communicate, making use of special operating system kernel objects.

The main process reads all the sensor values and passes them to other processes. In order to make the software more reliable, it has been divided into two threads: one for the Graphical User Interface (GUI) and one for the data acquisition. The GUI thread shows all the gas system parameters including the valve states in the main window. The operator can also use the controls to manage the system manually, as well as adjust the alarm parameters.

The DAQ thread acquires all the process variables, writes them into shared memory and checks the alarm conditions. Every alarm setting contains an alarm threshold, an alarm message and a control template. The template indicates the alarm set and the release actions for every controlled device, *e.g.*, a valve or a

compressor. The system makes corrective actions automatically and alerts the operator about the problem. Alarm control templates provide the user with a high degree of flexibility when setting up the system. All the process variables are written into the MS Access database with a specified period. In the case of an alarm trigger, the current values are written out in turn. All the alarm events and software messages are logged into the same database.

It is also useful to have a fast access to particular data and to plot the results during the gas system operation. A special tool (DBViewer) has been developed to work with the gas system database. It provides visualization of the data for any gas system process variable and exports the data from the database to an MS Excel file or tab-delimited text file for further analysis.

One more program has been designed for visualization of the actual state of the system. This program (Charts) displays up to ten selected parameters in the time chart format. Besides, it can be used for a tabular display of the process variables, with extra alarm signals for every parameter in the table. In addition, the TCP/IP client/server is implemented in the Charts software so that it can be used remotely to monitor the system under control.

The gas system control software was successfully used in nine gas systems [2, 3] for several detectors in the STAR and PHENIX experiments at RHIC.

4. Test beam results

During the test beam run in October 2011 at CERN, we had a good opportunity to test the gas system. The major task was to check the differential pressure stability of the RICH prototype in the recirculation mode during stable operation. Figure 2 features the results of our pressure regulation. Obviously, the differential pressure of the RICH prototype was stable at 2.0 ± 0.1 mbar, although the barometric pressure PTB varied in the range of 22 mbar. We can see the same results for the STAR and PHENIX gas systems [2–4], in spite of different control technique. For the STAR and PHENIX gas systems, mass controllers were used to prepare a fresh mixture with a very stable content. The fresh mixture was added to the system gas at a constant flow, and therefore the pressure of the detector was stabilized using a dedicated PID-controller in the recirculation mode.
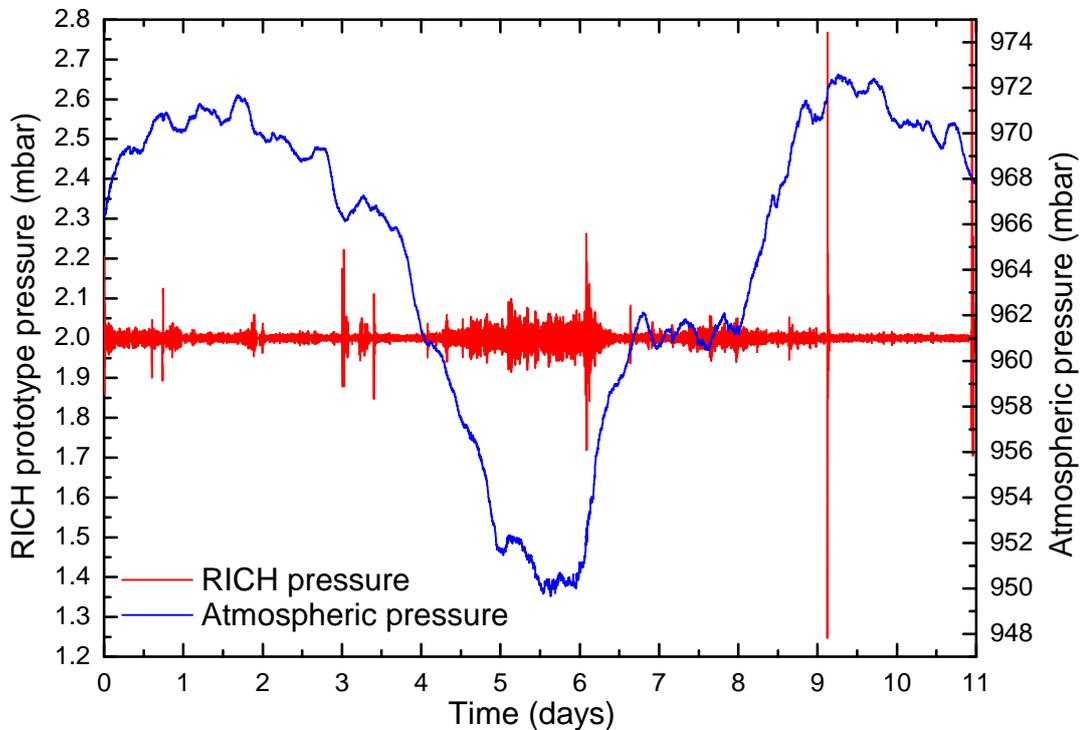

Fig. 2. Detector differential pressure (red line) and the atmospheric pressure (blue line)
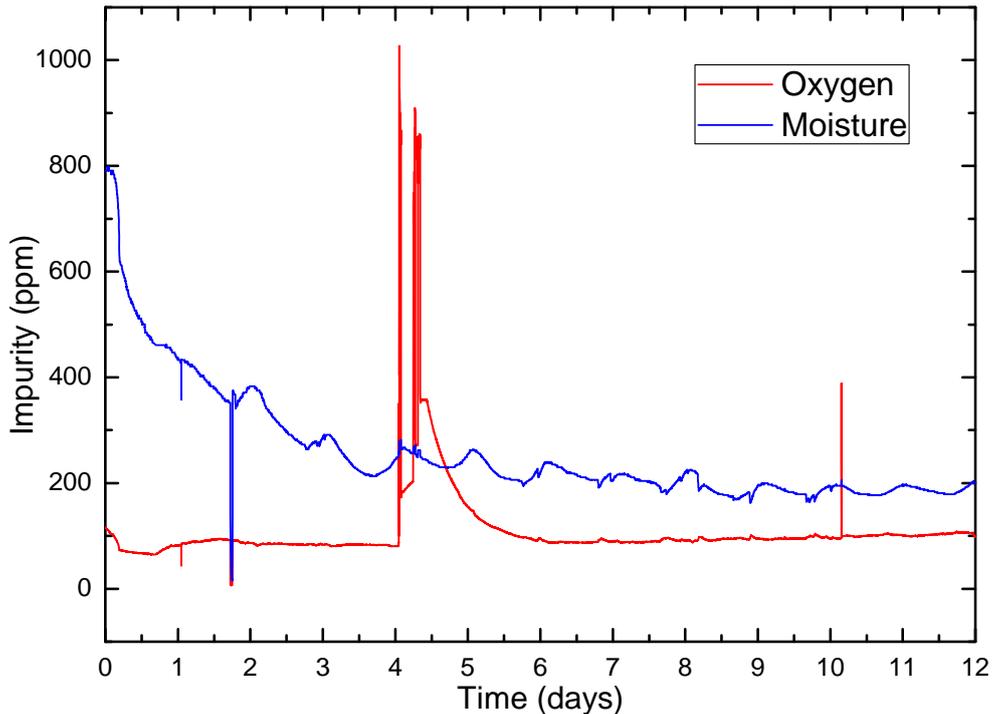
Fig. 3. Oxygen (red line) and moisture (blue line) content

The efficiency of the gas system Dryer and Purifier was also checked. Test results are shown in Fig. 3. It should be mentioned that the inner RICH prototype surface was not treated with a special cleaning process, and we had a lot of water and oxygen adsorbed by the walls of the RICH vessel and the inner structure elements. Even at these conditions, both the Dryer and Purifier had enough efficiency to remove moisture and oxygen to the required level.

The gas system was also used to add a certain amount of oxygen in order to check the detector operation at a higher oxygen content (the spikes in the oxygen line on the fourth day in Fig. 3). The oscillations of the moisture content are caused by daily temperature changes in the hall.

In general, the gas system provided stable operation with stabilization of all the required gas parameters in the RICH prototype. It was reliably operated by the control system, providing all the system parameters to the external slow control system. The RICH prototype vessel ($3.5 \, \text{m}^3$) was checked for leaks prior to the beam time. Measuring the pressure decrease in the vessel, we have estimated the leak rate to be below the sensitivity of the gas system (≤ 50 sccm).

References

1. L. Kotchenda *et al.*, CBM Progress Report, Darmstadt (2010).
2. L. Kotchenda *et al.*, STAR TPC Gas System, NIM A **499**, 703 (2003).
3. L. Kotchenda *et al.*, PHENIX Muon Tracking Detector Gas System, NIM A **578**, 172 (2007).
4. L. Kotchenda *et al.*, Preprint PNPI-**2712**, Gatchina (2007).
5. P. Kravtsov *et al.*, CBM Progress Report, Darmstadt (2010), p. 32.
6. P. Kravtsov and V. Trofimov, Preprint PNPI-**2723**, Gatchina (2007).
7. P. Kravtsov, Preprint PNPI-**2593**, Gatchina (2005).

RECOVERY OF AGED ANODE WIRES IN PROPORTIONAL COUNTERS USING A NEGATIVE CORONA DISCHARGE IN 80 % CF$_4$ + 20 % CO$_2$

G.E. Gavrilov, A.G. Krivshich, D.A. Maysuzenko, A.A. Fetisov, N.Yu. Shvetsova

1. Introduction

During last few years, large-scale studies of the radiation hardness of gaseous detectors were carried out in preparation for LHC experiments. Today, most of the factors affecting the aging rate of these detectors are well defined [1].

The "classical aging effects" are the result of chemical reactions occurring in the avalanche plasma near anode wires leading to formation of deposits on the electrode surfaces. This mode of aging is extremely sensitive to various additives and contaminants in the gas and materials used in contact with the gas. The most harmful chemical element, which is systematically detected in analyses of wire deposits, is silicon. Si compounds are found in gas-system components, sealant Room Temperature Vulcanizing Silicone Rubber, silicon-based lubricant, *etc*. Usually, Si deposits appear at the accumulated charges much below 1 C/cm per wire. That is why most of the materials used for construction of the detectors have to be tested to address their safety from the aging point of view.

Due to the need for radiation hardness, a broad list of conventional working gas mixtures was narrowed down to Ar(Xe) + CO$_2$ + CF$_4$. These mixtures block the negative influence of silicon deposits, preventing the anode aging. However, at the accumulated doses above 1 C/cm per wire, there exist aging effects that are not related to polymerization.

Anode wires are commonly made of gold-plated tungsten. It has been found that oxygen and other active radicals produced in avalanches penetrate through the pores and micro-cracks in the gold-plating and react with tungsten [2]. This process results in swelling of the wires because the forces within a wire break the gold-plating, and tungsten oxides (WO$_x$) appear on the wire surface. The aim of the present work was to demonstrate recovery of an aged anode wire in a proportional counter by treating it with a negative corona discharge in a 80 % CF$_4$ + 20 % CO$_2$ gas mixture.

2. Test set-up

Aging tests of straw-tubes were carried out using three ^{90}Sr β-sources mounted in a line with a total rate at one straw of 15 MHz. The beam profile of the irradiated zone was uniform with the width about 35 mm. Two straw-tubes used in our investigations had 0.4 cm diameter, and the anodes were made of 50 μm gold-plated tungsten wires. The gas flow rate was 0.5 cm^3/min, which was equal to four straw volumes per hour. To avoid both air and water vapor penetration into the straws from the outside, a set of straws was placed in a sealed box blown over by argon. Measurements of the straw tube properties were performed regularly each day after every charge accumulation increment of about 0.13 C/cm during the exposure [3, 4].

To monitor the gas gain, the photo peak position of a collimated ^{55}Fe *X*-ray source (E_γ = 5.9 keV) in the amplitude spectrum was measured at different test points along the irradiated straw. During the aging tests, we chose several working points of the high voltage to achieve gas gains and irradiation currents over a wide range: 2×10^4, 5×10^4, 1×10^5 and 0.38 μA/cm, 0.97 μA/cm, 1.98 μA/cm, respectively. This has covered the gas gains commonly used in gaseous wire detectors.

An analysis of the anode surface after the aging procedure was performed using a scanning electron microscope with *X*-ray emission (0–10 keV) spectroscopy (SEM/XEM).

3. Aging test results

Usually after accumulation of the total charge of about 1.5−1.8 C/cm at the rate of 0.13 C/cm per day, the wire degradation resulted in the gas gain reduction of about 10−15 %. The results of the SEM/XEM analysis of the aged anode wire in the centre of the irradiated zone (the gas gain being $G = 5 \times 10^4$) are presented in Fig. 1. As one can see, the gold coating was broken, and the tungsten oxide compounds

penetrated through the cracks in the gold layer and almost covered the surface of the swollen wire. As a result, the wire diameter increased by 6 % from 50 to 53 μm.

In principle, one known way to clean the wire surface from Si compounds and extend the operational lifetime of a straw detector non-invasively is to etch the wires by using a high current gas discharge in gas mixtures with CF_4 [5, 6]. We have applied this technique to WO_x cleaning, too.
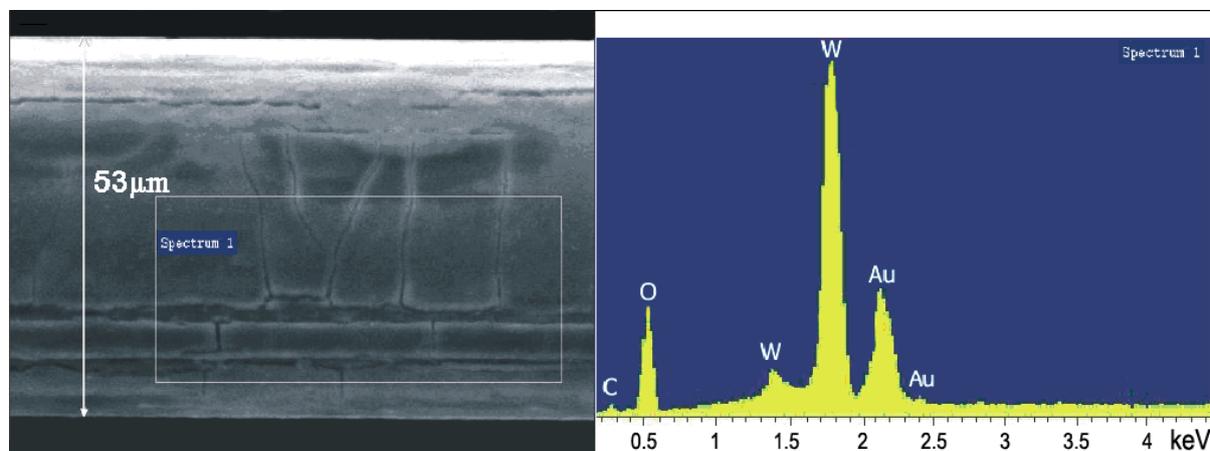

Fig. 1. SEM micrograph of the anode wire surface in the centre of the irradiated zone after the charge accumulation of Q = 1.53 C/cm (left) and XEM spectra (right) of the area that is denoted at the SEM micrograph by the rectangle

4. Task-setting

4.1. Glow discharge and integrated circuits production

Plasma chemistry is extensively applied in fabrication of semiconductor devices for microelectronic industry, which typically makes use of a glow discharge, which represents a low-pressure (< 1 Torr, RF-13.6 MHz) plasma. The glow discharge (DC, RF-plasma) in CF_4/O_2 gases is widely used in integrated circuits production for etching of silicon and tungsten compounds [7–9]. Our idea was to use this experience for removing tungsten oxides from the anode wire surface.

4.2. Corona discharge in wire chambers

The dominant parameter of a wire chamber is a strong non-uniform electric field around an anode wire. A classical corona discharge occurs in gases in regions of high electric field near sharp corners, edges of metal surface, including small diameter anode wires of MWPCs under atmospheric pressure. A start of a corona discharge in a straw (or MWPC) manifests itself with a sharp current increase.

It was observed that the gaseous products formed in avalanches in a proportional counter are qualitatively the same as expected under assumption that the chemical mechanisms in the avalanches are similar to the mechanisms of a low-pressure glow discharge [10–14]. On the other hand, because of strong non-uniform electric field around an anode wire, the spatial dimensions of the zone where chemical radicals, associated with the glow discharge processes are generated, is small and, according to our evaluation, does not exceed several tens of microns.

That is why it is important to find experimental evidence that the negative corona discharge can generate a considerable amount of chemical products usually associated with the glow discharge, which is enough to carry out effective etching of silicon and tungsten compounds in a proportional counter. If it is so, then one can use the principles of traditional plasma chemistry of a glow discharge (low pressure, RF) to predict the plasma chemistry of a corona discharge in the wire chambers (at 1 atm, DC).

5. Recovery of the aged anode wires

The wire etching is a rather complex chemical process. To obtain a general picture of the wire etching, it is necessary to identify the dominant processes occurring in the gas phase and at the gas/surface interface, resulting in formation of active chemical species (radicals, ions, *etc*.). The avalanche environment is plasma of ions and neutral radicals, and thus the wire etching process should be studied in the framework of the plasma chemistry. The intensity of ion and radical production depends on pressure, power density, detector irradiation rate, electric field strength, gas gain, materials of electrodes, gas composition including the presence of *ppm*-level impurities, *etc*.

5.1. Choice of the gas mixture

The discretion whether the etching or the yield of deposits will occur in CF_4 depends on plasma properties, although the F/C ratio model predicts that an effective etching gas mixture has the ratio of fluorine (F) to carbon (C) atoms in the range of $0.8 < F/C < 4.0$, and strong etching takes place at $F/C = 4$ [11]. On the other hand, the etching ability of tungsten compounds is more effective in CF_4/O reactive etching plasma [7–9]. To prevent the damage of carbon coating on the straw (cathode) wall during the recovery treatment, the oxygen in the etching gas mixture was replaced by CO_2. The needed oxygen radicals were mostly generated due to dissociation of CO_2 in collisions with the avalanche electrons near the wire. To optimize the recovery processes, the following gas mixture was chosen: 80 % CF_4 + 20 % CO_2 with the ratio $F/C = 3.2$ [15].

5.2. Etching process

The glow discharges media used in the plasma processing are partially ionized gases containing ions, electrons and neutral species in both ground and excited states. The degree of ionization is small, typically about 10^{-5} of all species, but the degree of dissociation can be quite large, sometimes exceeding 10^{-1} of all the species. Because of their higher concentration, neutrals (radicals) are the primary chemical species responsible for deposition and etching processes.

Due to a significant difference in mobility between the ions and electrons, the surfaces in contact with plasma generally acquire negative potential with respect to the plasma. As a result, positive ions are accelerated to the surface, and they can have a synergistic effect on the etching chemistry. This process is distinctly different in a wire chamber operating under atmospheric pressure, where the ionized gas contains electrons with a moderate energy of 5–10 eV, low-energy negative ions < 1 eV, and near-thermal positive ions [11].

To etch the tungsten or silicon compounds in a glow discharge (DC, RF-plasma), a negative potential was applied to the substrate that was in electric contact with the wafer. The etching process was carried out at a normalized electric field of 10–50 V/cm · Torr. The molecular dissociation leading to neutral radicals can be attributed to electrons with the energy in the range of 4−6 eV.

In a wire chamber (with a corona discharge, at 1 atm), the normalized electric field in vicinity of the wire surface is about 300−400 V/cm · Torr, which is enough to accelerate electrons up to the energy 5−10 eV. This energy is sufficient to break chemical bonds of the gas molecules and to start both molecular dissociation and other processes associated with the etching processes in a low-pressure glow discharge.

The mechanism of the etching process development can be considered to have four sequential steps:
- generation of active radicals $F^\bullet$, $O^\bullet$, $CF_3^\bullet$ in the gas discharge;
- their penetration through the wire gold coating;
- chemical interaction between the absorbed radicals and the wire materials leading to formation of tungsten compounds and their deposition on the wire surface;
- chemical interaction between the absorbed radicals and tungsten compounds leading to formation of volatile components and their desorption from the wire.
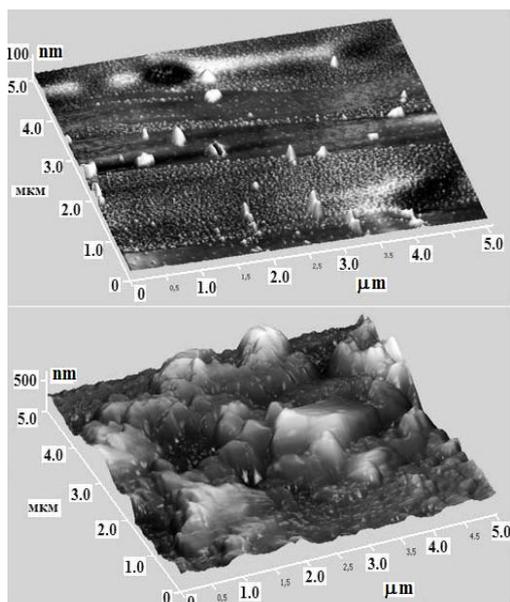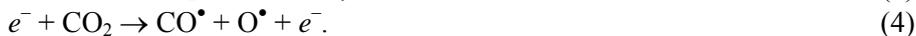
Fig. 2. Scanning Force Microscopy (SFM, solvent P47, cantilever HA-NC) images of both the non-irradiated wire surface (top) and the aged wire surface after irradiation (bottom)
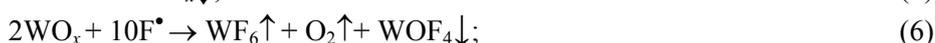
To make the corona discharge recovery processes more stable, the damaged zone of the wire was irradiated with a low intensity 3.5 kHz ^{55}Fe X-ray source. Photons effectively stabilize the ionized plasma, supporting the etching conditions and breaking chemical bonds of the compounds coating the wire.

The wire surface in the centre of the irradiated zone is the main source of ionizing electrons because it is covered with irregular spikes of 100–400 nm height with the radii smaller than 1 μm, Fig. 2. The electric field on the tops of the spikes can be estimated as $E_{max} \approx 2U / r \cdot \ln(2R/r)$, where $r \sim 0.5$ μm is the spike radius, $R = 2000$ μm is the straw radius, and $U \approx 2700$ V is the applied high voltage. As it follows from this formula, the electric field on the wire surface is about $E \approx 2.5 \times 10^5$ V/cm, and at least two orders of magnitude higher on the top of a spike, $E \sim 10^7$ V/cm. Therefore, a layer of tungsten oxides can be an additional source of electron current due to high field emission. Of course, such a wire surface damage stimulates micro-discharges and fast rising up of the corona discharge current, which results in production of radicals and ions in the vicinity of the wire surface.

The electrons formed in the ionized gas move in an intense electric field and obtain sufficient energy to break chemical bonds of the gas molecules. Thus, due to electron impact dissociation of CO_2 (the dissociation energy is $E_d = 5.5$ eV) and CF_4 around the anode wire, oxygen ions and radicals are produced, and many different active species, as well:

$$e^- + CF_4 \rightarrow CF_3^- + F^\bullet; \tag{1}$$
$$e^- + CF_4 \rightarrow CF_3^\bullet + F^\bullet + e^-; \tag{2}$$
$$e^- + CF_4 \rightarrow CF_2^{\bullet\bullet} + 2F^\bullet + e^-; \tag{3}$$
$$e^- + CO_2 \rightarrow CO^\bullet + O^\bullet + e^-. \tag{4}$$

The reactive gas fragments are transported in the electric field to the wire surface where they can be absorbed. The etching refers to a complex set of sequent chemical processes in which the gas-phase species interact with the tungsten-oxide compounds, which are placed both inside of the gold coating cracks and over the wire surface, the volatile products (↑) being evacuated through the gas. The most important plasma-chemical reactions for our gas mixture and their corresponding active radicals are the following:

$$W + O^\bullet \rightarrow WO_x \downarrow; \tag{5}$$
$$2WO_x + 10F^\bullet \rightarrow WF_6\uparrow + O_2\uparrow + WOF_4\downarrow; \tag{6}$$
$$2WOF_4 \rightarrow WO_2F_2\downarrow + WF_6\uparrow; \tag{7}$$
$$3WO_2F_2 \rightarrow WF_6\uparrow + 2O_2\uparrow + 2WO\downarrow; \tag{8}$$
$$WO \rightarrow W + O^\bullet; \tag{9}$$
$$W + 6F^\bullet \rightarrow WF_6\uparrow. \tag{10}$$

The average energy of positive ions in the gas discharge is almost thermal due to multiple elastic collisions with surrounding atoms and molecules. In contrast to electrons, ions do not store the energy obtained in the electric field: it is lost in each collision. The optimal etching conditions are fulfilled mainly in the peaks of the tungsten oxide compound where the electric field is high enough.

5.3. Choice of the working point for the negative corona discharge treatment

As it was mentioned above, a corona gas discharge occurs in high non-uniform electric fields surrounding anode wires. The tungsten-oxide deposits, which are placed both on the wire surface and inside of the cracks of the gold layer (see Fig. 2), will stimulate fast rising up of the corona discharge current because of their sharp shapes. Just in these points, chemical radicals generation associated with glow discharge processes becomes maximal, which results in intensive plasma-chemical etching of the tungsten-oxide peaks. As a result, the current of corona discharges falls down in time. That is why we performed the high voltage regulation every 30–40 min to compensate corona current decreases from 5 to about 1 μA.

In order to achieve the maximum etching rate, it was necessary to increase the current of corona discharges as high, as possible. This forced us to use a negative corona discharge because it has the following advantages in comparison to a positive corona discharge:

- this discharge is more stable and, consequently, it can generate a higher current;
- the mobility of negative ions is only half of that of positive ions.

Usually, the corona discharge in a straw manifests itself as a sharp current increase from 20–50 nA at the HV = –2500 V to 4–6 μA at the HV = –2650 V. The last potential was taken as the working point in the beginning of the recovery procedure.

5.4. Experimental results of recovery of aged wires

The progress of the wire recovery in terms of the gas gain along the straw is shown in Fig. 3a, b. Since the ^{55}Fe source spectrum has a sufficiently narrow peak in the 80 % CF_4 + 20 % CO_2 gas mixture, it was used to monitor the gas gain during the recovery process. The efficiency of the wire recovery procedure is presented in Fig. 3a. Such measurements were carried out every two hours. The gas gain distribution measured with the regular working gas mixture (60 % Ar + 30 % CO_2 + 10 % CF_4) before and after the recovery procedure is shown in Fig. 3b. As one can see, after six hours of the negative corona discharge treatment, the gas gain along the wire becomes the same as it was before irradiation.

Figure 4 shows results of SEM/XEM examinations of a restored anode wire surface in the centre of the irradiated zone in comparison with a non-irradiated wire surface. The total accumulated charge on a wire was 3 C/cm.

These results lead us to the conclusion that the proposed wire recovering procedure is very promising. The following processes are associated with the etching occurring after application of this procedure:

- the etched wire surface in the centre of the irradiated zone looks smooth and without any traces of deposits (tungsten-oxides compounds);
- the cracks formed by tungsten-oxides compounds in the gold layer (Fig. 1) have tightened. It means that etching of tungsten-oxides compounds occurs not only on the wire surface but also inside of the cracks and underneath the gold layer, too;
- the swollen wire diameter has decreased from 53 μm to the nominal value of 50 μm.
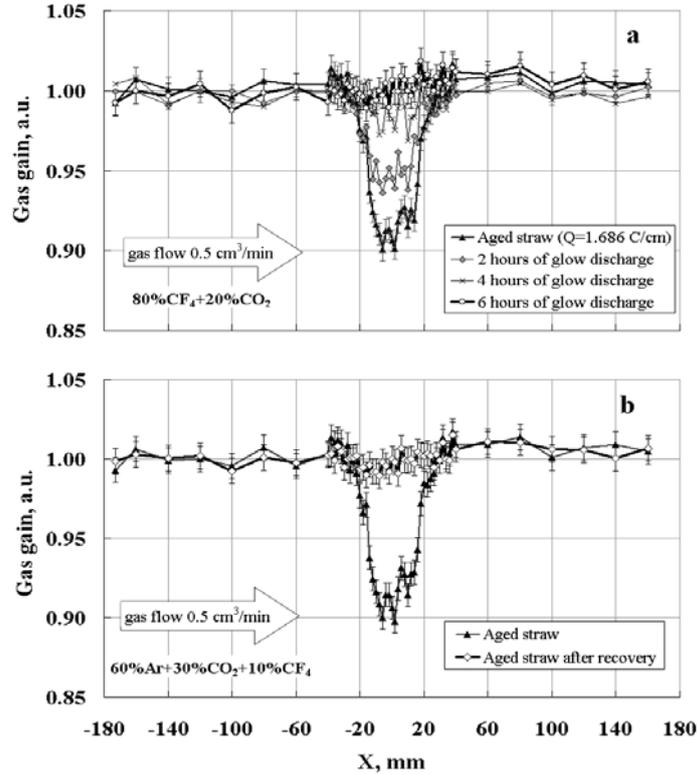
Fig. 3. a – gas gain behaviour along the straw during application of the wire recovering procedure. These measurements were carried out every two hours; 80 % CF_4 + 20 % CO_2 gas mixture, negative corona discharge; b – gas gain distribution along the straw before and after application of the wire recovering procedure; 60 % Ar + 30 % CO_2 + 10 % CF_4 working gas mixture
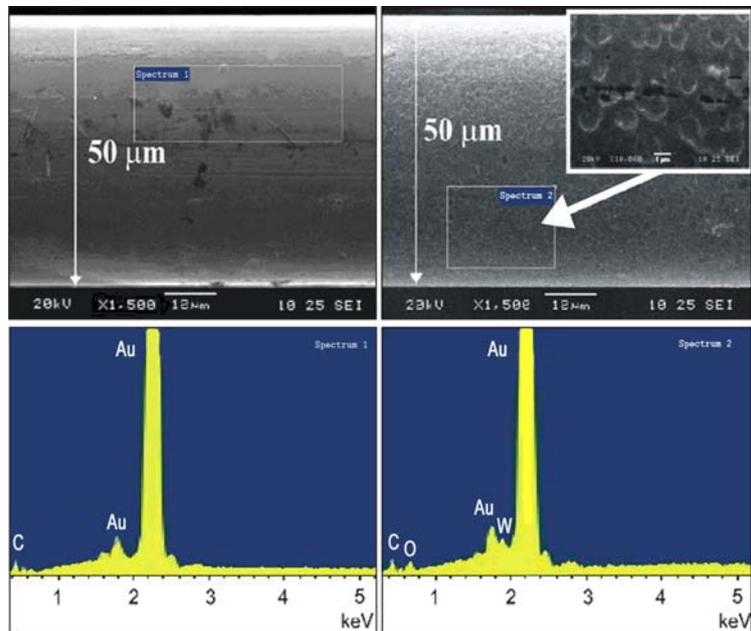

Fig. 4. SEM micrograph and the corresponding XEM spectra of the non-irradiated part of an anode wire surface (left) and in the centre of the irradiated zone of the wire after applying of recovery procedures (right). Both XEM analysis areas are denoted at the SEM micrograph by rectangles

388

6. Multiple recovery of aged anode wires

In order to confirm both the reliability and the reproducibility of the wire-recovering processes, multiple recoveries of the anode wires were performed. Our aim was to realize several cycles of an "aging-recovery" sequence during the continuous session of measurements.

The wire aging was carried out with a 60 % Ar + 30 % CO_2 + 10 % CF_4 gas mixture, and the recovery procedure was performed with an 80 % CF_4 + 20 % CO_2 mixture.

Two "aging-recovery" runs were performed. In the first run, the degradation of the gas gain in each cycle was 3 %, and in the second run in each cycle it was 6 %. During the first run, four cycles of the "aging-recovery" session were carried out, and during the second run three cycles were done. The total charge accumulated in each run was 3 C per 1 cm of the wire length.

The obtained data clearly demonstrate the efficiency of the proposed wire recovery method, see Fig. 5. As one can see, the application of a negative corona discharge to aged wires allows us to restore initial characteristics of a wire chamber several times. In other words, the lifetime of a straw detector can be increased by a few times. It is especially important when the wire detector is intensively irradiated with the irradiation current of about 1 μA/cm.
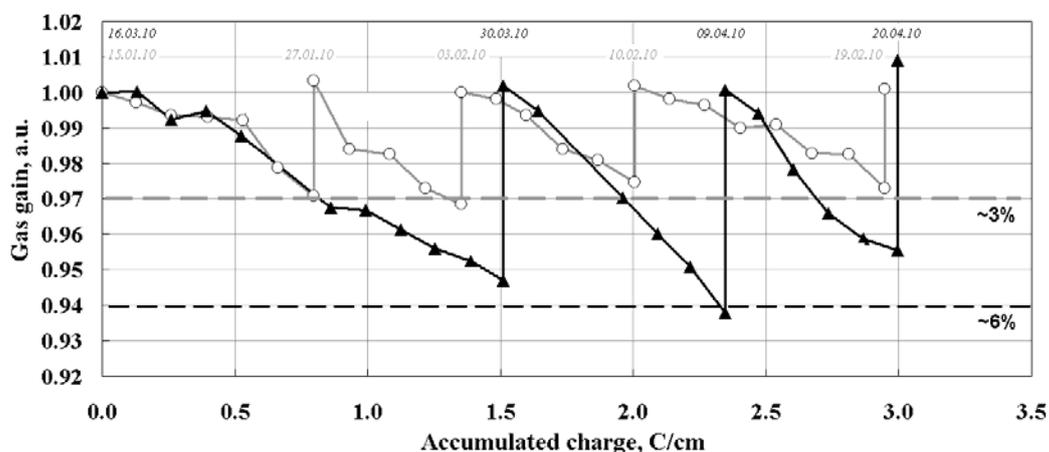

Fig. 5. Relative gas gain in the irradiated zone *vs* accumulated charge per unit of the wire length. The grey curve corresponds to the "aging-recovery" session with about 3 % of the maximum amplitude drop. The black curve corresponds to the "aging-recovery" session with about 6 % of the maximum amplitude drop due to wire swelling

Results of SEM examinations of anode wire surfaces in the centre of the irradiated zone after four cycles of "aging-recovery" session are shown in Fig. 6. As one can see, the wire surface is almost smooth and practically undamaged. Only some traces of WO_x compounds were found on the wire surface. This result looks almost similar to that of once-recovered wire, see Fig. 4. The wire diameter has decreased to the nominal value of 50 μm.
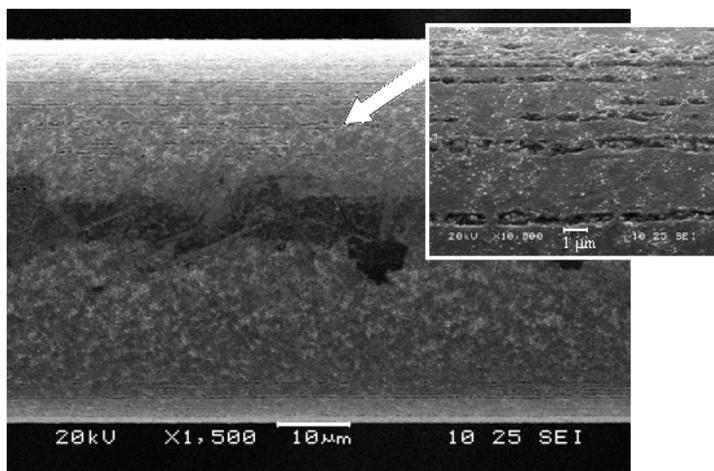

Fig. 6. SEM micrograph of the wire surface after applying of four cycles of the wire recovering procedure (see Fig. 5). The "aging-recovery" session with about 3 % of the maximum amplitude drop. The total accumulated charge was about 3 C/cm

7. Conclusion and outlook

1. A method for recovery of swollen anode wires in proportional counters by using a negative corona discharge treatment (with the current density about 3 μA per cm of the wire length) in 80 % CF_4 + 20 % CO_2 gas mixture has been proposed, successfully developed and tested. This method can remove from the surface of anode wires tungsten containing deposits which are accumulated there due to swelling effects.

2. Using this method, we have been able to recover a swollen wire multiple times, extending significantly the detectors lifetime. The proposed recovery mechanism is running "softly" and reliably.

3. We suppose that the application of the proposed method is more effective at the beginning of the detector degradation, when the gas gain drop does not exceed several percent (up to 9 %), and the total accumulated charge is smaller than 2 C/cm. For more aged wires, the wire degradation process becomes irreversible because of a high risk of formation of blisters and even ripping off fragments of the gold coating from the wire surface.

4. All the mentioned above experimental results allow us to conclude that the negative corona discharge can generate a considerable amount of chemical products usually associated with the glow discharge, which permit to carry out an effective etching of tungsten compounds in a proportional counter. This means that the principles of the traditional plasma chemistry of the glow discharge (low pressure, RF) can be used to explore the plasma chemistry of the corona discharge in wire chambers (1 atm, DC).

References

1. M. Hohlmann *et al*., Nucl. Instr. Meth. Phys. Res. A **494**, 179 (2002).
2. T. Ferguson *et al*., Nucl. Instr. and Meth. Phys. Res. A **488**, 240 (2002).
3. T. Ferguson *et al*., Nucl. Instr. and Meth. Phys. Res. A **515**, 266 (2003).
4. D.A. Aksenov, G.E. Gavrilov, A.G. Krivchitch, D.A. Maysuzenko, A.A. Fetisov, Preprint PNPI-**2830**, Gatchina (2010).
5. R. Openshaw *et al*., Nucl. Instr. Meth. Phys. Res. A **307**, 298 (1991).
6. S. Belostotski *et al*., Nucl. Instr. Meth. Phys. Res. A **591**, 353 (2008).
7. I.C. Plumb, K.R. Ryan, A Model of the Chemical Processes Occurring in CF4/O2 Discharges Used in Plasma Etching, Plasma Chem. and Plasma Process. **3**, 6 (1986).
8. R. d'Agostino, F. Fracassi, R. Lamendola, The Chemistry of Etching and Depositing Processes, Pure&Appl. Chem. **66**, 1185 (1994).
9. T.D. Bestwick, G.S. Oehrlein, Tungsten Etching Mechanisms in CF4/O2 Reactive Ion Etching Plasmas, J. Appl. Phys. **66**, 10 (15 November 1989).
10. J. Va'vra, Nucl. Instr. Meth. A **252**, 547 (1986).
11. J. Wise, J.A. Kadyk, D.W. Hess, M.C. Williams, IEEE Trans. Nucl. Sci., NS-**37**, 470 (1990); J. Wise, Vs Thesis, LBL-**29033**, University of California, Berkeley (1990).
12. M.E. Fraser, D.A. Fee and R.S. Sheinson, Plasma Chem. and Plasma Process. **5**, 163 (1985).
13. D.E. Tevault, Plasma Chem. and Plasma Process. **7**, 231 (1987).
14. S. Kanazawa, M. Kogoma, T. Moriwaki and S. Okazaki, J. Phys. D **1**, 838 (1988).
15. D.A. Aksenov, Yu. Dikarev, V.M. Vakhtel, G.E. Gavrilov, A.G. Krivchitch, D.A. Maysuzenko, A.A. Fetisov, Preprint PNPI-**2842**, Gatchina (2010).

UF/PNPI HIGH VOLTAGE SYSTEM IN THE LHCb MUON DETECTOR

N.F. Bondar, S.V. Bondarev, N.B. Isaev, O.E. Maev, A.V. Mylnikova,
E.M. Orischin, L.O. Sergeev, S.S. Volkov

1. MUON detector in LHCb

The muon system [1], shown in Fig. 1, consists of five stations (M1–M5) of rectangular shape, placed along the beam axis. Each Muon Station is divided into four regions, R1 to R4 with the distance increasing from the beam axis. The full system comprises 12 pairs of triple GEMs (M1R1), 264 double-gap MultiWire Proportional Chambers (MWPC) in M1/R2–R4 and 1104 four-gap MWPCs in M2–M5.

All the muon stations, including the iron f lters, are separated into two halves called A(access)-side and C(cryogenic)-side, which can move on rails away from the beam pipe for maintenance and installation. For M2–M5 stations, two large support structures built from iron beams accommodate the suspensions for the four chamber support walls and have platforms for electronics racks (4 racks on each side) and a gas system (2 racks on a side). The cable chains provide unbreakable connections of all the cables, optic f bers and pipes with the movable sides of the detector. Special racks with patch panels are located near each side of the detector as terminals of the cable chains. Station M1 has an independent support structure.
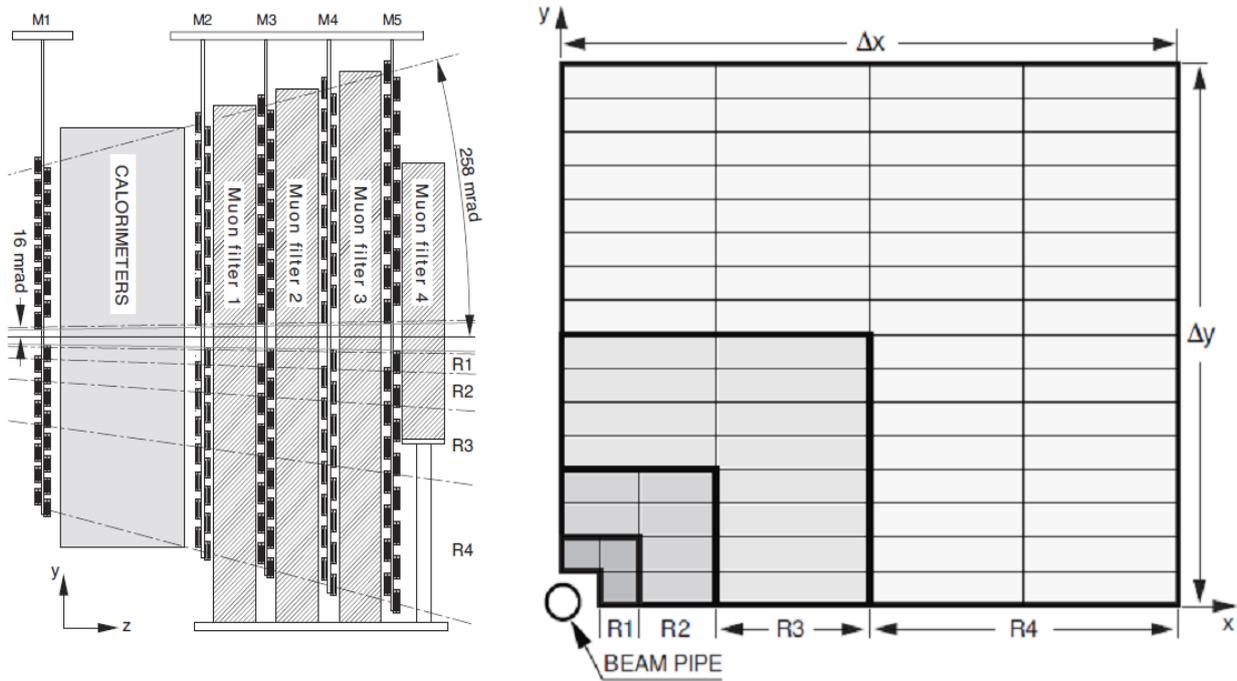

Fig. 1. Left – side view of the muon system. Right – front view of a quadrant of a muon station. Each rectangle represents one chamber, each station contains 276 chambers

2. Selection of a HV system

Due to great variations in technical requirements to HV parameters within the stations and regions in the MUON detector and taking into account the limited budget of LHCb, the choice of a HV system was a really big issue. Finally, the gas gain in MUON is now controlled by three independent HV systems: the INFN HV system was specially developed to control the gas gain in 72 HV channels of GEMs (M1R1), the CAEN system is serving R2–R4 regions in M1 and R1–R2 in M2–M5 – with 1104 channels, and the UF/PNPI HV system has been chosen for R3–R4 in M2–M5 with 3840 channels.

Initially, this multi-channel High Voltage Distribution and Monitoring System (HVDMS) was designed and produced by UF/PNPI collaboration for the End-cap Muon detector of the CMS project, and it met most of the LHCb requirements. To fit the LHCb chambers, special "LHCb-type" HV connectors were installed on the distribution boards [2]. A two stage configuration was selected for the LHCb muon detector.

The total number of HV channels is 3840. Taking into account the granularity of the HV system and the detector configuration we had to produce 4032 HV channels. To minimize initial price of the HV system, the production was divided into two stages. At Stage 1, all the chamber gaps of R3 are fed individually. Some of the gaps of the R4 chambers are connected in parallel in groups of four via the patch panels. The gaps connected in parallel always belong to different chambers to minimize losses of the efficiency. At Stage 2, all the chambers should be fed individually.

This solution allowed us to produce only half of the channels – 2016. Also, we have designed and produced a relatively cheap splitting device called "HV Patch Panel" (HV PP) for other 2016 channels.

At Stage 1, we produced:
- PCI card of the System Interface/Buffer (Host Card) – 6 modules plus 2 spares;
- 8-channel Master Distributor Board (MB) – 8 modules plus 2 spares;
- 36-channel radiation hard Remote Distributor Board (RDB) – 56 modules plus 10 spares;
- 320-channel HV Patch Panel – 8 units.

As a primary HV power supply, the Matsusada AU-5P60-LF was selected – 2 units plus 1 spare. Also, for a low voltage power supply, the WIENER type VEP 6021-LHC was selected – 1 unit.

For Stage 2, we had to produce additional 56 RDB modules and 8 MB modules to replace 8 units of the HV PP.

3. UF/PNPI HV layout in LHCb

The HV system layout is presented in Fig. 2. To follow the LHCb structure, the HV system is also divided into two independent parts, for the A-side and C-side. Each part has a complete set of equipment: a computer with 3 host cards, a Primary HV power supply and an individual crate with 4 Master Distributor boards. The low voltage power supply has 5 output channels. It allows to feed independently Remote Distributors on each side with +/– 8 volt power and to supply all the Master Distributors with 12 volts.
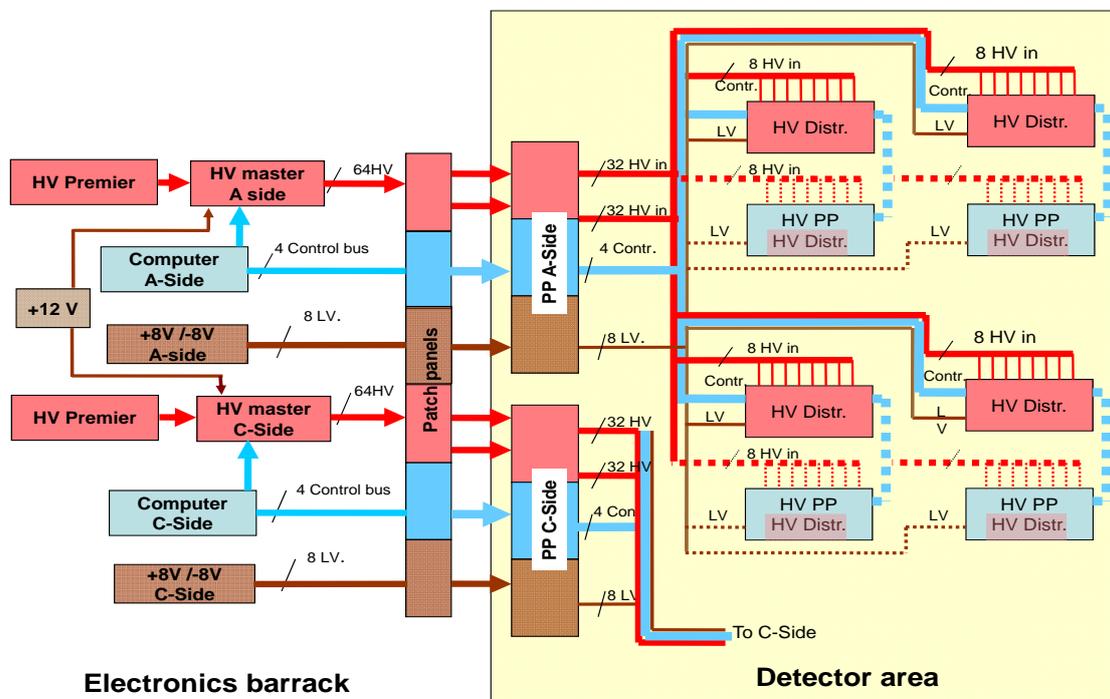

Fig. 2. UF/PNPI HV system layout of the LHCb muon detector. The remote distribution part is presented for the A-side

All the components including 2 computers, 2 Matsusada power supplies, 2 crates with 4 MB in each, and the low voltage WIENER power supply were assembled in one rack. The rack was installed in the electronics barrack away from the detector, so that it was always accessible even during the beam time. The cables for the low and high voltage, the signal cables for the final system layout were placed between the rack and two patch panels in the detector area. All the voltages and control signals were delivered from these patch panels to the Remote Distributors crates with flexible cables. The total length of the cables was more than 100 meters. The voltage drop and the signal cable skew was taken into account.

Since one control line can serve only up to 16 RDB modules, for the maximum number (56) of the RDB modules on each side we had to put 4 control lines per side. Currently, for Stage 1 we are using half of the RDB modules (28 at one side) and only 2 control lines per side.

In Fig. 2, the red boxes "HV Distr." are the crates with the RDB modules, and the blue boxes "HV PP/HV Distr." are the HV Patch Panels. These Panels have the same size as the RDB crate, so to implement Stage 2 we should replace these Patch panels with the RDB crates and reconnect some HV cables to chambers and rearrange the control lines. All the signal cables, the HV and power cables are now installed for the final version of the UF/PNPI HV system.

4. Improvement of the system parameters on the base of the operation experience

The first two years of operation were like a burn-in time for the system. There were quite a large number of failures that required a lot of attention, and changes to improve the system reliability and the precision of the specified and measured parameters.

First, it was found that the output voltage in some channels drifts, and biases in several channels were observed in both directions. Therefore, a procedure of calibration of the sensor output voltage was introduced to all channels directly in the detector. The reason for the voltage instability was low reliability of the 1 GigaOhm resistors in the HV divider circuits, which were used in each channel of the voltage stabilizer and also used as sensors of the output voltage. During a shutdown, these resistors were replaced by more reliable resistors in all the RDB and MB modules.

The second problem we faced in Stage 1 was a high level of the output current noise in some channels of the RDB and MB. Sometimes, this noise led to false alerts of the overcurrent protection circuit during ramping up of the output voltage, which impeded severely setting up of the system into the operation mode. The main reason of this excess noise was found to be some instability of the voltage regulators in these channels. The replacement of the 1GigaOhm resistors of the HV dividers improved the noise performance significantly. Also, we tuned the stabilizer parameters in all the RDB channels. Finally, we have reached the resolution of the current sensors for all the RDBs better than one ADC step.

The voltage regulator of the MB has four FETs connected in series. This solution allows to make a 4 kV stabilizer using 1.0 kV transistors. Unfortunately, this circuit is not very stable, in particular, during ramping up the output voltage. By selecting parameters of the transistors, we were able to assemble quite stable voltage regulators for the MB. Unfortunately, these regulators tend to aging, their stability being decreased. Now, there is a new commercially available transistor with the working voltage of 1.5 kV. We have designed a new version of the MB regulator specified for 3 kV with 2 transistors. This regulator is simpler and more stable, and can be used for the LHCb muon chambers since the HV in these chambers is lower than 2.8 kV.

There is a proposal to improve the temperature stability of the current sensors up to 1.5 nA/10 °C. This modification will be implemented in new modules.

One channel of the MB can supply up to 36 gas gaps through the RDB. In the case of a short circuit in any gap or in an RDB channel, all the 36 outputs will be tripped. To keep the maximum efficiency of the muon detector, a special remotely disconnecting fuse is installed in the output of every RDB channel. It allows to disconnect a failed channel during the beam time, when the LHCb cavern is closed for access. Because of large cable lengths and small wire cross sections, this procedure was not reliable enough. To improve it, we have increased the burning voltage up to 60 V.

According to the LHCb specifications, the HV control system must be USB controllable. This work is in progress, a new control system will be implemented during the 2013 shutdown.

5. HV system performance

Since 2009, the HV system is working under option "Stage 1" [3]. The main task of the system is to keep the output voltage within the specified limits to provide a homogeneous and stable gas gain in MWPCs. The system has a very useful feature, which apparently is a great competitive advantage over most commercial HV-systems. It is the ability to control and monitor the precision of the output voltage censors and to recalibrate them if necessary. The procedure is as follows: we set the HV-transistors to the fully open state and measure the voltage set on the primary power supply with the RDB voltage sensors. To have this option precise, we need properly calibrated primary power supplies, which are always accessible, only two of them being in the system.

This procedure allows us to sustain the output voltage with the precision of +/− 5V (Fig. 3). The system has the current measurements resolution about 1 step of an ADC. The average quantity of faulty channels per year is less than 5 out of 2000. The average quantity of disconnected channels is about 3 per year.
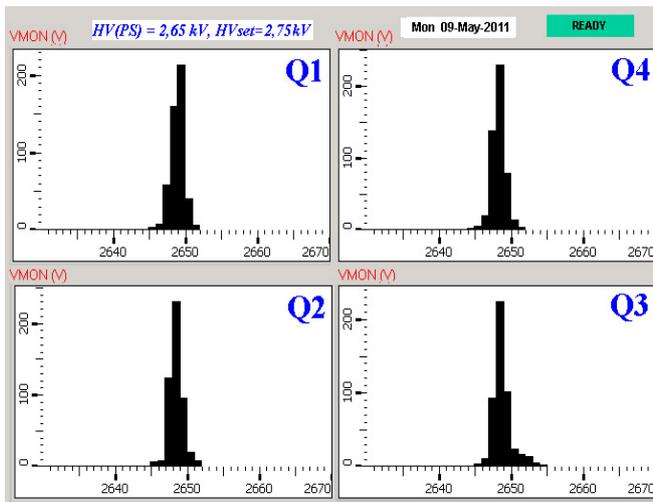
Fig. 3. Typical distribution of the measured voltages at the RDB outputs

After the period of 3 year maintenance and modifications described above, the HV system behaves very stable and reliable. Stage 2 is in progress, and the complete system must be commissioned and put into operation after the long shutdown in 2013–2014.

References

1. The LHCb Detector at the LHC/ LHCb Collaboration 2008, J. Instrum. **3** (2008).
2. S.V. Bondarev, N.B. Isaev, V.I. Lazarev, A.V. Mylnikova, L.O. Sergeev, S.S. Volkov, Multi-Chanel High Voltage Distribution and Monitoring System for LHCb Muon Chambers in *PNPI High Energy Physics Division, Main Scientific Activities 2002−2006*, Gatchina, 2007, p. 335.
3. A.A. Vorobyev *et al*., Experiment LHCb at the LHC, this issue.

CROS-3B – COORDINATE READOUT SYSTEM (NEW DRIFT CHAMBER VERSION)

V.L. Golovtsov, E.M. Spiridenkov, L.N. Uvarov, S.L. Uvarov, V.I. Yatsura

The Radio Electronics Laboratory of the High Energy Physics Division of PNPI continues developing a series of Coordinate ReadOut Systems – the so called CROS-3 series, which was first described in [1] and consists of 3 types of cards: Digitizer, Concentrator and System Buffer. Here we present the CROS-3B version targeted for instrumentation of large-size Drift Chambers (DCs) built at PNPI and designed for using as a tracking detector of the magnetic forward spectrometer for the BGO-OD experiment [2] at the Electron Stretcher Accelerator (ELSA) [3] facility at the Physics Institute of the University of Bonn, Germany.

The CROS-3B retains common features of the CROS-3 series.

- The CROS-3 basic setup consists (see Fig. 1) of 3 types of cards: System Buffer, Concentrator and Digitizer. The cards make use of high-speed serial 2.0 Gb/s fiber and 100 Mb/s copper links to transfer control, trigger and readout data. The cards functionality is based on a firmware loaded into FPGAs.
- The System Buffer provides interfaces to the host computer and trigger logic.
- The Concentrator collects event fragments from the Digitizers in parallel, builds an event and sends it to the System Buffer.
- The Digitizer amplifies, discriminates and continuously digitizes input signals, stores data in the digital pipeline for the trigger decision time and encodes arrival time and positions of hits in a programmable readout gate upon receiving a trigger.
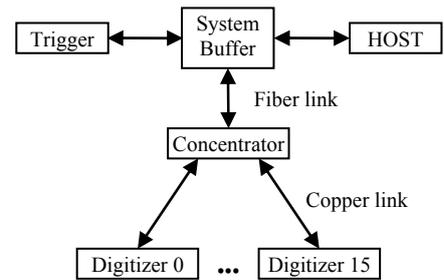

Fig. 1. CROS-3 basic setup

There are new features, specific only to the CROS-3B version. The amplifier input impedance and integration constant are optimized to get the best possible time resolution for large-size DCs with a rather big wire capacitance. The system setup is extended by adding a Low-Level Concentrator. So, the System Buffer is now able to control and collect data from up to 4096 channels, 16 times more channels than before. The-built-in error detection logic allows to terminate gracefully the readout process in case of hardware failures.

1. Drift chambers

PNPI has designed and built 8 DCs for the BGO-OD experiment. The DCs will be used for tracking of charged particles behind a spectrometer magnet. They are grouped into 2 stations. Each station consists of 4 (X, Y, U, and V) DCs with sensitive areas of approximately 1.2×2.4 m^2, 1.3×2.4 m^2, 1.8×2.7 m^2, and 1.8×2.7 m^2. All chambers feature similar design and contain a double layer of hexagonal drift cells as shown in Fig. 2, where black dots are sense (anode) wires and white dots are field (cathode)

Fig. 2. Drift Chamber cell structure, sense wires are shown as black dots, and field wires – as white dots

wires. Sense wires are spaced at 17 mm, so the maximum drift distance for tracks perpendicular to the chamber plane (vertical tracks in Fig. 2) is about 8.5 mm. The chambers operate with the standard 70/30 Ar/CO$_2$ gas mixture. The high voltage of $-(2.9 \div 3.2)$ kV is applied to cathode wires, anode wires being at 0 V for the signal readout.
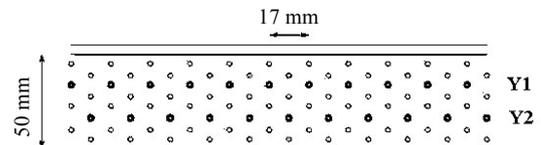
The X, Y, U, and V chambers have 160, 288, 320, and 320 sense wires correspondingly, totaling to 2176 sense wires for the entire system of two stations. The space resolution requirement for the experiment is 300 µm, the trigger rate being about 1 kHz.

2. Amplifier optimization

The basic amplifier structure shown in Fig. 3 was used as a starting point for optimization. The structure features 3 independent, but equal, RC circuits that integrate the input current signal I. The first transimpedance amplifier stage K_R is implemented as a common base transistor with low input noise. The amplifier input impedance (including a protection circuit) and the sense wire impedance are well matched.

The second stage K_V is a voltage amplifier with the 500 MHz bandwidth. *D* stands for a differential discriminator with a threshold voltage TH applied to its positive input and an amplified and integrated input signal to its negative input. The goal of the optimization was to choose the RC time constant that would result in the best time/space resolution for the given cell geometry.
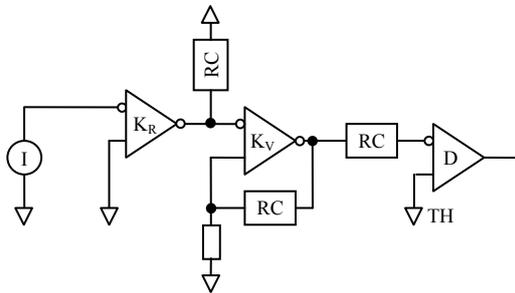

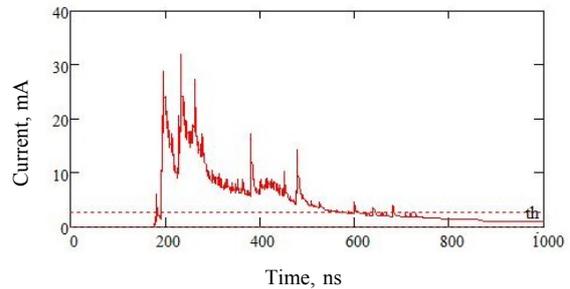
Fig. 3. Basic amplifier structure

Fig. 4. Drift chamber anode current produced by a track

The DC model used assumes each primary electron in the track is independently amplified by a random factor distributed exponentially [4]. Figure 4 shows an example of the anode current produced by a charged particle which traversed the drift cell perpendicular to the chamber plane. The tracks were generated using HEED [5], a program that computes in detail the energy loss of fast charged particles in gases. The simulated tracks in turn were used in GARFIELD [6] to calculate drift times of electrons or, in other words, the arrival time of amplifier input signals.
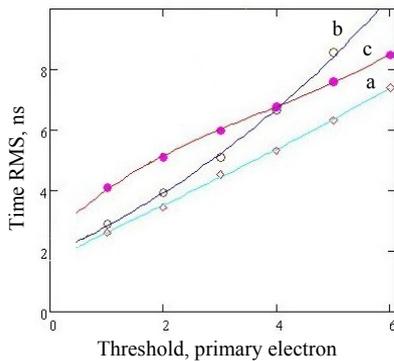

Fig. 5. Calculated DC time resolution for the amplifier with: the response as a step function (curve a); 2 ns time constant (curve b); 10 ns time constant (curve c)
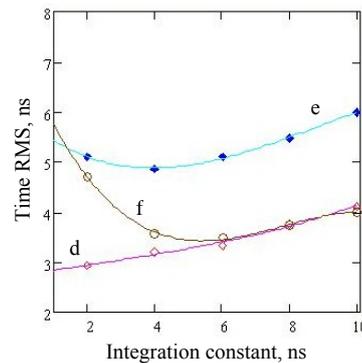

Fig. 6. Calculated DC time resolution at the threshold set to: 1 primary electron (curve d); 3 primary electrons (curve e); 5σ (curve f), where σ – noise standard deviation

Figure 5 demonstrates the calculated DC time resolution as a function of the threshold for 3 different ways of processing the anode signal. Ideally, an amplifier with the response as a step function for each primary electron (curve a) gives the best time resolution, which can be called an intrinsic DC resolution. 2 other curves are for the basic amplifier structure with 3 independent integration circuits. The time constant of each circuit is either 2 ns (curve b) or 10 ns (curve c). The smaller time constant is preferred for lower thresholds, while for thresholds above 4 primary electrons the bigger time constant yields better resolution.

The calculated DC time resolution as a function of the integration constant for different threshold settings is presented in Fig. 6. There is almost a linear dependence for 1 primary electron threshold (curve d). At the threshold of 3 primary electrons the best resolution is achieved with the integration constant of 4 ns (curve e). However, both curves do not take into account the input noise of the amplifier. If it is taken into account, the dependence has a distinct minimum at 6 ns for the threshold equal to 5 standard deviations of the input noise (curve f). So, the integration time constant of 6 ns was chosen.

Figure 7 demonstrates the calculated DC space resolution as a function of the track distance from an anode wire at the threshold set to 1 primary electron for an amplifier with the response as a step function (curve g) and for the implemented amplifier (curve h). The space resolution in the second case is only slightly worse than in the first one. The average space resolution is better than the required 300 μm.

Fig. 7. Calculated DC space resolution at the threshold set to 1 primary electron for: an amplifier with the response as a step function (curve g); the implemented amplifier (curve h)

3. CROS-3 extended setup

An evaluation of the data payload for copper and fiber data links under the expected occupancy and the trigger rate for the BGO-OD experiment revealed a possibility of merging more data into a single data stream by implementing a setup with 2 Concentrator levels.

A newly developed CROS-3 extended setup, shown in Fig. 8, consists of the same 3 types of cards: System Buffer, Concentrator and Digitizer, but there are two kinds of Concentrators. The regular Concentrator interfaces with the System Buffer over a fiber link as it does in the CROS-3 basic setup. But now, instead of Digitizers, it serves up to 16 Branches consisting of a Low-Level Concentrator with up to 16 Digitizers linked to it. 1 Branch serves an *X* DC, and 2 Branches serve *Y*, *U*, and *V* DCs, the total number of Branches being 14 for the entire system. Each Low-Level Concentrator interfaces with the upstream Concentrator over a copper link. Both Concentrators utilize the same printed circuit board. Though, the boards are differently stuffed and run under different firmwares. The CROS-3 extended setup retains the backward firmware and program compatibility with the CROS-3 basic setup, but serves up to 16 times more channels than before.

Fig. 8. CROS-3 extended setup

4. CROS-3B features

The CROS-3B version makes use of the extended setup and includes the following cards:
- CSB-B as the System Buffer, Fig. 9;
- CCB16-B as the Concentrator, Fig. 10;
- CCB10-B as the Low-Level Concentrator, Fig. 11;
- AD16-B as the Digitizer, Fig. 12.

The CSB-B complies with the PCI/PCI-X Local Bus Specifications and supports linear burst reads. The CCB10-B is a ten-port version of the sixteen-port CCB16-B card. The built-in error detection logic can be activated in the CSB-B, CCB16-B, and CCB10-B cards. It gracefully terminates the readout and reports the encountered problem(s) to the HOST in case of the hardware failure.

The AD16-B main features are:
- 16 input channels;
- an effective digitization frequency of 400 MHz or 2.5 ns per time bin;
- an 8-bit programmable threshold;
- an 8-bit programmable pipeline delay in 10 ns steps;
- an 8-bit programmable gate width with 2.5, 5, 10, or 20 ns programmable binning;
- 4 modes of operation with different output formats:
  - in the "Leading-Edge Raw" mode a 2-dimensional array (time bin #, channel #) of the leading edge transitions (hits) of the discriminator outputs is returned;
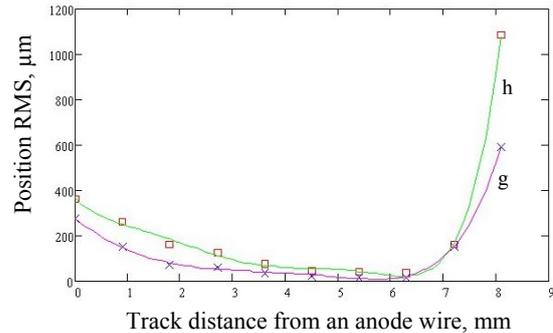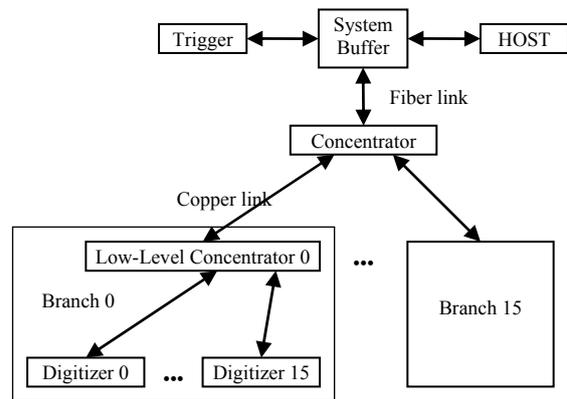
− in the "Leading-Edge Encoded" mode a list of encoded hits (time bin #, channel #) is returned;

− in the "Time-Over-Threshold" mode a 2-dimensional array (time bin #, channel #) of the discriminator outputs is returned;

− in the "Threshold Curve" mode a threshold scan is performed. For each channel at each step a sum of noise and test pulse hits is counted up, and an array of counter values is returned. The initial threshold, the threshold step and the number of generated test pulses (exposure window) are programmable.
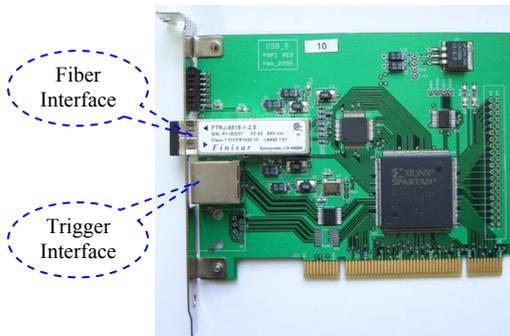

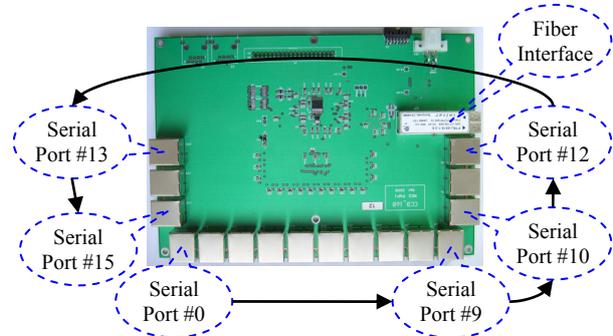**Fig. 9.** CSB-B – the CROS-3B System Buffer

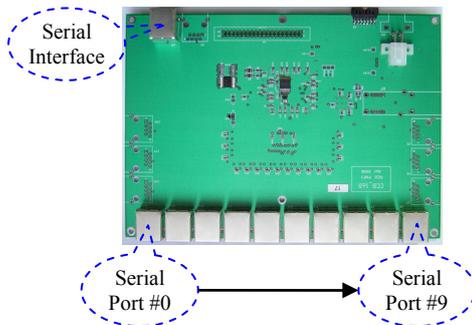**Fig. 10.** CCB16-B – the CROS-3B Concentrator

Fig. 11. CCB10-B – the CROS-3B Low-Level Concentrator

Fig. 12. AD16-B – the CROS-3B Digitizer

The CROS-3B command library provides an access to all CROS-3B registers. Examples of the system configuration and the data taking algorithms can be found in the CROS-3B Reference Guide [7]. A user is supposed to create his/her own code based on the above library and algorithms to effectively exploit all CROS-3B features.

References

1. N.F. Bondar, V.L. Golovtsov, A.G. Golyash, E.A. Lobachev, L.N. Uvarov, S.L. Uvarov, V.I. Yatsura, Third Generation Coordinate Readout System – CROS-3, *PNPI High Energy Physics Division, Main Scientific Activities 2002–2006*, Gatchina, p. 335.

2. http://bgo-od.physik.uni-bonn.de

3. http://www-elsa.physik.uni-bonn.de/elsa-facility_en.html

4. L. Kudin, V. Sedov, E. Spiridenkov, Electronics Noise and Time Resolution of the Multiwire Proportional Chamber, LHCb Note 99-039, MUON.

5. I.B. Smirnov, Modeling of Ionization Produced by Fast Charged Particles in Gases, Nucl. Instr. and Meth., A **554**, 474 (2005); the HEED Latest Developments Can Be Found at http://ismirnov.web.cern.ch/ismirnov/heed

6. R. Veenhof, GARFIELD, Recent Developments, Nucl. Instr. and Meth. A **419**, 726 (1998); the GARFIELD Latest Developments Can Be Found at http://garfield.web.cern.ch/garfield/

7. http://red.pnpi.spb.ru/~uvarov/BONN/CROS-3B.htm

CROS-3L – COORDINATE READOUT SYSTEM (LHCb TEST STAND VERSION)

V.L. Golovtsov, E.M. Spiridenkov, L.N. Uvarov, S.L. Uvarov, V.I. Yatsura

The design and development of the CROS-3 series is in the scope of interest of the LHCb Test Stand, which is constructed specially for tests of LHCb muon chambers [1]. We present a CROS-3L version, which has been designed and used for the LHCb Test Stand.

The block-diagram of the system is illustrated by Fig. 1 and includes:

- 4-channel front-end digitizer (ADF-L);
- 16-channel concentrator (CCB16);
- system buffer (CBS-B).

The analog part of the ADF-L is based on discrete elements performing chamber signal amplification and shaping, as well as pulse discrimination with peaking time 15 ns and operational threshold $\leq$ 15 fC. The digital part is implemented in a Xilinx Spartan-3 FPGA that performs both the time digitization and readout tasks. The delay range compensates trigger latency of up to 2.5 µs in 10 ns steps. The finest time bin resolution is 2.5 ns, the maximum number of time slices being 255. The amplitude digitization per each channel is performed by 10-bit ADC at a 100 MHz rate. The readout is performed over a STP CAT5 cable at a 100 Mb/s rate.

The CCB16 collects data from up to 16 digitizers into temporary buffers, which are read out to the CBS-B via an optical fiber at a 2.0 Gb/s. The CBS-B is implemented as a universal PCI card. The electronics modules of the system are illustrated by Figs. 2–4. Figure 5 shows the LHCb muon chamber equipped by CROS-3L electronics.
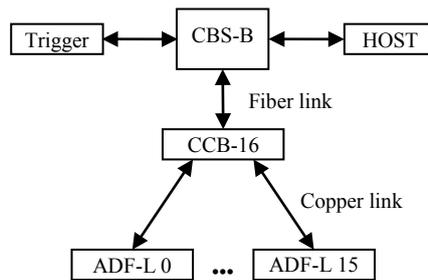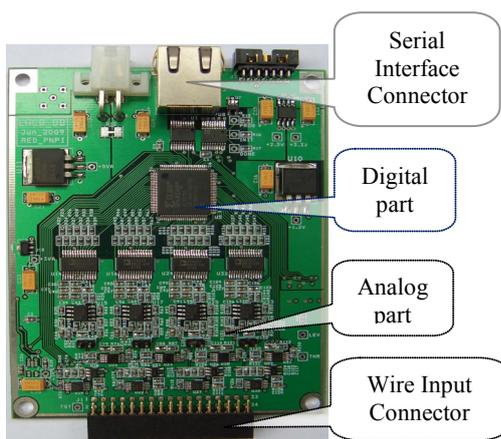

Fig. 1. CROS-3L set-up

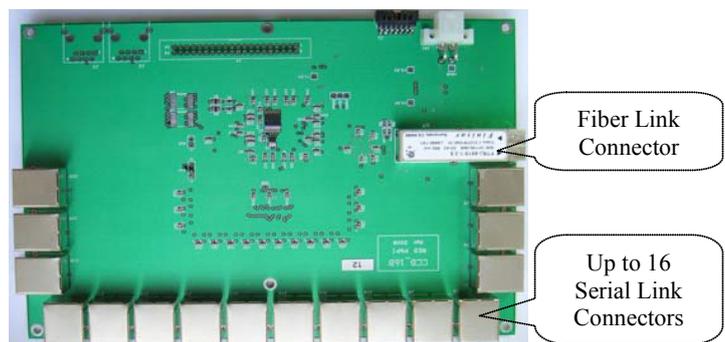**Fig. 2.** ADF-L digitizer module
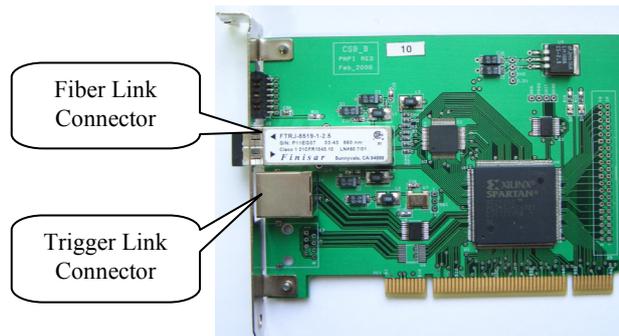

Fig. 3. CCB-16 concentrator module
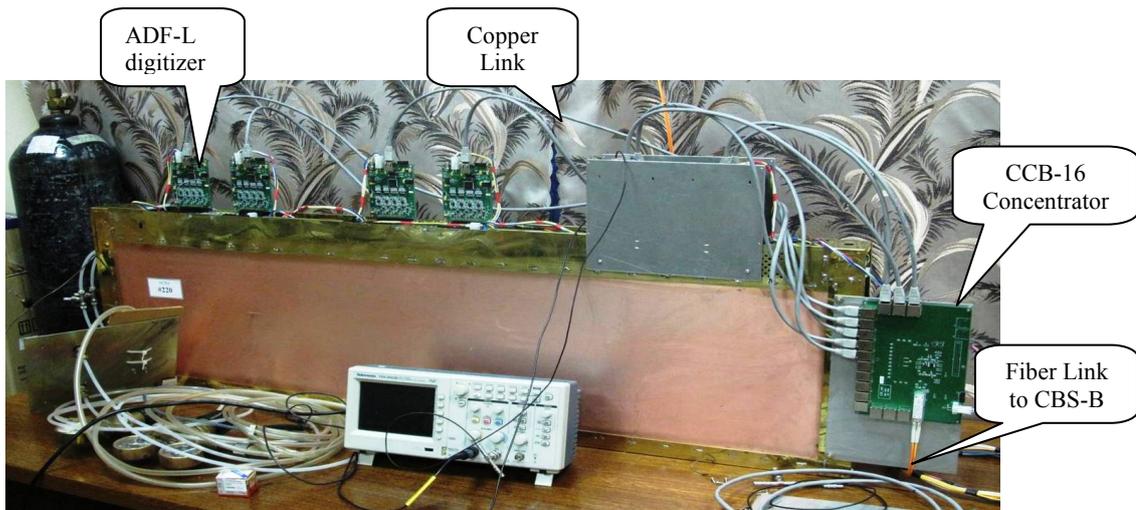
Fig. 4. CBS-B system buffer module

Fig. 5. LHCb muon chamber equipped by CROS-3L electronics at the Test Stand

The CROS-3L modules have the following features:
- the digitizers and the concentrator are mounted directly on the chamber;
- each digitizer amplifies, discriminates and pipelines input signals in parallel at a 100 MHz rate;
- when the system trigger occurs, the sparse encoding within the gate is started at a 400 MHz rate to collect data in parallel into a temporary buffer located in the digitizers;
- when the sparse encoding is over, the readout process is started over serial links at a 100 Mb/s rate to collect the sparse compacted data into a temporary buffer located in the concentrator;
- finally, the data are collected into the system buffer over the fiber link at a 2 Gb/s rate;
- fiber and copper links are used for the system trigger to be sent and the system constants such as the delay and gate values to be downloaded into the digitizer.

Reference

1. High Energy Physics Division, Main Scientific Activities 2002–2006, Gatchina (2007).

SCINTILLATION PROPERTIES OF BaF$_2$:Cd, BaF$_2$, BaF$_2$:Ce, BaF$_2$:Sc, BaF$_2$:Tm CRYSTALS AND CERAMICS; NEW PHOTOSENSORS FOR THE VACUUM ULTRAVIOLET REGION

Yu.I. Gusev, S.V. Kosyanenko, D.M. Seliverstov, V.M. Suvorov

1. Introduction

Research and development of new scintillation materials is mainly triggered by the growing needs of modern medical imaging, high energy and nuclear physics.

Pure BaF$_2$ crystals are widely applied as scintillation material because of its high density, high radiation resistance and good time resolution due to the fast component (< 1 ns) appearing in the emission bands around 220 and 195 nm. This fast component luminescence is called Auger-free luminescence or cross-luminescence, and it is attributed to the radiative recombination of the F-2p valence band electrons with the outmost holes of the Ba-5p core band.

However, in addition to the fast component, the BaF$_2$ crystal has a slow component at 300 nm with a decay time of about 700 ns, which causes deterioration of the time resolution at high counting rates. Suppression of the slow component is a crucial key when applying this crystal to high counting rate experiments in such fields as high energy physics and nuclear medicine.

This work is aimed to develop specimens of BaF$_2$-based crystals and ceramics doped with different elements in order to improve the light yield of the fast component and to suppress the slow part of the luminescence.

2. Experimental method

BaF$_2$ crystals were grown by the Stepanov – Stockbarger method, which provides high light transparency in the Vacuum UltraViolet (VUV) region. The optical transparency of our samples was measured with a SF-26 spectrophotometer in the wavelength range from 190 to 600 nm. We used an improved method of ceramics production from the BaF$_2$ powder with 40 to 60 nm nano particles by hot pressing in the CF$_4$ environment at a temperature of 1050 °C and under pressure of 200 MPa. The transparency of ceramics at 220 nm is only 11 % lower in comparison to that of single crystals, allowing to use them for measurements in the VUV region. However, such transmittance is insufficient for 20 mm length specimens and requires further improvements.

The luminescence spectra were measured under constant *X*-ray (40 kV) excitation. The registering equipment consisted of a MDR-2 monochromator and a FEU-106 photomultiplier. The obtained spectra were corrected for decreasing of the PMTs sensitivity in the wavelength range from 200 to 600 nm. In measurements of the luminescence kinetics, a pulsed *X*-ray (30 kV) source was used with the pulse duration shorter than 1 ns and a repetition rate of 12 kHz. The registering equipment was arranged according to the standard "start-stop" scheme, the time resolution of the system being better than 50 ps.

3. Results of measurements of optical properties of BaF$_2$ crystals and ceramics

3.1. Cd-doped BaF$_2$ crystals

The transmission curves within the range of 200–600 nm for pure BaF$_2$ and BaF$_2$:0.1%CdF$_2$ crystals are identical within the experimental error of 1 % (here and in the following, the percentage of the doped element is given in mol/%). In the case of ceramics, a slight decrease of the transparency in the UV range (200–300 nm) at a level of 3–5 % is observed. Increasing the Cd concentration to 0.3 % has virtually no effect on the sample transparency. The transparency of the BaF$_2$:0.1%CdF$_2$ sample is higher by 30 %, relative to that of the BaF$_2$ single crystal. A comparison of the total *X*-ray luminescence light yield for BaF$_2$:0.1%CdF$_2$ crystals and the corresponding ceramics shows that the light yield is 15 % higher in ceramics. A discovery of the strong dependence on the Cd concentration of the light yield in ceramics (clearly visible in Fig. 1) is a subject of interest. Changing the Cd concentration from 0.1 to 0.3 % in the

ceramics reduces the light yield by a factor of 5.4, while in the doped crystal it falls by a factor of 1.3 only. The optical parameters of the BaF_2:0.1%CdF_2 crystals and ceramics, which we determined for the first time, make these scintillators promising from the standpoint of obtaining high light yield for the fast component and reducing the intensity of the slow component relative to that of single BaF_2 crystals [1].
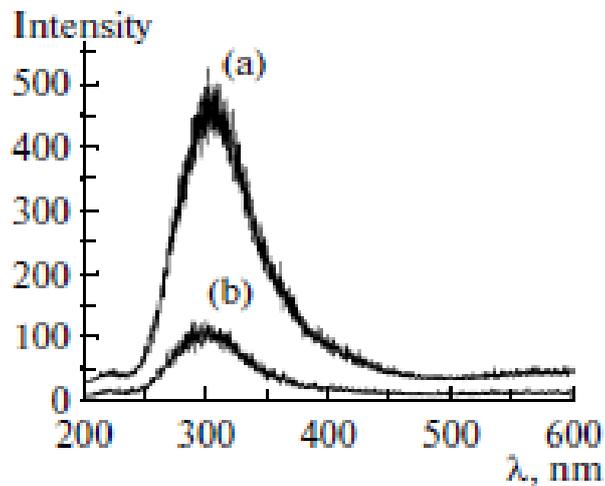

Fig. 1. Influence of Cd doping on the light yield of BaF_2:CdF_2 ceramics: a – 0.1%CdF_2; b – 0.3%CdF_2

3.2. BaF₂ single crystals and ceramics

A comparison of X-ray luminescence spectra for single BaF_2 crystals and ceramics shows an increase of the fast component yield in ceramics (as compared to BaF_2 single crystals) of about 12 % and a reduction of the slow component yield by a factor of 3.6 (Fig. 2a, b), which is observed for the first time. We suppose that the suppression of the slow component is caused by the non-irradiative annihilation of excitons on boundaries of nano particles in ceramics. Fitting the experimental data with two exponential decay curve $LY(t) = A_1 \exp(t/\tau_1) + A_2 \exp(t/\tau_2)$ gives $\tau_1 = 1.77 \pm 0.12$ ns and $\tau_2 = 493 \pm 6$ ns. A similar reduction of the time decay exciton component is observed in BaF_2 crystals doped with Cd [1, 2].
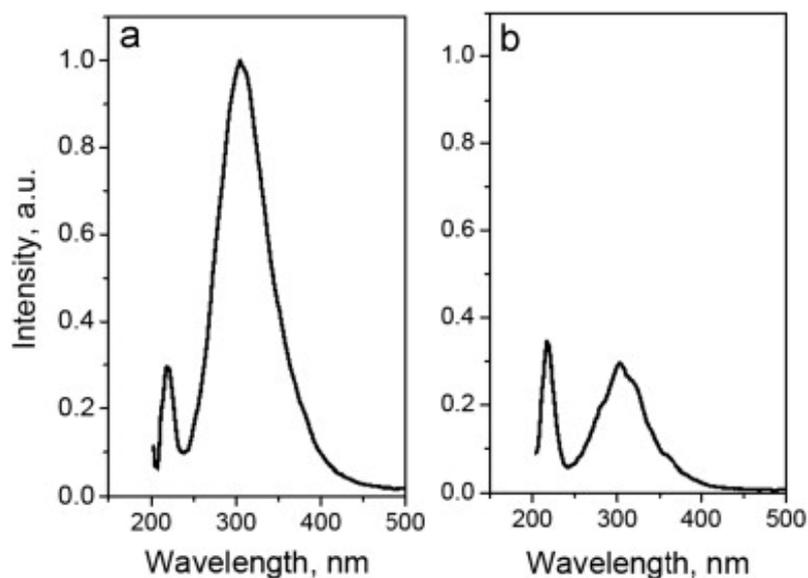

Fig. 2. X-ray luminescence spectra of a single BaF_2 crystal (a) and of ceramics (b)

402

3.3. Sc-doped BaF$_2$ single crystals and ceramics

BaF$_2$ single crystals and ceramics were doped with 0.5, 1.0 and 2.0 % Sc. The transparencies of $5 \times 10 \times 15$ mm^3 BaF$_2$:0.5%Sc and BaF$_2$:2.0%Sc crystals are close to that of single BaF$_2$ crystals with a slight absorption line at 290 nm. An increase of the Sc concentration from 0.5 to 2.0 % reduces the transparency at 220 nm by 8–10 %, which does not affect significantly other optical properties of the crystals. Doping the crystals with scandium (1%Sc, Fig. 3a, b) and annealing in CF$_4$ increase the relative light yield of the fast component by a factor 2.6, in comparison with that of single BaF$_2$ crystals.

Doping the BaF$_2$ crystals with scandium (1.0 and 2.0 %) does not change the decay time of the fast component ($\tau_1 = 2.0 \pm 0.5$ ns). The dependence of the light yield upon annealing in the CF$_4$ atmosphere of ceramics samples of dimensions $4 \times 4 \times 15$ mm^3 with the concentration 0.5 and 2.0 % of Sc was studied. Relative measurements showed an increase of the ratio of the fast to slow components yield by a factor from 1.7 to 2.5, as compared with single crystals [2].
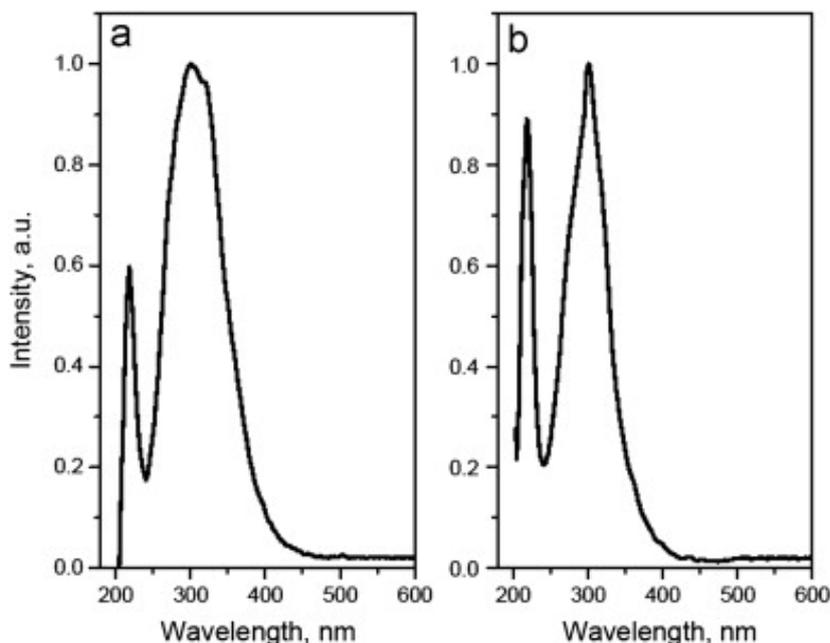

Fig. 3. Light yields of a single BaF$_2$ crystal without annealing in CF$_4$ (a) and of a BaF$_2$ crystal doped by 1%ScF$_2$ with annealing in CF$_4$ (b)

3.4. Tm-doped BaF$_2$ crystals

The main objective of our investigation of BaF$_2$ crystals doped with 0.5, 1.0, 2.0 and 3.0 % Tm was the development of crystal production technology and then its application to ceramics with the possibility of a four-fold increase of the fast component yield and accordingly a significant reduction of the slow component.

The transmission spectrum of BaF$_2$:3%Tm is more complicated than a similar BaF$_2$:Sc spectrum. The spectrum is characterized by three main bands of absorption caused by $4f$–$4f$ transitions in Tm^{3+} ions.

Figure 4 presents X-ray luminescence spectra of BaF$_2$ single crystals, pure and doped with Tm at a concentration of 0.5 %. One can observe an increased yield of the fast component and the corresponding suppression of the slow one, which is typical for all the studied samples. Fitting the experimental data with two exponential decay curve gives $\tau_1 = 1.34 \pm 0.06$ ns and $\tau_2 = 534 \pm 7$ ns [2].

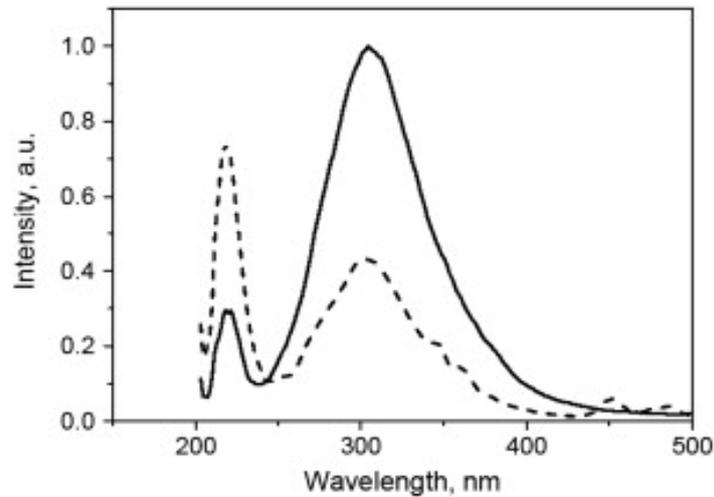**Fig. 4.** *X*-ray luminescence spectra of a single BaF_2 crystal (solid line) and a crystal of BaF_2 doped with Tm (dash line). The BaF_2:0.5%Tm crystal has the light yield of the 0.9 ns component 2.4 times larger than that of a single BaF_2 crystal and the slow component yield smaller by the same factor

3.5. Ce-doped BaF_2 crystals

Emission spectra of BaF_2 single crystals and those doped with 0.1 % of CeF_3 are shown in Figs. 4 and 5. The spectrum of the pure BaF_2 ceramics (as well as of the crystals) exhibits a wide band with a maximum near 300 nm, which is caused by self-trapped excitons and a weak band 220 nm relating to the core-valence transitions. In BaF_2:Ce^{3+}, two bands at 308 and 323 nm, typical for Ce^{3+} ions, have been detected.
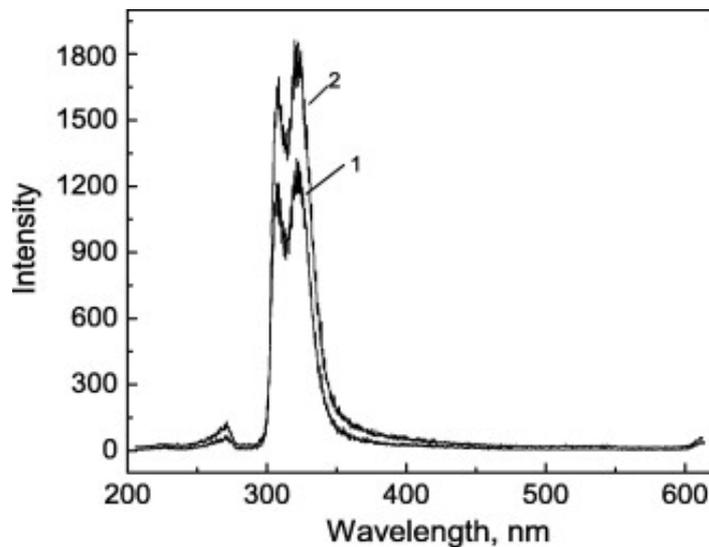
Fig. 5. *X*-ray induced emission spectra: 1 – BaF_2:Ce (0.1 %) single crystal and 2 – BaF_2:Ce (0.1 %) ceramics

It is worth noting that the intensity of the ultrafast component in BaF_2:Ce^{3+} ceramics is slightly larger than that in the standard BaF_2 crystals [3].

4. Photodetectors with AlGaN photocathodes

New photodetectors with photocathodes operated within the VUV spectral range have been developed. $Al_xGa_{1-x}N$ epitaxial films within a full range of composition (x = 0–1) and AlGaN-based heterostructures were grown by plasma-assisted molecular-beam epitaxy. The samples were grown on the annealed and

nitridated c-sapphire substrates, the growth temperature being varied within the range of 650–740 °C. The RF-power in the plasma source, changed within the range of 115–150 W at a constant nitrogen mass-flow of 5 sccm, allowed the N-limited growth rates from 0.25 to 0.5 μm/h, respectively. All the heterostructures had 1–1.6 μm-thick AlGaN buffers and p-type 20-nm-thick GaN:Mg top layers doped with solid-state Mg effusion cells. To control the AlGaN growth, a phenomenological approach based on simultaneous *in-situ* measurements of the laser interference and high energy electron diffraction followed by *ex-situ* electron probe micro-analysis was used. When the photocathode was grown, it was activated with Cs. The structural and optical properties of the structures were analysed using the scanning electron microscopy, the transmission electron microscopy, the X-ray diffraction and photoluminescence spectroscopy.

The Quantum Efficiency (QE) spectrum has an abrupt threshold at the photon energy equal to the GaN band gap. Changing the band gap value, it is possible to suppress the QE in the range of the BaF_2 slow luminescence component. The maximal value of the QE of 0.14 was measured at the wavelength of 230 nm [4].

5. Conclusion

1. The BaF_2 ceramics with the transmission at the wavelength 220 nm close to that of monocrystals can be obtained.

2. The BaF_2 ceramics luminescence spectrum demonstrates stability of the fast component and suppression of the slow one as compared to that of monocrystals.

3. Doping the BaF_2 crystals and the ceramics with different elements causes suppression of the slow component.

4. A photocathode with the quantum efficiency of 0.14 at 220 nm has been developed. The photocathode has an abrupt threshold about the slow luminescence component.

References

1. E.A. Garibin *et al*., Bull. Rus. Acad. Sci., Phys. **75**, 1011 (2011) (translated from Izvestiya Rossiiskoi Akademii Nauk., Ser. Fiz. **75**, 1066 (2011)).
2. D.M. Seliverstov, A.A. Demidenko, E.A. Garibin, *et al*., Nucl. Instr. Meth. A **695**, 369 (2012).
3. A.A. Demidenko, E.A. Garibin, S.D. Gain, *et al*., Opt. Materials **32**, 1291 (2010).
4. G. Benemanskaya, E. Garibin, Yu. Gusev, *et al*., Nucl. Instr. Meth. A **610**, 335 (2009).

COMPUTING FACILITIES FOR SMALL PHYSICS ANALYSIS GROUPS: EXAMPLES AND CONSIDERATION

A.Y. Shevel

1. Introduction

A small physics group (3–15 persons) might use a number of computing facilities for analysis/simulation, developing/testing, teaching. The most recent instances of small clusters for the Nuclear Chemistry Group at the State University of the New York campus, Stony Brook (http://www.sunysb.edu) and for the High Energy Physics Division at the Petersburg Nuclear Physics Institute (http://hepd.pnpi.spb.ru/) are briefly described here. Different types of computing facilities are discussed: collaboration computing facilities, local group computing clusters (including colocation), and cloud computing. A growing variety of the computing options and the growing role of the group-owned computing clusters of micro size are emphasized.

The members of a physics group usually have their computer accounts on large computing facilities, which are supported by institutional collaborations. Such facilities have certain rules: who can access the computing installation, in what scale, and for what purpose. As a result, the registration procedure takes some time. On the other hand, short-term students and/or visitors might need a computer account just temporarily. Finally, a physics group needs in addition to the institutional computing infrastructure a more agile and flexible computing infrastructure completely under group's control for several purposes:

- to keep common group data (papers, drafts, programs, fractions of experimental data, *etc.*);
- to test new/modified simulation or/and analysis software/algorithms;
- to provide an account for short-time visitors/students who need to do something in data analyses;
- for any other possible purpose, in particular, as a good gateway to remote large computing clusters.

We have to take into account the growth of the computing power of Computer Processing Units (CPU) every year. If we pay attention not only to CPU but to the whole computing power of a cluster, we can find, for example, such an estimation: "...DOE (U.S. Department of Energy) centres have historically delivered average improvements in computing capability of 40–80 % per year with relatively flat budget" [1]. This means that dozens of modern computing nodes in 2012 are more powerful than hundreds of servers in 2002.

Obviously, such a small computing installation is a good complement to large computing facilities. The computing needs can be considered in various ways (from the point of view of a small group):

- to use a big[1] centralized cluster (we mean a collaboration cluster);
- for cloud computing;
- as a group owned local cluster (might be in two instances):
    - location of the group computing cluster in the group office space with all responsibilities for air conditioning, electric power, hardware support, *etc.*;
    - colocation of the groups cluster hardware somewhere else [2].

Many pros and contras for each of the above listed options were discussed earlier [3]. Here it is assumed that the physics group uses more than one cluster to get the computing task done. Within the scope of papers, such group owned computing clusters are referred to as clusters Tier[2]-3 [4]. In the following in this paper, we will analyse our own local computing cluster and cloud computing facilities: now and in the nearest years.

Usually, a small physics group has limited financial resources. This fact does impose many restrictions on the cluster architecture. The cluster has to be:

- cheap (a useful consideration on the true cluster ownership cost is in Ref. [5]);
- composed of reliable hardware;
- not demanding for intensive supervision/maintenance.

---

[1] The cluster sizes: big, large – more than 1000 machines; middle size – up to 1000; small – up to 100; micro – around 10.

[2] In the grid, like the computing infrastructure around the LHC, several Tiers are defined: Tier-1, Tier-2, Tier-3, and so on. The difference is mainly determined by expected functionality (ability to accept and maintain the policy of Virtual Organization (VO), implement distinguished service for different VOs, availability of backup facilities, *etc.*).

Other requirements are the implications of the desire to reduce the maintenance efforts: compatibility (architecture and base OS) with the collaboration cluster environment (*e.g.*, as in the ATLAS or CMS and other CERN Collaborations), in particular, with the same set of application software, as in the collaboration cluster.

From the above, we see that a group-owned computing cluster cannot be large or even mid-range, it is quite small, a micro cluster. A good configuration of a group-owned cluster might consist of 5–15 modern machines (multicore CPUs, 2–3 GB of the main memory per core, 10–20 TB or more of the disk space per machine). It is better to use a 10 Gbit network switch. Such a group cluster can help to get more flexibility when using several remote computing facilities: the collaboration cluster(s), public/private cloud computing, *etc*.

The situations in different physics groups might differ from each other. Here, we shall discuss the particular group cluster solutions for the Nuclear Chemistry Group (NCG) at SUNYSB/Chemistry and for the High Energy Physics Division (HEPD) at PNPI.

2. Local computing cluster at SUNYSB/Chemistry

The computing cluster in the NCG was organized in 2000, or a bit earlier. At that time, all the machines (30+) had 512 MB of the main memory and Dual 500 MHz CPUs. This cluster was used for program developments, test analyses, students work, *etc*. There were more than 70 registered users, and about 3–5 of them were quite active. More detailed information about the cluster is available in Ref. [3].

To reduce the downtime of the cluster, it is good to buy and install special equipment – a KVM switch over the Internet Protokol [6] to do many control actions (switching on and off any machine in the cluster, to get access to the console of any machine, *etc*.) remotely over Internet. So, the group might use a remote help from external experts. However, in the cases described here the idea has not been implemented yet.

For the batch system, we use a pair of torque/maui from http://www.supercluster.org. Due to security reasons, the regular maintenance of the cluster is available only from specifically defined network domains. Because the cluster is located in a relatively large room with good ventilation, there is no need for air conditioning. After years of experience, we conclude that the University electric power supply is quite stable.

The basic OS (Scientific Linux with the same Red Hat Package Manager set as on the RHIC&ATLAS Computing Facility at BNL) installation procedure and the basic configuration are semiautomatic: there are a couple of scripts which use the kickstart as the initial step, and another step consists of a script for a post kickstart configuration. No virtualization technique was used in the cluster.

In our circumstances, the users mailing list does form a kind of a thinking engine for various methods how to use the cluster for concrete tasks. The mailing list is located in the Google.com (*i.e.* somewhere in a "cloud").

3. Local computing cluster at the High Energy Physics Division of PNPI

The computing cluster at the HEPD stemmed from a very small cluster consisting of three servers in February 1998. Details of the initial implementation are available in Ref. [7]. The cluster passed through multiple upgrades in hardware and software, though it remained quite small, or micro size. Now, the cluster consists of 5 hardware servers with 20 virtual machines (completely virtualized) and has around 16 TB of the disk space. The OS is Scientific Linux 5.7. There are about 150 registered users on the cluster; about 50 users logged many times per month, and about 15 persons use the cluster every day. Virtual tools permit to use specific configurations for specific user needs, *e.g.*, it is possible to use the CERNVM for a range of physics collaborations.

There is a custom-made backup scheme for user home directories (not for the data). One experienced person spends part of his/her time to keep the cluster running. The cluster room is equipped with air conditioner, UPSs, and UDP.

In the two computing cluster examples for High Energy Physics (at SUNYSB and PNPI) we can see the main similar trend: to reduce the cluster Total Cost of Ownership (TCO). It includes everything: the cost

of hardware and deployment, electric power, manpower, software and hardware support, any operation cost, cost of upgrades, *etc*. In this context it is not bad to have a look at the "cloud" computing.

4. Cloud computing

The cloud computing is a hot topic in the information technology for about 5 years. Many successful experiments with clouds were carried out (see Refs. [8–10]). It is not quite a common paradigm, though it has a lot of examples in government and private sectors. The quote below is a part of the most consistent cloud computing definition copied from Ref. [11].

Cloud computing is a model for enabling convenient, on-demand network access to a shared pool of configurable computing resources (*e.g.*, networks, servers, storage, applications, and services) that can be rapidly provisioned and released with minimal management effort or service provider interaction. This is just the beginning of the definition[3], but it gives the main idea. Scores of cloud services are available with a small difference in character and style of service and in policy of payment for the service, *e.g.* [12, 13].

Some physicists are afraid to use public cloud computing service because the public cloud is out of their control (for instance, the service could be down forever due to business or/and political issues). That is true. On the other hand, we can consider the control capability as the reliability of the access to the cloud. Can we think that public cloud service is 100 % reliable all the time? The right answer is "no". Unfortunately, we have to say the same about any other case of computing service of any kind. At the same time, small groups often have not so reliable local computing, which depends on unstable enthusiast activity. In many cases during even medium time frame (2–5 years), a local computing service is most probably less reliable than a public cloud computing service. If you are worrying about reliability of your data being safe, the obvious solution is to use all of the mentioned options.

Several successful testbeds with using the cloud computing for production simulation in HEP were carried out, *e.g.*, in ATLAS [12] and STAR [9]. The latter work has many deep and smart observations of the experience with computing in grid and cloud computing environments. The success does depend on a lot of details, in particular on the computing infrastructure components and their parameters which are "under hood" of the computing cloud. The authors of Ref. [14] were urged to do additional conversions of virtual machine images, may be for lack of open standards in the field. In other cases [9, 10], the authors found that the tested public cloud had not so good computer hardware parameters, as they expected. Also, the computing cloud initiatives and the government plans are to be taken into account [15].

5. Conclusion

Small computing/information installations are already on the way to use the clouds. For a small physics group, moving to the cloud does eliminate the cluster hardware maintenance task, but not the application software and data structure maintenance. Also, to achieve the maximal effect of using the cloud one should not ignore good understanding of the cloud hardware, architecture, and OS details.

We are emphasizing specifically the clusters of micro size, because if we take a look at a range of all size clusters, we might see more servers in the cluster, more spendings and efforts to support it. With a more powerful cluster, you need additional staff and additional activity to meet more complicated conditions including stronger regulations from the public authorities: fire safety, information security, insurance, *etc*.; all these factors increase the TCO significantly. There are many reasons for the TCO of midrange computing clusters to grow faster with the number of hardware servers than the total cost of the servers in the cluster, that is the relative TCO (per server) is less for micro size clusters and for huge clusters (due to the large scale) than for midrange clusters (see Fig. 1). This leads to the idea, that two main types of computing clusters will have long life: the huge clusters with many thousands of servers, often referenced as data centres which have a lot of users (actually such clusters are used as computing clouds), and micro clusters, which can be deployed in almost any office and used by a small group of users.

---

[3] The whole definition is explained on two pages or so.

Relative cost for cluster maintenance per one server

Number of servers in the computing cluster
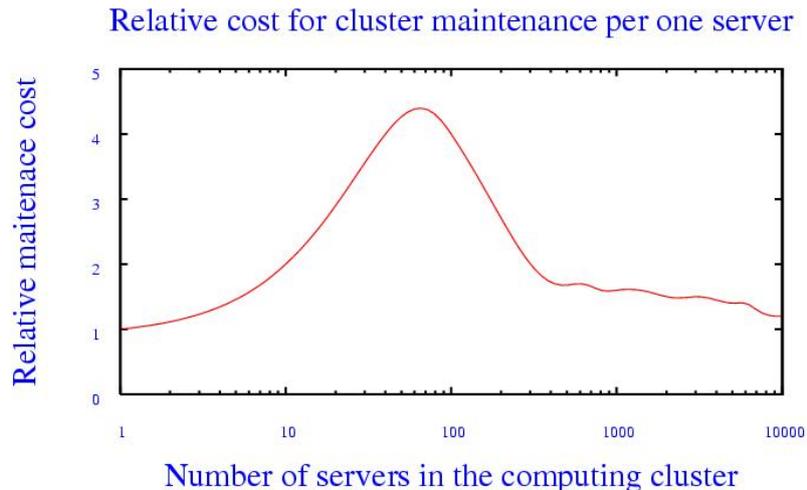
22/11/13 22:23

Fig. 1. Estimate of the relative maintenance cost per serever

In the light of the above experience, a group-owned cluster is to be used as an important gateway to public or private (*i.e.* collaborational) cloud computing. The number of public and private cloud computing instances is growing significantly every year. This means that the importance of suitable gateways to different clouds for small physics group is growing, as well.

References

1. The Magellan Report on Cloud Computing for Science – U.S. DOE, Office of Advanced Scientific Computing Research, December, 2011, p. 125;
   http://www.science.energy.gov/~/media/ascr/pdf/program-documents/docs/Magellan_Final_Report.pdf
2. Colocation Centre, http://en.wikipedia.org/wiki/Colocation_centre
3. Damian Reynolds, Andrey Y. Shevel, PHENIX Technical Note tn-452.0,
   http://www.phenix.bnl.gov/phenix/WWW/publish/shevel/tech-reports/ClusterPaper-2011-04-11.pdf
4. OSG Tier3 Twiki, https://twiki.grid.iu.edu/bin/view/Tier3/WebBook
5. The True Cost of HPC Cluster Ownership, http://www.clustermonkey.net//content/view/262/1/
6. KVM Switch, http://en.wikipedia.org/wiki/KVM_switch
7. Batch Computing Facility Based on PCs, http://hepd.pnpi.spb.ru/CSD/CSDPublications/proc_043.pdf
8. Jan-Philip Gehrcke *et al.*, ATALS@AWS, http://iopscience.iop.org/1742-6596/219/5/052020
9. Jerome Lauret *et al.*, From Grid to Cloud: STAR Experience,
   http://computing.ornl.gov/workshops/scidac2010/papers/data_j_lauret.pdf
10. Keith R. Jackson *et al.*, Performance Analysis of High Performance Computing Applications on the Amazon Web Services Cloud, http://www.lbl.gov/cs/CSnews/cloudcomBP.pdf
11. NIST Definition of Cloud Computing, http://www.nist.gov/itl/cloud/upload/cloud-def-v15.pdf
12. Dropbox, http://www.dropbox.com/
13. ADrive, http://www.adrive.com/
14. Jerome Lauret *et al.*, Contextualization in Practice: the Clemson Experience,
    http://pos.sissa.it/archive/conferences/093/027/ACAT2010_027.pdf
15. Vivek Kundra, U.S. Chief Information Officer, Federal Cloud Computing Strategy,
    http://www.cio.gov/documents/Federal-Cloud-Computing-Strategy.pdf